Causality and Heat Transport in Low Magnetic Shear Stellarators

by

Javier Hernández Nicolau

in partial fulfillment of the requirements for the degree of Doctor in

Plasmas y Fusión Nuclear

Universidad Carlos III de Madrid

Director/Tutor
Dr. Luis García Gonzalo

January, 2019

A Mar, i a mon pare i mu mare

Contents

Acknowledgments - Agradecimientos

I want to express my gratitude to all the people who, in some way, have helped me in this long journey.

Primero quería agradecer a mi director de tesis Luis García por guiarme en estos años y por recibirme siempre con una sonrisa. Sin su ayuda esta tesis no hubiera sido posible. También reconocer la enorme ayuda brindada por Benjamín Carreras quien, a pesar de no aparecer oficialmente, ha sido determinante en este trabajo. Gracias por la ayuda y por sacarme siempre una sonrisa a mí ¡y una carcajada a Luis!

A todo el equipo del TJ-II (CIEMAT) porque su trabajo es el fundamento de esta tesis. Especialmente a Boudewijn van Milligen por su colaboración y contribución en este proyecto.

I want to thank to David Newman and Uma Bhatt for their generous hospitality in our visit to Alaska. Also thank to Douglas for his help to get us into the American life.

Quiero recordar con especial cariño a todo mi grupo de amigos de mi infancia en nuestro barrio Son Roqueta: Toni, Hugo, Xisco M., Guillermo, María, Edu y Xisco S. Sin duda, durante muchos años, hemos pasado muy buenos momentos que me han forjado como la persona que soy. Aunque algunos de nosotros vivamos en puntos diferentes del mundo nuestras reuniones son como si nada hubiera cambiado. Ellos cumplen sobremanera la expresión: *La familia que uno elige.*

També volia agraïr a mom pare per transmetre'm la seva passió per la ciencia (si no fos per ell pot ser no seria aquí) i a mu mare per donar-ho tot sempre pels seus fills. De la mateixa manera vull recordar als meus germans Miquel i Elena els quals encara que ja no

visquem junts els tenc molt presents. A la meva *abuela-madrina* per aconsellar-me i sempre donar una mà en lo posible.

Vull recordar també a la Universitat de les Illes Balears on vaig cursar la llicenciatura en Física i al IFISC el master. Durant molts d'anys em van formar com a futur científic. També recordar a Guillem, Julián i Toni per totes les cervesses que em fet plegats.

En la Universidad Carlos III de Madrid he pasado gran parte de estos últimos cuatro años. Quiero agradecer a todo el Departamento de Física su labor y haberme dado la oportunidad de realizar mi doctorado. También mencionar especialmente al grupo de Fusión Nuclear: a Raúl por sus comentarios y saberme aconsejar, a Ramón por esa cercanía que le caracteriza y su esfuerzo como director del programa de doctorado; y a Víctor por su profesionalidad y su enorme trabajo a cargo del cluster *Uranus*. A José Miguel por ser esa conexión entre profesores y doctorandos y estar siempre allí para ayudarte. Quiero recordar a todo el grupo de doctorandos del "despacho" (aunque algunos ya se marcharon): Aaron, Toon, Hugo, Gabi, Jorge, Rubén, Maša, Amalia, Žana, Gonzalo, Alena, Julio y Álvaro y, en especial, a Luis y Will. Gracias chicos por estos más de cuatro años, mi vida en Madrid ha sido mucho mejor junto a vosotros.

Me gustaría recordar la que ha sido mi casa durante estos dos últimos años: el colegio mayor Fernando Abril Martorell. Quiero agradecer a todo el personal su trabajo y familiaridad al hacerme sentir, literalmente, como en casa. A Pepi por su personalidad y ser la esencia de la FAM y a la directora, Maria Durbán, por su ayuda.

Agradecer también al (ahora) Ministerio de Ciencia, Innovación y Universidades haber financiado este doctorado mediante los contratos predoctorales (FPI). De la misma manera agradecer su financiación de mi estancia temporal en Alaska.

Por último, y claramente no menos importante, a mi esposa Mar. Gracias por tu apoyo y por estar ahí en los buenos y en los malos momentos, sin tí sería otra persona.

Y a todos los que, de alguna manera, han contribuido a donde estoy. Gracias a todos. Gracies a tots. Thank you all.

Javier H. N.

Abstract

Nuclear Fusion is becoming the most promising way to achieve a reliable and sustainable source of energy in the coming future with a low environmental impact. Hundreds of millions degrees are required to obtain the desired Nuclear Fusion reactions so plasma must be confined using strong magnetic fields. Under such large temperatures plasma is far away from equilibrium and high temperature gradients (and heat fluxes) appear. For several decades, heat transport has been one of the main issues to achieve the goal of an efficient nuclear fusion reactor. High losses yields to a poor confinement and reduce the viability of a reactor. Even though, heat transport is not yet well understood and still much work is necessary.

In this thesis heat transport in fusion plasmas is analyzed in the framework of resistive MHD simulations. To do so, we use the Transfer Entropy (TE) technique. Chapter 2 introduces the MHD model used to simulate fusion plasmas and the Transfer Entropy approach is described in Chapter 3.

The TE is a technique, from Information theory field, which measures the information propagation between two time signals. The TE can identify if previous events in one signal can be used to predict future events in another signal. Its main advantage is that it shows the direction of that information flow. In this sense, by *causality* we mean that if the information is flowing from A to B then A *causes* B. Therefore, we make an analogy between the information propagation and heat propagation.

The most used methods to study heat transport in experimental fusion plasmas are the perturbative methods. They have been used during decades in most fusion devices. Most of the experiments use external heating modulation to determine the plasma response and, in this way, analyze heat transport.

In numerical models is relatively easy to introduce a heat perturbation in the plasma and study its time evolution. That is not the case in experimental plasmas where to set a single pulse can be not feasible and it is not easy to identify it due to the background noise. The approach presented here, based on the Transfer Entropy, illustrates a new tool to analyze heat transport.

In recent experiments [1], the ERCH was used to heat inner locations of the plasma and then observe the spontaneous perturbations generated by the heating. The electron temperature was measured at different radial locations during the presence of spontaneous perturbations in the core. Then the Transfer Entropy was applied from a reference point in the core to the different signals radially distributed. In this way, radial heat propagation was observed using TE. However this propagation was neither continuous nor diffusive and showed *trapping* regions where perturbations were slowed down. Chapter 4 sums up some of the experimental observations and then apply the same Transfer Entropy approach to numerical simulations of TJ-II plasmas. The numerical model allows us to understand the underlying physics and interpret the experimental results. The model is applied to different cases and similar conclusions are obtained. We can identify as well regions were the perturbations are mostly trapped and other regions were radial transport is faster. This trapping regions are suggesting the presence of (mini) transport barriers [2].

The same study of heat transport was done in the W7-X [3]. In spite of the fact that the W7-X device has a better performance and many differences with the TJ-II, it has a common characteristic of being a stellarator with low magnetic shear. Due the low shear, low order modes may extend in a wider radial region. The presence of these rational surfaces may generate transport barriers. Chapter 5 introduces some of the experimental observations in Ref. [3] and then our numerical model is used in order to interpret these experiment results. Using the TE approach we observe, again, regions where heat perturbations are trapped or regions with enhanced transport.

In Chapters 4 and 5 the heat transport is studied qualitatively. The Transfer Entropy allows to identify radial regions in the plasma with different heat transport. However, in Chapter 6, we use the Transfer Entropy to quantitatively study that radial heat transport. The technique is able to estimate an effective diffusivity at different radial locations. The TE is compared with other approaches to demonstrate

its effectiveness.

Chapter 7 describes the emergence of transport barriers and turbulent vortices. Resistive interchange instabilities yield to turbulent vortices which follow the magnetic field lines. Therefore, those turbulent vortices may have a filamentary structure. The total contribution of the different turbulent vortices and fluctuations in the plasma may generate an average poloidal flow which in turn can lead to the formation of transport barriers.

The turbulent vortices, related to the transport barriers, should be found as filamentary structures in the plasma. In Chapter 8, the topology of filamentary structures in TJ-II is analyzed using the Transfer Entropy technique. First, some of the experimental results in TJ-II are summarized and then our numerical simulations are used to interpret these results. Focusing on the electrostatic potential we can observe that there are (filamentary) structures following the magnetic field lines in radial surfaces. By the TE approach, periodicity, length, radial width and velocity of filaments can be calculated. Then, we find that where we observed trapping radial regions (Chapter 4), there are filamentary structures. We associate the presence of these filaments with the transport barriers.

Finally, Chapter 9 reproduces some of the studies from the previous chapter but for the W7-X device. Using our numerical simulations, some of the properties of the filamentary structures are studied and similar conclusions are obtained. This work may be used in future experiments to interpret the results.

Resumen

La Fusión Nuclear se ha convertido en el camino más prometedor para alcanzar una fuente de energía fiable y sostenible en un futuro próximo con un bajo impacto medioambiental. Cientos de millones de grados son necesarios para alcanzar las deseadas reacciones de Fusión Nuclear así que el plasma debe ser confinado usando fuertes campos magnéticos. Con estas enormes temperaturas el plasma está lejos del equilibrio y grandes gradientes de temperatura (y flujos de calor) aparecen. Durante décadas el transporte de calor ha sido uno de los temas principales en la búsqueda de un reactor de Fusión Nuclear eficiente. El elevado número de perdidas conlleva a una reducción del confinamiento y reduce la viabilidad de un reactor. Aun así, el transporte de calor todavía no se entiende totalmente por lo tanto queda mucho trabajo por delante.

En esta tesis el transporte de calor en plasmas de fusión es analizado en el contexto de simulaciones MHD resistivas. Para ello usamos la técnica Transferencia de Entropía (TE). El Capítulo 2 introduce el modelo MHD usado para la simulación de plasmas de fusión y el Capítulo 3 describe el procedimiento de la Transferencia de Entropía.

La TE es una técnica, del campo de la Teoría de la Información, la cual mide la propagación de información entre dos señales. La TE puede identificar si eventos pasados en una señal pueden ser usados para predecir eventos futuros en la otra señal. Su principal ventaja es que muestra la dirección del flujo de información. En este sentido, por *causalidad* nos referimos a que si la información está fluyendo de A hacia B entonces A *causa* B. De esta manera hacemos una analogía entre la propagación de información y la propagación de calor.

Los métodos más usados en el estudio del transporte de calor en plasmas experimentales de fusión son los métodos perturbativos. Estos han sido usados durante décadas en la mayoría de dispositivos de

fusión. Muchos de estos experimentos usan un calentamiento externo modulado para determinar la respuesta del plasma y, de esta manera, analizar el transporte de calor.

En modelos numéricos es relativamente fácil introducir una perturbación de calor en el plasma y estudiar su evolución temporal. No es el caso en plasmas experimentales donde lanzar un único pulso puede no ser viable y no es fácil de identificar debido al ruido de fondo. La estrategia presentada aquí, basada en la Transferencia de Entropía, muestra una nueva herramienta para analizar el transporte de calor.

En recientes experimentos [1], el ECRH fue utilizado para calentar regiones internas del plasma para luego observar las perturbaciones espontaneas que se generaban durante el calentamiento. Se midió la temperatura electrónica en diferentes puntos radiales durante la presencia de perturbaciones espontaneas en el núcleo. Después la Transferencia de Entropía fue aplicada desde un punto de referencia en el nucleo a las diferentes señales distribuidas radialmente. De esta manera, la propagación radial de calor fue observada usando la TE. Sin embargo, esta propagación no era continua ni difusiva y mostraba regiones de *atrapamiento* donde las perturbaciones se frenaban. El Capítulo 4 resume algunos de los resultados experimentales observados y después aplica el mismo método de la Transferencia de Entropía a simulaciones numéricas de plasmas en el TJ-II. El modelo numérico nos permite entender la física subyacente e interpretar los resultados experimentales. El modelo es aplicado a diferentes casos y se obtienen conclusiones similares. Podemos identificar también regiones donde las perturbaciones mayormente son atrapadas y otras regiones donde el transporte radial es más rápido. Estas regiones de atrapamiento nos sugieren la presencia de (mini) barreras de transporte [2].

El mismo estudio de transporte de calor fue realizado en el W7-X [3]. A pesar de que el dispositivo W7-X tiene un mejor rendimiento y muchas diferencias con el TJ-II, tiene una caracteristica común al ser un stellarator con una pequeña cizalla magnética. Debido a esa pequeña cizalla, modos de orden bajo pueden extenderse radialmente. La presencia de estas superficies racionales puede generar barreras de transporte. El Capítulo 5 introduce algunas observaciones experimentales de la Ref [3] y luego nuestro modelo numérico es usado para interpretar esos resultados experimentales. Usando el método TE observamos, otra vez, regiones donde las perturbaciones de calor están atrapadas o regiones con un transporte mayor.

En los Capítulos 4 and 5 el transporte de calor se estudia cualitativamente. La Transferencia de Entropía permite identificar regiones radiales en el plasma con diferente transporte de calor. Sin embargo, en el Capítulo 6, usamos la Transferencia de Entropía para estudiar cuantitativamente el transporte radial de calor. La técnica es capaz de estimar una difusividad efectiva en diferentes puntos radiales. La TE es comparada con otros métodos para demonstrar su efectividad.

El Capítulo 7 describe la emergencia de barreras de transporte y vórtices turbulentos. Las inestabilidades resistivas de intercambio dan lugar a vórtices turbulentos los cuales siguen las líneas de campo magnético. Por consiguiente, esos vórtices turbulentos pueden desarrollar una estructura filamentaria. La contribución total de los diferentes vórtices turbulentos e inestabilidades en el plasma puede generar un flujo poloidal promedio el cual puede dar lugar a la formación de barreras de transporte.

Los vórtices turbulentos, relacionados con las barreras de transporte, deben poderse encontrar como estructuras filamentarias dentro del plasma. En el Capítulo 8 la topología de las estructuras filamentarias en el TJ-II es analizada usando la técnica de la Transferencia de Entropía. Primero, algunos de los resultados experimentales en el TJ-II se resumen, después usando nuestras simulaciones numéricas interpretamos esos resultados. Centrándonos en el potencial electrostático podemos observar que hay estructuras (filamentarias) siguiendo las líneas de campo magnético en superficies radiales. Con el método TE, la periodicidad, longitud, ancho radial y velocidad de los filamentos se puede calcular. Luego encontramos que donde se observan las zonas radiales de atrapamiento (Capítulo 4) hay estructuras filamentarias. Asociamos la presencia de esos filamentos con las barreras de transporte.

Finalmente, el Capítulo 9 reproduce algunos de los estudios del anterior capítulo pero para el dispositivo W7-X. Usando nuestras simulaciones numéricas, estudiamos algunas de las propiedades de las estructuras filamentarias y obtenemos conclusiones similares. Este trabajo puede ser usado en futuros experimentos para interpretar sus resultados.

Published & Submitted Content

Articles or other contributions (co)-authored by the Doctoral candidate that are included as part of the thesis and that have been published:

- B.Ph. van Milligen, J.H. Nicolau, L. García, B.A. Carreras and C. Hidalgo. *"The impact of rational surfaces on radial heat transport in TJ-II"*. Nucl. Fusion **57**, 056028 (2017). [1]

  https://doi.org/10.1088/1741-4326/aa611f

  This item is partly included in Chapter 4 and is mentioned in the introduction of the Chapter. The material from this source that is included in this thesis has not been singled out with typographic means; appropriate references are made. Reproduced here with permission of the copyright owner, *Institute of Physics (IOP)*.

- B.Ph van Milligen, U. Hoefel, J.H. Nicolau, M. Hirsch, L. García, B.A. Carreras and C. Hidalgo. *"Study of radial heat transport in W7-X using the transfer entropy"*. Nucl. Fusion **58**, 076002 (2018). [3]

  https://doi.org/10.1088/1741-4326/aabf5d

  This item is partly included in Chapter 5 and is mentioned in the introduction of the Chapter. The material from this source that is included in this thesis has not been singled out with typographic means; appropriate references are made. Reproduced here with permission of the copyright owner, *Institute of Physics (IOP)*.

- J.H. Nicolau, L. García, B.A. Carreras and B.Ph van Milligen. *"Applicability of Transfer Entropy for the calculation of effective diffusivity in heat transport"*. Phys. Plasmas **25**, 102304 (2018). [4]

  https://doi.org/10.1063/1.5041495

  This item is partly included in Chapter 6 and is mentioned in the introduction of the Chapter. The material from this source that is included in this thesis has not been singled out with typographic means; appropriate references are made. Reproduced here with permission of the copyright owner, *AIP publishing.*

- B.Ph. van Milligen, J.H. Nicolau, B. Liu, G. Grenfell, U. Losada, B.A. Carreras, L. García and C. Hidalgo. *"Filaments in the edge confinement region of TJ-II"*. Nucl. Fusion **58**, 026030 (2018). [5]

  https://doi.org/10.1088/1741-4326/aa9db6

  This item is partly included in Chapter 8 and is mentioned in the introduction of the Chapter. The material from this source that is included in this thesis has not been singled out with typographic means; appropriate references are made. Reproduced here with permission of the copyright owner, *Institute of Physics (IOP).*

Other contributions

Articles or other contributions (co)-authored by the Doctoral candidate that are not included in this thesis:

- J.H. Nicolau, L. García and B.A Carreras. *"Correlations and non-local transport in a critical-gradient fluctuation model"*. J. Phys.: Conf. Ser. **775**, 012008 (2016).

- B.Ph. van Milligen, B.A. Carreras, L. García, A. Martín de Aguilera, C. Hidalgo and J.H. Nicolau. *"The causal relation between turbulent particle flux and density gradient"*. Phys. Plasmas **23**, 072307 (2016).

- J.H. Nicolau, L. García, B.A. Carreras, B.Ph. van Milligen, B. Liu, G. Grenfell, U. Losada and C. Hidalgo. *"Detection of filamentary structures using the Transfer Entropy in TJ-II and W7-X"*. 45th EPS conference on Plasma Physics, Prague (2018).

Abbreviations & Symbols

NF	Nuclear Fusion
MCNF	Magnetic Confinement Nuclear Fusion
ICF	Inertial Confinement Fusion
JET	Joint European Torus
ECRH	Electron Cyclotron Resonance Heating
NBI	Neutral Beam Injection
ECE	Electron Cyclotron Emission
SOC	Self-Organized Criticality
ELM	Edge Localized Mode
MHD	MagnetoHydroDynamics
TE	Transfer Entropy
PDF	Probability Distribution Function

$\boldsymbol{r}$	Position vector
$\boldsymbol{v}$	Velocity vector
r	Radial direction
θ	Poloidal angle
ζ	Toroidal angle
$\boldsymbol{E}$	Electric field
$\boldsymbol{B}$	Magnetic field
$\boldsymbol{J}$	electric current
ι	Rotational transform
q	Electric charge
m_i	Mass of particle i
e	Fundamental electric charge
n	Density
T_e	Electron temperature
ρ	Mass density

η	Resistivity
Φ	Electrostatic potential
ψ	Poloidal magnetic flux
q	Safety factor
m	Poloidal mode number
n	Toroidal mode number
$\boldsymbol{k}$	Wave vector
a	Minor radius (torus)
R	Major radius (torus)
ε	Inverse aspect ratio of a toroidal device
D	Diffusivity
χ	Thermal diffusivity
β	Ratio plasma pressure to magnetic pressure
τ_R	Resistive time
τ_A	Alfvén time
S	Lundquist number
ω_{*e}	Electron diamagnetic frequency
ω_{ci}	Ion cyclotron frequency
x_{eq}	Equilibrium component of a variable x
$\tilde{x}$	Fluctuating component of a variable x

List of Figures

Chapter 1

Introduction

Humankind is living, for the last century, in an era of an unprecedented economical expansion [7]. Clearly, a large energy demand is bounded to this broad economic growth and increase in average income. The global energy consumption in 1990 was about 1 billion GW, today is higher than 10 billion GW [8]. Making a pen, checking your email, flying from Madrid to Tokyo or cook a pizza, all of them require some amount of energy. Humans have become more and more dependent of energy, one simply has to think about people reaction during a blackout. For thousand of years energy was nothing to worry about, if people needed a fire to cook or heat the house they just burnt some logs. But once in the industrial era and with a fast growing population [9] energy became an issue. The problem is not just find an efficient source of energy but take care of its sustainability and environmental consequences.

From XIX century energy production in the world has been based in fossil fuels (coal, petroleum or natural gas), its efficiency, price and easy combustion made them the pillar of the industrial era. However in the last years their disadvantages have been more visible. Global warming, due the greenhouse effect, is becoming an issue [10, 11] and most governments are making an effort to stop or, at least, slow down their emissions [12]. On the other hand, combustion of fossil fuels is potentially dangerous for people and even responsible of numerous deaths in polluted areas [13]. Due these drawbacks many big cities, in order to protect their citizens, are making policies to reduce (or even ban) the combustion in private cars or industries [14].

Nuclear fission as a source of energy was originated in 1950s and

many developed countries have established several power plants. For example electric power in France is 70% produced by Nuclear plants[15]. That technology allows a high amount of power with very low economic costs [16]. However this energy has a higher environmental cost, the main disadvantage is how to deal with the nuclear waste and its associated radioactivity. Having a half-live of the order of thousands of years, uranium becomes an extremely difficult problem to solve in the long run. Not to mention the bad reputation of this energy due to some unfortunate accidents as in Chernobyl and Fukushima [17].

In the last decades, renewable energies (as wind, solar panels or hydroelectric) have shown to be efficient, economically viable and environmentally friendly. This has allowed a growth in its adoption in the electricity production and many people demand a larger implementation of this kind of source of energy. For example, 40% of electricity produced in Spain by originated by renewable energies in 2016 [18]. However, what is not obvious for the general public is that a 100% implementation of renewable energy is not viable. Being an intermittent source of energy makes impossible to satisfy the energy demand of a country in a mid-term.

In this goal for an efficient, clean and affordable energy, Nuclear Fusion is playing an important role. Large amounts of energy can be produced in fusion reactions where the main advantages are the lack of greenhouse gas emissions and the low amount of wastes with a low half-life. Nuclear Fusion is not yet efficient for a commercial use but projects as ITER should demonstrate in a decade if this kind of energy is viable.

1.1 Nuclear Fusion

During the first decades of the XX century nuclear physics was developed and yielded to the discovery of the fusion nuclear reactions. In that process two light nuclei are bring together, they *fuse* and a heavier nuclei (or more) is produced along a large amount of energy. The energy comes from the the mass defect between the two light nuclei and the "heavier" nucleus. The reaction is more efficient for the lighter elements due to a lower binding energy [19]. It is a natural process which for example powers our sun fusing hydrogen (and others) nuclei. The easiest fusion reaction to achieve in experiments is the Deuterium

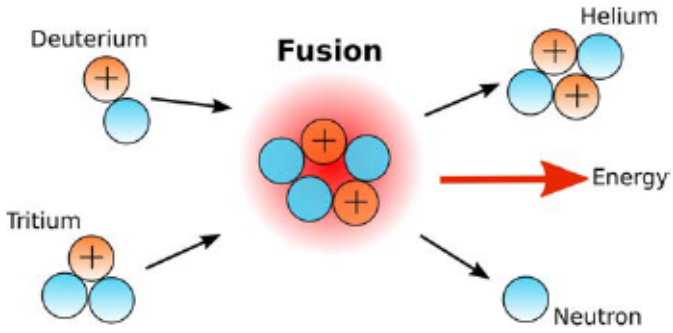

Figure 1.1: Nuclear Fusion reaction.

(D) and Tritium (T) reaction (see Fig. 1.1) because it has a maximum of cross section (probability to collide) at the lowest temperature [20]. These two hydrogen isotopes fuse as

$$ {}^{2}_{1}H + {}^{3}_{1}H \rightarrow {}^{4}_{2}He + n + 17.6\text{MeV} \tag{1.1} $$

so the fusion of deuterium (${}^{2}_{1}H$) and tritium (${}^{3}_{1}H$) nuclei generates a Helium nucleus (alpha particle), a neutron and 17.6MeV of energy.

The nuclear fusion reaction is a very efficient generation of energy in terms of energy produced by mass and the equivalence with fossil fuels is [20]

$$ 10^{6} \text{ tonnes of oil} = 0.14 \text{ tonnes of deuterium.} $$

Deuterium is a relatively easy to find hydrogen isotope and is present in the water in the Earth [21]. However Tritium is more complicated to obtain because it has a half-life of 12.26 years so it cannot be found in nature and has to be generated artificially. In future fusion reactors, as ITER, the tritium can be bred using Lithium and the neutrons from the fusion reaction in the following way

$$ \begin{aligned} {}^{6}_{3}Li + n &\rightarrow {}^{4}_{2}He + {}^{3}_{1}H + 4.8\text{MeV} \\ {}^{7}_{3}Li + n &\rightarrow {}^{4}_{2}He + {}^{3}_{1}H + n - 2.5\text{MeV}. \end{aligned} \tag{1.2} $$

The presence of lithium in the fusion reactors has some advantages, the first is the tritium breeding we just commented which at the same time reduce the number of neutrons escaping from the reactor. The second is that lithium is used to dissipate the large amounts of energy produced in a future reactor.

One of the main disadvantages of Nuclear Fusion, apart from the generation of neutrons, is that the Tritium is radioactive and, clearly, dangerous. However, as we mentioned, its half-life is short and possible waste could be handled in a generation in the same way as the activated components of the reactor due to the neutrons.

In spite of the problems in the D-T reaction, it is the more promising fusion reaction and the first generation of reactors will use this fuel. The extraction of Tritium is technologically feasible and for example ITER will use the Lithium method. In second generation (and future) fusion reactors the desirable reactions will be D-D

$$\begin{aligned} {}^2_1H + {}^2_1H &\rightarrow {}^3_2He + n + 3.27\text{MeV} \\ {}^2_1H + {}^2_1H &\rightarrow {}^3_1H + p + 4.03\text{MeV} \end{aligned} \tag{1.3}$$

where p is a proton.

Fusion reactions, in general, do not occur naturally because the nuclei repel each other due to the Coulomb interaction, so energy is needed to overcome that repulsion and bring together the nuclei. The only known natural fusion reaction is the observed in the Sun and other stars. In these systems the gravitational force is large enough to join the nuclei and produce fusion reactions in the star core. Obviously that is not possible in a laboratory so two different approaches have been proposed as a feasible way to reach controlled nuclear fusion. The first approach is Magnetic Confinement Nuclear Fusion (MCNF) which is the one this thesis is focused on (see Sec. 1.2 for a description). The second one is the Inertial Confinement Fusion (ICF) where fusion reactions are obtained by accelerating the particles using extremely powerful lasers. The lasers fire to a spherical pellet filled with the fuel and generate an implosion which bring together the nuclei. The largest experiments in ICF are the National Ignition Facility in Livermore, US and the Laser Mégajoule in Bordeaux, France.

The large amount of energy needed in the MCNF or ICF approaches for fusion results in high pressure values in the fuel. Under these conditions the fuel is in the *plasma* state. Plasma, considered as fourth state of matter, is a gas which ions and electrons have been decoupled. One of the main properties relevant here is that plasma responds to electromagnetic fields.

1.1.1 Energy balance

The goal of the research in Nuclear Fusion is to obtain net energy from these processes. In a reactor we need to introduce some amount of energy to bring together the nuclei and allow fusion reactions. Therefore, in the *breakeven* the energy obtained by the reactions should be at least equal to the input energy taking into account the losses.

In general the power balance of sources and sinks of energy is

$$P_f + P_h = P_B + P_k \tag{1.4}$$

where P_f is the power obtained from fusion reactions, P_h is the heating (input power) and P_B and P_k are the radiative (mainly bremsstrahlung) and thermal losses respectively. How to quantify and determine the thermal losses in plasma is one of the main problems in Nuclear fusion, heat transport is not well understood as it will be shown in Sec. 1.3. However, fusion community defines a *confinement time* τ_E which represents the losses as

$$\tau_E = \frac{3nT}{P_{\text{losses}}} \tag{1.5}$$

where P_{losses} takes into account the radiative and thermal losses and $3nT$ is the internal energy density of a plasma with density n and temperature T using the Equipartition theorem [22].

A desirable reactor in steady state should no need external heating so the losses are covered by the energy obtained in the fusion reactions. We call that this condition *ignition* so

$$P_f = P_B + P_k. \tag{1.6}$$

This relation can be estimated in terms of density, temperature and confinement time. It gives a criterion such as the triple product of these quantities has to be larger than certain threshold to have ignition so

$$n\tau_E T \geq f(T). \tag{1.7}$$

The threshold is a function of temperature and depends on the components of the plasma. For example, in a D-T reaction with a temperature of 15KeV (approximately 170 millions degrees) the criterion becomes [23]

$$n\tau_E T \geq 3 \times 10^{21} m^{-3} \text{KeV s} \tag{1.8}$$

The ignition criterion has some relevant consequences in the design of a fusion reactor. The temperature is one of the parameters which cannot be modified in excess because the cross section for fusion reactions is high only in a short temperature range. Then the density can be increased up to certain value known in MCNF devices as Greenwald limit [24] where plasma is unstable and disruptions may occur. So the only option is to improve the confinement time, that is, reduce the power losses. One easy way is to increase the reactor size which increases as well the τ_E, however a size increment in a fusion device implies a rise in complexity and cost. Another way is improving the confinement analyzing heat transport and establishing some conditions to reduce that transport.

1.2 Magnetic Confinement Nuclear Fusion

From all the possible mechanisms to reach Nuclear Fusion as a source of energy the Magnetic Confinement is the most promising one. For fusion reactions large values of temperature (hundreds of millions $°C$) need to be achieved so the fuel becomes plasma. Due to the large temperatures, plasma must be confined and kept away from the walls of the reactor. Since plasma is made of ionized particles it reacts to a magnetic field. In the presence of the magnetic field the particles follow a helical trajectory around the magnetic field line (see left figure in Fig. 1.2) so particles are rotating with a particular *cyclotron* frequency and *Larmor* radius [25].

In a real system the plasma must be contained in a finite space. Due to the $\nabla \cdot \boldsymbol{B} = 0$ the magnetic field lines must be either infinite or finite but closing themselves. The plasma can be trapped in magnetic mirrors or closing the field lines in a toroidal geometry. First calculations and experiments showed that magnetic mirrors have many more losses than toroidal devices so MCNF has been focusing in toroidal geometries. Not all the field lines in a torus need to be closed to confine the particles, the lines can also go around the torus infinitely filling a surface or volume.

Studying the equilibrium and stability of the plasma leads to some restrictions in the geometry of the magnetic field in the toroidal device. The magnetic field B has not only a component in the toroidal

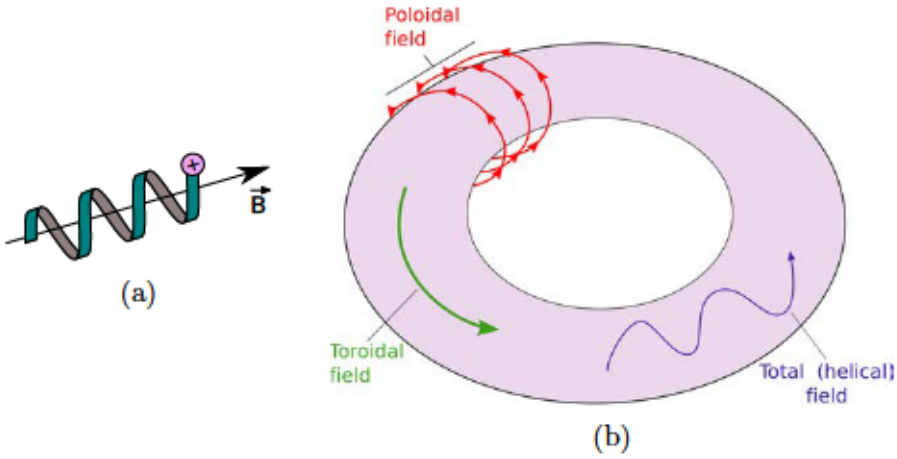

Figure 1.2: (a) Charged particle in a magnetic field. (b) Poloidal, toroidal and total field in a toroidal geometry.

direction B_z but another component in the poloidal direction B_θ. The sum of both contributions generates a helical magnetic field. Right figure in Fig. 1.2 shows a schematic of the magnetic field components.

The magnetic field lines lie in toroidal surfaces which ideally are nested surfaces. Note that not all the magnetic field lines in the torus are closed because the values of toroidal and poloidal field change in space. Even though, at certain regions the field lines may close. The *rotational transform* is defined as a quantity that measures the number of poloidal turns by toroidal turns

$$\iota = \frac{\text{Num. poloidal turns}}{\text{Num. toroidal turns}}. \tag{1.9}$$

At certain surfaces, where the magnetic field lines close after being winded around the torus, ι is a rational number so they are called *rational surfaces*. For certain devices (Tokamaks) the inverse quantity, called *safety factor*,

$$q = \frac{1}{\iota} \tag{1.10}$$

is used. It is called safety factor because if $q > 1$ at all points the plasma is stable to internal kink instabilities.

The most successful devices so far are the Tokamak and the stellarator. In Tokamaks the poloidal magnetic field is generated from a toroidal current in the plasma. A brief description and some of

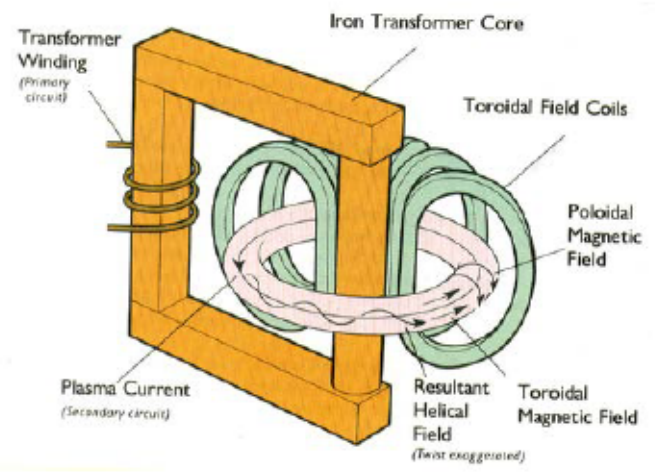

Figure 1.3: Tokamak schematic. Poloidal magnetic field is produced by the toroidal current generated by the induction of the transformer.

their properties is given in Sec. 1.2.1. On the other side, in stellarators toroidal and poloidal magnetic fields are produced from external coils. All the results of this thesis correpond to the TJ-II and W7-X stellarators, both of them are described in Sec. 1.2.2 and Sec. 1.2.3 respectively.

1.2.1 The Tokamak

Although the Tokamaks was invented after the stellarator, it is nowadays the most promising concept to obtain energy from Nuclear Fusion. The Tokamak was proposed by the USSR in the late 50's as a different toroidal confinement device, it gave much better confinement time values than other devices at that time. For that reason during many years researchers put much effort on this device and the stellarator concept was set aside by a large part of the fusion community. [26]

The basic design of the Tokamak is simple, the toroidal magnetic field is generated by external coils but the poloidal field is generated by a toroidal current in the plasma. The current is produced using the idea of a transformer where the plasma is the secondary coil. The concept of the Tokamak is sketched in Fig. 1.3. Furthermore the toroidal current is used as well as a heating system through the Ohmic heating.

One advantage of the Tokamak is that it is an axisymmetric device

so a poloidal cross section should be similar for any toroidal angle. Thus the symmetry simplifies many calculations as it can be considered a 2D system.

However, the Tokamak has as well some drawbacks. The most important is due to the nature of a transformer itself. The electromagnetic induction necessary in the transformer is only possible if the current in the transformer winding is not constant. That means that the toroidal current generated in the plasma cannot be continuous. This pulsed current of Tokamaks makes not possible a steady state operation.

Another disadvantage is the presence of the toroidal current. Currents in the plasma should be avoided because they are a source of instabilities [27]. Furthermore these instabilities can lead to disruptions where most of the energy of the plasma is released abruptly [28].

The largest Tokamak is the Joint European Torus (JET) in Culham (UK) built in the beginning of the 80's [29]. It is still in operation and was the first one to produce energy from D-T reactions [30].

Nowadays the biggest project in Nuclear Fusion, ITER, is being built in Cadarache (France) in an alliance of the world's most powerful countries. ITER is a tokamak reactor designed to prove the feasibility of Nuclear Fusion as an energy source [31, 32]. At the moment of writing this thesis ITER construction is more than 50% completed and first plasmas are expected around 2025.

1.2.2 TJ-II

The Stellarator was one of the main concepts to achieve MCNF. The idea was firstly presented by Spitzer in the 50's and it consisted in a toroidal geometry where the magnetic fields are generated by external coils [33]. However, at the same time the Tokamak was also presented and it exhibited a better performance with higher confinement times, the particle losses in the stellarator were much higher. The reason is that the 3D magnetic field necessary to average out the drift of particles needs to be precise enough. In the last decades advances in numerical calculation and stellarator optimization have allowed the design of better magnetic configurations which reduces losses to an acceptable level [6].

Stellators are still less developed than tokamaks however they are as well a promising device for Nuclear Fusion reactions. The main

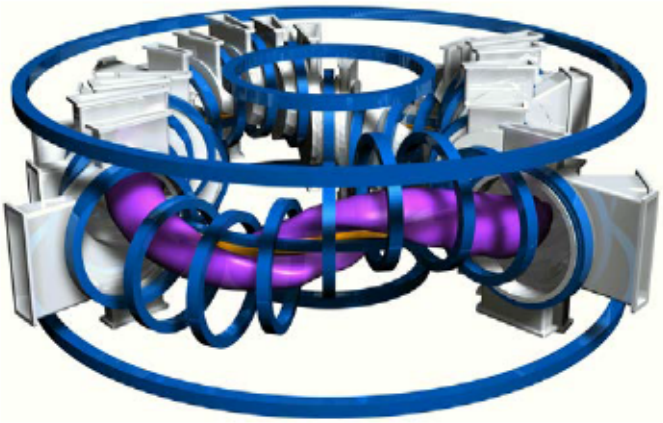

Figure 1.4: 3D model of the TJ-II stellarator.

advantage is that they can operate in steady state. Furthermore both toroidal and poloidal magnetic fields are generated and controlled by external coils. Ideally there are no currents in the plasma so no current instabilities should appear neither the possibility of disruptions. On the other hand, the lack of toroidal currents discards the possibility to heat the plasma with the Ohmic heating.

The largest stellarator in the world is the Wendelstein 7-X (see Sec. 1.2.3) in Greifswald (Germany) which started operation in 2015. The number of stellarators currently in operation is low but other relevant devices are the LHD in Japan and the TJ-II in Spain.

The TJ-II [34] is a stellarator built at Ciemat in Madrid (Spain) with the first plasma launched in 1997. The device was designed in collaboration with the Oak Ridge National Laboratory (USA) and the IPP (Germany). Figure 1.4 shows a 3D representation of the TJ-II stellarator with the external coils (blue and orange) and plasma (purple). The structure of the coils is described as follows. One central coil which along it a set of 32 toroidal coils is distributed, the axis of the toroidal coils describing a helix. Then a helicoidal winding (orange) is wrapped around the central coil. Finally a set of vertical, radial and ohmic coils are used to control the position of the magnetic axis and compensate any not desirable magnetic field. Table 1.1 shows the basic characteristics of TJ-II plasmas.

One of the advantages of the TJ-II stellarator is that the currents in the coils can be adjusted allowing a large modification of the rotational transform ι. The range of ι values in the axes goes from 0.9 to 2.6.

Major radius R	1.5 m
Minor radius a	0.1∼0.25 m
Electron temperature T_e	0.3∼1 KeV
Electron density n_e	$\sim 10^{19} m^{-3}$
Magnetic field B	1T
Plasma pressure β_0	$\sim 10^{-3}$

Table 1.1: Basic properties of TJ-II plasmas.

The magnetic shear (the radial variation of ι) can be as well modified. Therefore the TJ-II is a useful tool to study transport and stability comparing different magnetic configurations.

There are two heating systems installed in the TJ-II. One is the Electron Cyclotron Resonance Heating (ECRH) for which high frequency waves are launched to the plasma and then electrons are heated through resonance. The other method is the Neutral Beam Injection (NBI) where a beam of neutral particles is fired into the plasma, the neutrals collide with other particles in the plasma and transfer them energy.

Diagnostics

The TJ-II is an experimental device so a large number of diagnostics are used to study the different discharges. In this work, we compare our numerical simulations with some experimental results. The results we are interested in are basically obtained by two different diagnostics: the ECE and Langmuir probes.

The Electron Cyclotron Emission (ECE) measures the electron temperature at different radial locations. It detects the cyclotron emission of the electrons and the intensity of this emission depends on the temperature. Moreover the radial position can be extracted if the magnetic field is known because the cyclotron frequency depends on that magnetic field [35]. In TJ-II there are 12 ECE channels which allow the measurement of electron temperature at different radius [36].

The other important diagnostic relevant to this work are the Langmuir probes. In general no direct measurements are possible in fusion devices because temperatures are extremely high and the diagnostics could be damaged and the plasma contaminated. However the Langmuir probes can measure the ion saturation current and the floating

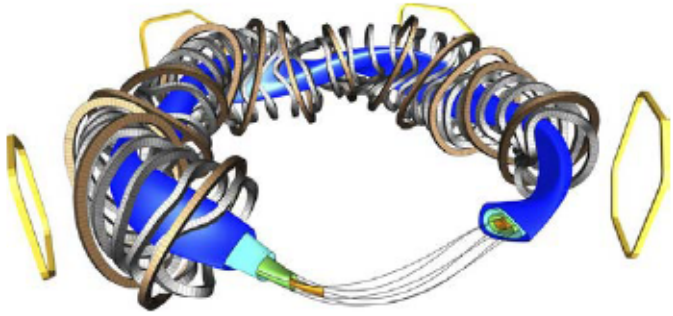

Figure 1.5: Schematic of the W7-X coils and plasma. Picture taken from Ref. [6] under a Creative Commons CC-BY license.

potential at the edge of the stellarator [37]. The probes can move very fast and have several pins which can measure the mentioned quantities.

1.2.3 W7-X

The Wendelstein 7-X (W7-X) is the largest stellarator in the world. It is located at the Max-Planck Institut für Plasmaphysik (IPP) in Greifswald (Germany) and started operation in December 2015. The design was based on the optimization of neoclassical transport and MHD stability [38]. Figure 1.5 shows a schematic of the W7-X experiment. All the superconducting coils contribute to the magnetic configuration, the grey coils are the non-planar, the brown coils are the planar and the yellow ones are the trim coils. Table 1.2 summarizes the basic properties of plasmas in the first campaign (known as OP1.1) in W7-X [39].

Plasma is heated using the ECRH providing a heating power up to 10MW and, in the future, a NBI heating system will be used in

Major radius R	5.5 m
Minor radius a	~0.49 m
Electron temperature T_e	5~6 KeV
Electron density n_e	$1 \sim 2 \cdot 10^{19} m^{-3}$
Magnetic field B	2.5T

Table 1.2: Basic properties of W7-X plasmas in the first campaigns [39].

the coming campaigns. Before the OP2 campaign a divertor will be installed. The W7-X device includes also a large number of diagnostics and the ECE and Langmuir probes (the ones we are interested) are present.

1.3 Transport in Fusion devices

One could think that, in a Magnetic Confinement Fusion device, restricting the particle movement using a magnetic field should be enough to keep the plasma confined, so the particles should be traveling along the field line and if the lines are tangent to a surface these particles should be trapped with minimal losses. However, that is not the case, during decades experiments have shown that transport in fusion devices is a very important issue. Strong transport reduces considerably the confinement time and hence the viability of a fusion reactor. Nowadays transport is not well understood yet and it is still analyzed by the fusion community.

There are three concepts in transport theory in fusion plasmas:

- *Classical transport.* The charged particles are moving along the magnetic field lines, however due to the Coulomb interaction they can collide with other particles. After many collisions, stochastically, the particles will displace to outward positions until they escape from the device.

- *Neoclassical transport.* As the particles are moving along the magnetic fusion device they feel a drift. There are several reasons as for example the presence of an electric field or the curvature or gradient of the magnetic field.

- *Turbulent transport.* For many years experiments have shown that transport is much higher than Neoclassical predictions, this phenomena was first called *anomalous transport.* The reason is the collective phenomena of the charged particles. Pressure or current gradients in the plasma can be the source of instabilities that enhance transport.

Turbulence has been observed as the main element in transport in most of fusion plasmas, experimental values show confinement times up to two order of magnitude lower than Neoclassical predictions [40].

This transport is "faster" and cannot be explained by diffusive (classical) theories. *Superdiffusive* transport was experimentally observed in different fusion devices [41]. Different theories have been proposed for several years to try to understand turbulent transport in fusion plasmas. Some of them were more traditional (like in physics of fluids) as the calculation of effective diffusivities which then are introduced in advective-diffusion equations. Others were novel approaches as the Self-Organized Criticality (SOC) paradigm which explains qualitatively some of the observations in turbulent transport. In SOC systems transport is generated by avalanches which are triggered by fluctuations [42]. SOC exhibits some of the characteristics in fusion plasmas as the Bohm scaling (transport scales with system size), profile stiffness or superdiffusive transport [43, 44].

Turbulent transport involves many drawbacks in fusion plasmas apart from the superdiffusive transport. It is suggested to be one of the causes of power degradation [45]. It means that the amount of energy confined in the plasma increases less than linearly with the heating power so the energy confinement time $\tau_E \propto P^{\alpha}$ where $\alpha \sim -0.6$. Furthermore the observation of the *Bohm scaling* is another issue related with turbulent transport. That experimental scaling showed that the confinement time was proportional to the minor radius $\tau_E \propto a$ which implied that for the desired confinement times the fusion reactor should be much larger (and not economically viable). That problem was partially solved by the introduction of transport barriers.

1.3.1 Transport barriers

The observation of the Bohm scaling was a seriour concern for the fusion program in the 70's. It implied a low confinement time which scaled with the size of the device, so this confinement regime was called L-mode. Fortunately in the early 80's a new (high) confinement regime, called H-mode, was discovered first in ASDEX [46] and then in other relevant Tokamaks. The H-mode was obtained when the input power surpassed a threshold (and a wall conditioning) and yielded to up to twice values of confinement time.

Figure 1.6.(a) illustrates qualitatively the different pressure profiles in the L-mode and H-mode in MCNF devices. The H-mode shows higher pressure values however the gradient is identical to the L-mode in the inner regions. We can reach these high values in the H-mode

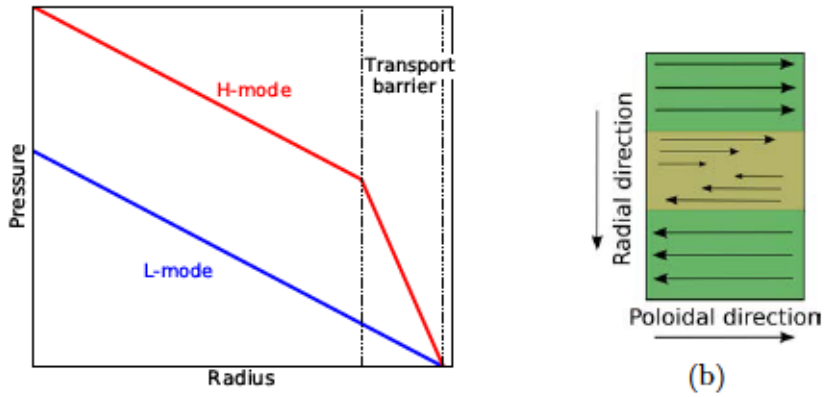

Figure 1.6: (a) Pressure profiles for Low and High confinement modes. (b) Transport barrier.

due to the generation of a transport barrier at the edge which reduces considerably the turbulent transport in the core. The physical mechanism of a transport barrier consists in a spatial region where the plasma velocity changes radially. That radial shear of the velocity produces the transport barrier. An example of shear in the flow is shown in Fig. 1.6.(b). Two radial regions (top and bottom) in the plasma are rotating at different velocities and the middle region is a transition area where velocity is changing so a radial shear of the velocity appears. This shear region works as a barrier and suppresses turbulence so transport becomes diffusive [47, 48].

In the H-mode, a transport barrier is present at the edge where the plasma rotates at different velocities. The rotation is caused by the presence of a radial electric field at the edge which generates an $\boldsymbol{E}\times\boldsymbol{B}$ flow in the poloidal direction. Moreover in the last decades, using the same mechanism, the generation of Internal Transport Barriers (ITB) have been observed and it has been suggested as a method to reduce turbulent transport in fusion plasmas.

The presence of a transport barrier at the edge in the H-mode allows higher pressure values and suppresses turbulent transport. However it implies the formation of a steep gradient at the edge which yields to the Edge-Localized-Modes (ELMs). The ELMs are a kind of instability that ejects large amounts of energy and particles to the wall [49]. They are a serious issue in large tokamaks (as ITER) because

the wall components can be damaged.

1.3.2 Perturbative methods

A simple idea to analyze turbulent transport in a stationary fluid is to follow the particle movement. For example, one can throw a leaf to the river and follow the leaf trajectory over time. This way we could identify regions where the leaf moves faster or the location of eddies where the leaf could be trapped. Analogously that is how the perturbative methods work in a fusion plasma. A perturbation is set at some location and its time evolution is analyzed.

Perturbative methods are one of the most used methods to study heat transport in experimental fusion plasmas. They have been used in several devices as for example Tore Supra [50], DII-D [51], ASDEX Upgrade [52], JET [53] and W7-AS [54]. The idea of these methods is to introduce one (or a set of intermittent) heat perturbation in the plasma and then analyze the plasma response and the time evolution of the perturbations [55, 56, 57].

Measuring transport in a turbulent fluid is complicated but it is even more difficult in fusion plasmas due the extreme temperatures in the core which makes impossible direct measurement in the inner regions. All the measurements are from electromagnetic emissions or using probes at the edge regions where temperatures are lower.

1.4 The aim of this work

In this thesis we propose an approach based on the Transfer Entropy (TE) technique to study heat transport in turbulent plasmas in MCNF devices. We apply the technique to numerical results of a resistive MHD model (Chapter 2) which simulates the plasma condition in the stellarators TJ-II (Chapter 4) and W7-X (Chapter 5). The aim is to validate and interpret the experimental results with our simulations.

Chapter 3 is dedicated to the description of the Transfer Entropy. The technique is new in plasma physics and the reader may not be familiar with the TE so the chapter introduces it from the field of information theory. Then some examples are provided in order to understand these tool and show their advantages.

During this work we observe that heat transport is modified by the

presence of transport barriers at different radial regions. We suggest that these transport barriers are caused by the radial shear in the perpendicular flow. Chapter 7 analyze how the perpendicular flow is generated in the plasma. The flow is produced by the turbulent vortices due the resistive interchange plasma instabilities.

The Transfer Entropy is used to identify and characterize filamentary structures in the plasma (in this case the turbulent vortices). In Chapter 8 the TE is applied to our numerical simulations to compare an interpret the physics underlying the experimental results in TJ-II. Similarly, in Chapter 9, the TE is used as well to study and characterize filamentary structures in simulations of W7-X plasmas.

Chapter 2

Model equations

In this Chapter we describe the model used to simulate fusion plasmas in TJ-II and W7-X stellarators in the next chapters. The model is based on the MagnetoHydrodynamic (MHD) theory, in our studies the resistive interchange modes are the most dominant instability. It is not the aim of our model to fully describe plasmas in real stellarators but to provide a (relatively easy) model where the basic plasma physics is present. The model has to be seen as a tool to simulate the fundamental physics in the mentioned stellarators and extract qualitatively some of their main properties.

First we introduce the MHD theory which describes (under some assumptions) plasma physics in fusion devices. Then the main instabilities which can occur in plasmas are defined with emphasis in the relevant instability in our studies, the interchange modes. The equations which govern our plasma simulations are explained in different sections. Finally the numerical code used to simulate the theoretical model, FAR, is presented indicating the main characteristics.

A summary of the model equations is given in Sec. 2.3.5.

2.1 MagnetoHydroDynamics

The kinetic theory describes how the particles interact with the electromagnetic fields. The particles are represented by their distribution functions $f_\alpha(\boldsymbol{r}, \boldsymbol{u}, t)$ (α indicates each species) and are governed by

the Boltzmann equation [25]

$$\frac{\partial f_\alpha}{\partial t} + \boldsymbol{u} \cdot \nabla f_\alpha + \frac{q_\alpha}{m_\alpha}(\boldsymbol{E} + \boldsymbol{u} \times \boldsymbol{B}) \frac{\partial f_\alpha}{\partial \boldsymbol{u}} = \left(\frac{\partial f_\alpha}{\partial t}\right)_C \tag{2.1}$$

where the first two terms on the left side are the convective derivative, the third term includes the electromagnetic forces and the right hand side represents the collisions. So with Eq. 2.1 and the Maxwell's equations should be enough to study the plasma.

In spite of the apparent simplicity of Eq. 2.1, it can be an arduous work to solve it from the computational point of view. The kinetic theory illustrates in detail the microscopic dynamics, however for the global behavior of the plasma a simpler model based on macroscopic quantities should be enough. The MagnetoHydroDynamic (MHD) model has been used for decades to study plasma physics in fusion devices. The model characterizes the plasma as a fluid and this fluid assumption is correct if particle collisions are high enough.

Therefore a set of macroscopic variables is defined as

$$n_\alpha \equiv \int f_\alpha d\boldsymbol{u} \tag{2.2}$$

$$\boldsymbol{v}_\alpha \equiv \frac{1}{n_\alpha} \int \boldsymbol{u} f_\alpha d\boldsymbol{u} \tag{2.3}$$

$$p_\alpha \equiv \frac{1}{3} m_\alpha \int |\boldsymbol{v}_\alpha - \boldsymbol{u}|^2 f_\alpha d\boldsymbol{u} \tag{2.4}$$

$$T_\alpha \equiv \frac{p_\alpha}{n_\alpha} \tag{2.5}$$

where n_α is the density, $\boldsymbol{v}_\alpha$ is the velocity, p_α is the pressure and T_α is the temperature. The charge density σ and current $\boldsymbol{J}$ are

$$\sigma = \sum_\alpha q_\alpha \int f_\alpha d\boldsymbol{u} \tag{2.6}$$

$$\boldsymbol{J} = \sum_\alpha q_\alpha \int \boldsymbol{u} f_\alpha d\boldsymbol{u}. \tag{2.7}$$

The main assumptions for the derivation of the MHD model are:

- High collisionality to consider plasma as a fluid.

- Quasineutrality. An immediate electric field appears to keep this quasineutrality if there is a macroscopic separation of charges. $n_i = n_e$
- Mass fluid is mainly due to ions.
- Displacement current is zero. Waves in the plasma are much slower than speed of light.
- Fluid velocity is approximately the ion velocity $\boldsymbol{v} = \boldsymbol{v_i}$.
- Pressure is the sum of pressure from both species $p = p_i + p_e$.
- Plasma current is $\boldsymbol{J} = en\,(\boldsymbol{v_i} - \boldsymbol{v_e})$.
- Small ion Larmor radius.

After some calculations [27], one obtains the set of MHD equations

$$\frac{\partial \rho}{\partial t} + \nabla \cdot \rho \boldsymbol{v} = 0 \tag{2.8}$$

$$\rho \frac{d\boldsymbol{v}}{dt} = \boldsymbol{J} \times \boldsymbol{B} - \nabla p \tag{2.9}$$

$$\frac{d}{dt}\frac{p}{\rho^\gamma} = 0 \tag{2.10}$$

$$\boldsymbol{E} + \boldsymbol{v} \times \boldsymbol{B} = \eta \boldsymbol{J} \tag{2.11}$$

$$\nabla \times \boldsymbol{B} = \mu_0 \boldsymbol{J} \tag{2.12}$$

which are the equation of mass conservation, momentum balance equation, energy equation, Ohm's law and Ampère's law respectively. The convective derivatives can be written as

$$\frac{d}{dt} = \frac{\partial}{\partial t} + \boldsymbol{v} \cdot \nabla. \tag{2.13}$$

In Fusion plasmas the high collisionality assumption is not completely fulfilled, however the presence of a strong magnetic field is enough to keep the particles as a fluid at least in the perpendicular direction.

The resistivity η in Eq.2.11 is, in general, small in fusion plasmas and, as a first approximation, it can be considered as zero so the model

is called *ideal* MHD. It has an importance consequence, if the resistivity is zero then the magnetic flux is conserved. This implies that the magnetic field lines are "frozen" in the plasma so if the plasma moves the field lines moves with it. On the other hand, even if it is very small, the presence of resistivity will allow the diffusion of field lines within the plasma. This diffusion may lead to more favorable energetic states and to a *reconnection* of field lines . Magnetic reconnection changes the topology of the magnetic field. Disruptions and the sawtooth relaxation in Tokamaks are explained through magnetic reconnection [58].

2.2 Plasma stability

The MHD model in Sec. 2.1 is used to find first a static equilibrium in steady state plasmas so $d/dt = 0$. An important consequence is that in equilibrium

$$\boldsymbol{J} \times \boldsymbol{B} = \nabla p \tag{2.14}$$

which is a balance between Lorentz force and pressure gradients. It implies that $\boldsymbol{J}$ and $\boldsymbol{B}$ are perpendicular to ∇p so current and magnetic field lie on constant pressure surfaces so called *flux surfaces*. Furthermore the study of MHD equilibrium with external fields set the possible magnetic confinement devices to reach a steady state plasma.

Once the plasma is in equilibrium its stability should be analyzed because if a fluctuation or force appears in the plasma it is important to know if this perturbation will increase or decrease. If the forces induced by the perturbation make it grow then the plasma is unstable. On the other hand if the forces generated by the perturbation tend to restore the plasma to the equilibrium state then the plasma is stable. Stability is crucial in the design and operation of a fusion device because stabilities may reduce plasma confinement or even damage the device.

There are two sources of instabilities in plasmas, one is the *parallel current* and the other is the *pressure gradient*. So to prevent instabilities we should avoid toroidal currents and strong pressure gradients. However, that is complicated because in real devices we need a toroidal current to operate a Tokamak and, in all the devices high pressure values (so strong gradients) in the core are required to have a viable fusion reactor. Therefore, as these instabilities are not easy to avoid, plasma

stability has to be analyzed in detail to set the right parameters to minimize the consequences of these instabilities.

The current-driven instabilities are the ones which source is the parallel current $J_{\parallel}$. These instabilities are not relevant in stellarators due the lack of toroidal current, however they are important for example in tokamaks. So as we are simulating plasmas in the W7-X and TJ-II stellarator, we are focusing in the pressure-driven instabilities.

2.2.1 Pressure-driven instabilities

Pressure-driven instabilities are caused by pressure gradients in confined plasmas. These instabilities can exist even if there is no parallel current. Traditionally they are divided in two subcategories: interchange modes and ballooning modes.

Interchange modes

Usually interchange modes are compared with the Rayleigh-Taylor instability which is observed when a more dense fluid is above a less dense one. However for the interchange instability, the role of the gravity is played by the curvature of the magnetic field. So a perturbation "interchanges" two fluid tubes at different radial locations.

These instabilities are nearly constant along a magnetic field line and its short perpendicular wavelength makes them to be localized in radius. Furthermore they are localized in the main rational surfaces. They become unstable if the average magnetic curvature is unfavorable so the magnetic configurations must be chosen properly to avoid these instabilities. Conditions for stability are given by the Mercier criterion which corresponds to the limit when the width of the mode tends to zero. Shear in the magnetic field contributes to stabilize the interchange mode because it implies a line bending to interchange two flux tubes and that bending is a stabilizing effect (it consumes energy).

Interchange modes are not important in Tokamaks because the average magnetic curvature is favorable. However, in stellarators, for certain magnetic configurations the average curvature may be unfavorable.

Ballooning modes

Ballooning modes are also pressure-driven instabilities. Magnetic field lines around the toroidal device vary between favorable and unfavorable curvature. This perturbation is located in the unfavorable regions. So these modes can be unstable even if the average magnetic curvature is favorable.

This instability determines a maximum value for β in the devices. Ballooning modes are important for Tokamaks and stellarators

2.3 Reduced MHD model

In this thesis we simulate plasmas in the TJ-II (and W7-X) device and then we analyze the numerical results with different techniques. Most of our results are qualitative so there is no need to use more precise models, here we are interested in the essential physics in these plasmas. Therefore this model has to be seen as a tool to obtain the main characteristic observed in those fusion devices.

In the TJ-II the most dominant instabilities are the interchange modes which are characterized by their flute-like pattern. They become unstable when the average magnetic curvature is unfavorable. Reduced MHD equations are used here in the Greene and Johnson formalism [59] and a straight helical system is assumed within a cylindrical geometry. The aim of the reduced MHD equations is to describe the fundamental physics with the minimum number of variables [60], this way the model is more manageable than the MHD theory.

An initial (simplified) version of this model was presented in Ref. [61] where the resistive pressure-driven instabilities were analyzed analytically and numerically. In Ref. [62] the diamagnetic effects were introduced and the plasma rotation was studied. Then, in Ref. [63] the equations of density and electron temperature were set in order to analyze TJ-II plasmas. The latter reference uses exactly the model described in this section.

We now describe the approximations used in this model and how the equations are obtained.

2.3.1 Flute perturbations

Imagine an arbitrary perturbation of some variable $x(\boldsymbol{r}, t)$ in a toroidally confined plasma. The geometry of the systems allows the Fourier decomposition

$$x(r, \theta, \zeta, t) = \sum_{m,n} x_{m,n}(r, \theta, \zeta, t) \exp\left[i(m\theta - n\zeta)\right] \tag{2.15}$$

where (r, θ, ζ) are flux coordinates. Any perturbation will involve several components due the toroidicity and the nonlinear coupling, however in a linear and cylindrical system one mode could represent the perturbation. In spite of the coupling, the perturbation usually is dominated by a single harmonic with a wave vector

$$\boldsymbol{k} = m\nabla\theta - n\nabla\zeta \tag{2.16}$$

where the integers m and n are the poloidal and toroidal mode numbers respectively. The ratio m/n identifies the helicity of the harmonic. Note that the helicity of the magnetic field lines in the plasma can be characterized by the safety factor q which in flux coordinates is

$$\frac{\boldsymbol{B} \cdot \nabla\theta}{\boldsymbol{B} \cdot \nabla\zeta} = \frac{1}{q(r)}. \tag{2.17}$$

We define a unit vector $\boldsymbol{b}$ aligned with the magnetic field $\boldsymbol{B}$ as

$$\boldsymbol{b} = \frac{\boldsymbol{B}}{B}. \tag{2.18}$$

In Fusion plasmas, the most dangerous perturbations are the ones aligned with the magnetic field so we call them flute perturbations because its *flute-like* behavior. The parallel wave vector $k_\parallel$ is zero if the perturbation is aligned to the magnetic field. So using Eq. 2.17 the parallel wave vector is

$$k_\parallel = \boldsymbol{b} \cdot \boldsymbol{k} = \frac{\boldsymbol{B} \cdot \nabla\theta}{B}(m - nq). \tag{2.19}$$

Note that at certain radius q may be a rational number $q = m/n$ so the parallel wave vector vanishes.

In general, for flute perturbations the parallel wave vector is small so

$$k_\parallel << k_\perp. \tag{2.20}$$

Our model uses the *flute reduction* [64] which assumes that

$$k_{\parallel} = \mathcal{O}(\varepsilon k_{\perp}) \tag{2.21}$$

where ε is a small parameter so variables and derivatives can be expanded in term of this parameter. This ordering allows to simplify the expressions and neglect small terms.

2.3.2 Magnetic flux equation

Starting from the Ohm's law

$$\boldsymbol{E} + \boldsymbol{v} \times \boldsymbol{B} = \eta \boldsymbol{J} \tag{2.22}$$

at the lowest order and multiplying it by a unitary magnetic field $\boldsymbol{b} = \boldsymbol{B}/B$ we can approximate

$$-\boldsymbol{b} \times \nabla\Phi + B\boldsymbol{b} \times (\boldsymbol{v} \times \boldsymbol{b}) \simeq 0. \tag{2.23}$$

Therefore the perpendicular velocity is

$$\boldsymbol{v}_{\perp} = -\frac{1}{B}\nabla\Phi \times \boldsymbol{b} \tag{2.24}$$

which is the well known $\boldsymbol{E} \times \boldsymbol{B}$ velocity.

The magnetic field in the plasma can be written with a parallel and perpendicular components as

$$\boldsymbol{B} = \nabla\zeta \times \nabla\psi + F\boldsymbol{\zeta} \tag{2.25}$$

so the F is the equilibrium magnetic field and the ψ is the poloidal magnetic flux. We do not include the F component because its parallel gradient is small.

From Faraday's law

$$\nabla \times \boldsymbol{E} = -\frac{\partial \boldsymbol{B}}{\partial t} = -\frac{\partial}{\partial t}(\nabla\zeta \times \nabla\psi) = \frac{\partial}{\partial t}\nabla \times (\psi\nabla\zeta) \tag{2.26}$$

so

$$\boldsymbol{E} = -\nabla\Phi + \frac{\partial\psi}{\partial t}\nabla\zeta. \tag{2.27}$$

Multiplying the Ohm's law (Eq. 2.22) by $\boldsymbol{b}$

$$E_{\parallel} = \eta J_{\parallel} \tag{2.28}$$

so if we apply Eq. 2.27 we obtain

$$-\boldsymbol{b}\cdot\nabla\Phi+\boldsymbol{b}\cdot\nabla\zeta\frac{\partial\psi}{\partial t}=\eta J_{\parallel} \tag{2.29}$$

which can be rewritten as and equation for the time evolution of the poloidal magnetic flux

$$\frac{\partial\psi}{\partial t}=\nabla_{\parallel}\Phi+\eta J_{\parallel}. \tag{2.30}$$

However, for this ordering, this reduced MHD model does not include some relevant physical effects. The rotation of electromagnetic perturbations at the diamagnetic frequency has been observed and is a stabilizing contribution. Using the Braginskii equations (see Ref. [65]), an extra term appears in the Ohm's law,

$$E_{\parallel}=\eta J_{\parallel}-\frac{1}{ne}\nabla_{\parallel}p. \tag{2.31}$$

We are using this model to simulate plasmas in the stellarators TJ-II and W7-X. In both devices our simulations are compared with discharges heated by ECRH so we assume the ion temperature is low. Thus, the plasma pressure is given mainly by electron pressure so

$$p=p_e=n_eT_e. \tag{2.32}$$

Therefore the time evolution of the poloidal magnetic flux equation becomes

$$\boxed{\frac{\partial\psi}{\partial t}=\nabla_{\parallel}\Phi-\frac{1}{ne}\left(T_e\nabla_{\parallel}n+n\nabla_{\parallel}T_e\right)+\eta J_{\parallel}.} \tag{2.33}$$

2.3.3 Momentum balance equation

Stability from plasma equilibrium can be analyzed using the *shear-Alfvén law*. It exhibits the essential dynamics of the plasma from the momentum equation (Eq. 2.9). A full demonstration of this expression can be found in Ref. [64]. The exact shear-Alfvén law is

$$\frac{\boldsymbol{b}}{B}\cdot\nabla\times\left(\rho\frac{d\boldsymbol{v}}{dt}\right)-2\frac{\boldsymbol{b}\times\boldsymbol{\kappa}}{B}\cdot\rho\frac{d\boldsymbol{v}}{dt}=\boldsymbol{B}\cdot\nabla\left(\frac{J_{\parallel}}{B}\right)+2\frac{\boldsymbol{b}\times\boldsymbol{\kappa}}{B}\cdot\nabla p. \tag{2.34}$$

The left hand side of Eq. 2.34 illustrates the plasma inertia. The right hand side describes the driving forces (sources of free energy)

which plasma is experiencing. The first term on the right hand side involves the parallel current and is the origin of the current driven modes. In fact this term has two contributions, one describes the gradient in the equilibrium parallel current which yields to kink instabilities and the other one reflects the bending of magnetic field lines. In our model there is no parallel current (in equilibrium) but perturbations are possible. That perturbation of parallel current generates a perpendicular magnetic field (Ampère's law) which bend the field lines. The line bending is a stabilizing effect (energy bending field lines is not available for fluid motion) but this term is small near rational surfaces [64].

The second term in right hand side of Eq. 2.34 contains the pressure gradient and is the source of the pressure driven modes. The stability of this term depends on the magnetic curvature and pressure gradient so if $\boldsymbol{\kappa}\cdot\nabla P > 0$ the term becomes unstable and this curvature is called *unfavorable*.

Our model seeks to simulate interchange instabilities in a stellarator using a cylindrical geometry. This type of instability becomes unstable if the average magnetic curvature is unfavorable. So in this model the curvature $\boldsymbol{\kappa}$ is the average curvature which depends only on the radius

$$\boldsymbol{\kappa} = \kappa(r)\,\hat{\boldsymbol{r}}. \tag{2.35}$$

The variables in the model can be decomposed in an equilibrium and fluctuating part so

$$x = x_{eq} + \tilde{x} \tag{2.36}$$

where the subindex "eq" indicates the equilibrium component and the tilde the fluctuating part. The shear-Alfvén law can be rewritten in terms of the fluctuating part of the variables. The second term on the left hand side can be neglected because the contribution of the right hand side is much higher so

$$\frac{\boldsymbol{b}}{B}\cdot\nabla\times\left(\rho\frac{d\tilde{\boldsymbol{v}}}{dt}\right) = \boldsymbol{B}\cdot\nabla\left(\frac{\tilde{J}_{\parallel}}{B}\right) + 2\kappa\frac{\boldsymbol{b}\times\hat{\boldsymbol{r}}}{B}\cdot\nabla\tilde{p}. \tag{2.37}$$

The advective derivative is

$$\frac{d}{dt} = \frac{\partial}{\partial t} + \boldsymbol{v}_{\perp}\cdot\nabla \tag{2.38}$$

The curl of the velocity suggest the introduction of the vorticity so the parallel component of the vorticity is

$$U = \boldsymbol{b} \cdot \nabla \times \boldsymbol{v} = \boldsymbol{b} \cdot \nabla \times \boldsymbol{v}_\perp \tag{2.39}$$

and using Eq. 2.24 the U can be written as

$$U = \nabla_\perp^2 \Phi \tag{2.40}$$

where in cylindrical coordinates

$$\nabla_\perp^2 = \frac{1}{r}\frac{\partial}{\partial r}\left(r\frac{\partial}{\partial r}\right) + \frac{1}{r^2}\frac{\partial^2}{\partial \theta^2}. \tag{2.41}$$

The parallel gradient operator in this flute approximation is

$$\nabla_\parallel \equiv \frac{\boldsymbol{B} \cdot \nabla}{B_0}. \tag{2.42}$$

The momentum balance is then

$$\rho\left(\frac{\partial \tilde{U}}{\partial t} + \boldsymbol{v}_\perp \cdot \nabla \tilde{U}\right) = B\nabla_\parallel \tilde{J}_\parallel + 2\kappa\hat{\boldsymbol{\theta}} \cdot \nabla \tilde{p}. \tag{2.43}$$

As we have already seen, the plasma pressure is given mainly by electron pressure so $p = p_e = n_e T_e$. Then the momentum balance equation is finally

$$\boxed{\rho\left(\frac{\partial \tilde{U}}{\partial t} + \boldsymbol{v}_\perp \cdot \nabla \tilde{U}\right) = B\nabla_\parallel \tilde{J}_\parallel + \kappa\left(T_{eq}\frac{1}{r}\frac{\partial \tilde{n}}{\partial \theta} + n_{eq}\frac{1}{r}\frac{\partial \tilde{T}_e}{\partial \theta}\right) + \mu\nabla_\perp^2 \tilde{U}} \tag{2.44}$$

where a dissipative term $\mu\nabla_\perp^2 \tilde{U}$ is added corresponding to the viscosity.

2.3.4 Density and electron temperature equations

Now evolution equations for density and electron temperature are required. So for the density

$$\frac{d\tilde{n}}{dt} = D_\perp \nabla_\perp^2 \tilde{n} \tag{2.45}$$

where $D_\perp$ is the perpendicular diffusion and we assume that the parallel diffusivity is small. Adding the diamagnetic effects (see Ref. [65]) and the advective derivative we obtain

$$\boxed{\frac{\partial \tilde{n}}{\partial t} = -\boldsymbol{v}_\perp \cdot \nabla n + \frac{1}{|e|}\nabla_\parallel \tilde{J}_\parallel + D_\perp \nabla_\perp^2 \tilde{n}.} \tag{2.46}$$

For the electron temperature

$$\frac{d\tilde{T}_e}{dt} = \chi_\perp \nabla_\perp^2 \tilde{T}_e + \nabla_\parallel \left(\chi_\parallel \nabla_\parallel T_e\right) \tag{2.47}$$

where $\chi_\perp$ is the perpendicular electron heat conductivity and $\chi_\parallel$ is the parallel conductivity which may be radial dependent. Including the diamagnetic effects and expanding the advective derivative we get

$$\boxed{\frac{\partial \tilde{T}_e}{\partial t} = -\boldsymbol{v}_\perp \cdot \nabla T_e + \frac{T_{eq}}{|e| n_{eq}}\nabla_\parallel \tilde{J}_\parallel + \chi_\perp \nabla_\perp^2 \tilde{T}_e + \nabla_\parallel \left(\chi_\parallel \nabla_\parallel T_e\right).} \tag{2.48}$$

2.3.5 Summary of the model

The four equations of the model are summarized here in their dimensionless form

$$\boxed{\begin{aligned}
\frac{\partial \tilde{\psi}}{\partial t} &= \nabla_\parallel \Phi - S\bar{\omega}_{*e}\left(\frac{T_{eq}}{n_{eq}}\nabla_\parallel \tilde{n} + \nabla_\parallel \tilde{T}_e\right) + \eta \tilde{J}_\parallel, && (2.49)\\
\frac{\partial \tilde{U}}{\partial t} &= -\boldsymbol{v}_\perp \cdot \nabla U + S^2 \nabla_\parallel \tilde{J}_\parallel \\
&\quad - S^2 \frac{\beta_0}{2\varepsilon^2}\kappa\left(\frac{T_{eq}}{n_{eq}}\frac{1}{r}\frac{\partial \tilde{n}}{\partial \theta} + \frac{1}{r}\frac{\partial \tilde{T}_e}{\partial \theta}\right) + \mu \nabla_\perp^2 \tilde{U}, && (2.50)\\
\frac{\partial \tilde{n}}{\partial t} &= -\boldsymbol{v}_\perp \cdot \nabla n + \frac{S}{\bar{\omega}_{ci}}\nabla_\parallel \tilde{J}_\parallel + D_\perp \nabla_\perp^2 \tilde{n}, && (2.51)\\
\frac{\partial \tilde{T}_e}{\partial t} &= -\boldsymbol{v}_\perp \cdot \nabla T_e + \frac{S}{\bar{\omega}_{ci}}\frac{T_{eq}}{n_{eq}}\nabla_\parallel \tilde{J}_\parallel + \chi_\perp \nabla_\perp^2 \tilde{T}_e \\
&\quad + \nabla_\parallel \left(\chi_\parallel \nabla_\parallel Te\right). && (2.52)
\end{aligned}}$$

which are the magnetic poloidal flux equation, momentum balance, density and electron temperature equation respectively. The four variables in the model are the magnetic poloidal flux ψ, the electrostatic

potential Φ, the densiy n and the electron temperature T_e. The parallel component of the vorticity is

$$U = \nabla_\perp^2 \Phi \tag{2.53}$$

and the parallel current is

$$J_\parallel = \nabla_\perp^2 \psi. \tag{2.54}$$

The parallel gradient is

$$\nabla_\parallel = \frac{\partial}{\partial \zeta} - \frac{1}{q}\frac{\partial}{\partial \theta} + \frac{\partial \tilde{\psi}}{\partial r}\frac{1}{r}\frac{\partial}{\partial \theta} - \frac{1}{r}\frac{\partial \tilde{\psi}}{\partial \theta}\frac{\partial}{\partial r} \tag{2.55}$$

and

$$\nabla_\perp^2 = \frac{1}{r}\frac{\partial}{\partial r}\left(r\frac{\partial}{\partial r}\right) + \frac{1}{r^2}\frac{\partial^2}{\partial \theta^2}. \tag{2.56}$$

The perpendicular velocity is

$$\boldsymbol{v}_\perp = -\nabla\Phi \times \hat{\boldsymbol{\zeta}} \tag{2.57}$$

which yields to

$$v_r = -\frac{1}{r}\frac{\partial \Phi}{\partial \theta}, \qquad v_\theta = \frac{\partial \Phi}{\partial r}. \tag{2.58}$$

The tildes in the variables indicate the fluctuations from an equilibrium so

$$x = x_{eq} + \tilde{x}. \tag{2.59}$$

The resistivity is η, the viscosity is μ and the perpendicular diffusivity is $D_\perp$. $\chi_\parallel$ and $\chi_\perp$ are the parallel and perpendicular thermal diffusivity, respectively. The inverse aspect ratio is $\varepsilon = a/R_0$. B_z is the z component of the magnetic field and $\beta_0 = 2\mu_0 p(0)/B_z^2$. The magnetic field line curvature κ includes the averaged effect of the toroidal and helical components of the magnetic field.

The Lundquist number is $S = \tau_R/\tau_A$. The poloidal Alfvén time is $\tau_A = R_0\sqrt{\mu_0 m_i n_i}/B_z$, where m_i and n_i are the ion mass and density, respectively. The resistive time is $\tau_R = \mu_0 a^2/\eta(0)$ where $\eta(0)$ is the resistivity at the magnetic axis. The normalized frequencies are $\bar{\omega}_{*e} = \tau_A \omega_{*e}$ and $\bar{\omega}_{ci} = \tau_A \omega_{ci}$, where $\omega_{*e} = T_e/(ea^2 B_z)$ and $\omega_{ci} = eB_z/m_i$ are the electron diamagnetic frequency and the ion cyclotron frequency respectively.

Length in this model is given in units of the minor radius a and the time is given in units of resistive time τ_R.

Interpretation

The model equations are

$$\frac{\partial \tilde{\psi}}{\partial t} = \nabla_\parallel \Phi - S\bar{\omega}_{*e}\left(\frac{T_{eq}}{n_{eq}}\nabla_\parallel \tilde{n} + \nabla_\parallel \tilde{T}_e\right) + \eta \tilde{J}_\parallel, \tag{2.60}$$

$$\frac{\partial \tilde{U}}{\partial t} = -\boldsymbol{v}_\perp \cdot \nabla U + S^2 \nabla_\parallel \tilde{J}_\parallel - S^2 \frac{\beta_0}{2\varepsilon^2}\kappa\left(\frac{T_{eq}}{n_{eq}}\frac{1}{r}\frac{\partial \tilde{n}}{\partial \theta} + \frac{1}{r}\frac{\partial \tilde{T}_e}{\partial \theta}\right) + \mu \nabla_\perp^2 \tilde{U}, \tag{2.61}$$

$$\frac{\partial \tilde{n}}{\partial t} = -\boldsymbol{v}_\perp \cdot \nabla n + \frac{S}{\bar{\omega}_{ci}}\nabla_\parallel \tilde{J}_\parallel + D_\perp \nabla_\perp^2 \tilde{n}, \tag{2.62}$$

$$\frac{\partial \tilde{T}_e}{\partial t} = -\boldsymbol{v}_\perp \cdot \nabla T_e + \frac{S}{\bar{\omega}_{ci}}\frac{T_{eq}}{n_{eq}}\nabla_\parallel \tilde{J}_\parallel + \chi_\perp \nabla_\perp^2 \tilde{T}_e + \nabla_\parallel\left(\chi_\parallel \nabla_\parallel Te\right). \tag{2.63}$$

where the red terms are the dissipative terms corresponding to resistivity, viscosity and diffusivity. The blue ones are the diamagnetic effects. The magenta term is generating the drive (trough the pressure gradient). The green one is the stabilizing term due the perturbations in the parallel current.

2.3.6 Numerical code: FAR

The equations of the model are solved using a numerical code called FAR (Finite Aspect Ratio) [66]. It inherits the main numerical method of KITE code [67]. FAR is able to run in a toroidal geometry although in this work only a cylindrical is studied.

The variables are decomposed in Fourier decomposition for the poloidal and toroidal angle and the radial direction is solved using finite differences so

$$f(r,\theta,\zeta,t) = \sum_{m,n}\left[f^s_{m,n}(r,t)\sin(m\theta + n\zeta) + f^c_{m,n}(r,t)\cos(m\theta + n\zeta)\right]. \tag{2.64}$$

The code uses an implicit method to advance the equations. However the nonlinear terms are explicitly added at each time step using a predictor-corrector method. For a more details of the code see Appendix A.

Chapter 3

Transfer entropy

The Transfer Entropy (TE) technique is broadly used in this thesis to analyze the numerical results obtained by the MHD code. The technique is relatively new in Plasma Physics for Nuclear Fusion. The aim of this chapter is to introduce and describe the TE and then provide some examples on how the technique is applied. For a detailed description of how the Transfer Entropy is actually calculated see Appendix B.

One of the basic ideas in Physics is not only study a phenomena and make predictions but also find the cause of that phenomena. Imagine a system where different physical magnitudes can be measured, one variable is perturbed and after some (usually short) time other variable is affected. We could establish a causality relation between these variables and formulate our theory/model. This assumption of causality can be straightforward for a simple system, as for example the force between two charged particles, but can be extremely complicated for a non linear system as a fluid.

The traditional methods (linear correlation, conditional averaging [68],...) are conceived to identify a relation between variables. They analyze previous events and determine if they are relevant in future events. However not always the causality relation is identified or it may lead to confusing conclusions because these techniques frequently rely in our first assumption of cause-effect. Furthermore, as it is well known, *correlation does not imply causation*. Here we present a new technique which goal is to establish a causal relation between two processes.

The Transfer Entropy [69] was introduced in the field of Informa-

tion theory as a measure of *causality*. The use of the word *causality* in science can be controversial, its colloquial sense is basically: "If X happens then Y will occur" or in the other way "we observed Y so X occurred". That is the philosophical sense of *cause-effect* and it is an abstract concept easy to understand but extremely difficult to quantify. In this work we use the *Granger causality* definition (introduced by Wiener) [70, 71] which states: "Having two signals X and Y, if we can predict better signal X using the past information from signal Y than without it, then Y causes X". Therefore the Transfer Entropy is measuring the information contained in two signals and quantifies the information flow between them.

In a sense, the Transfer Entropy is measuring the information from previous events from two processes and establish (if exist) a causal relation between those processes. The technique identifies if the previous information in signal Y is affecting future events in X, but taking into account as well the previous information contained in X itself.

The Transfer Entropy was originally applied by Schreiber in physiological time series [69]. The technique has been used in many fields as neurosciences [72], biochemistry [73], control systems [74] and even financial markets [75]. The Transfer Entropy was applied for the first time in Fusion Plasmas in Ref. [76] which lead to other works (as Ref. [77]) in TJ-II and W7-X plasmas (see references in the next chapters). The technique has been as well applied to tokamak experiments in Ref. [78] by an independent group.

3.1 Introduction

In thermodynamics the concept of entropy was established by R. Clausius in the XIX century. Its original idea was to quantify the amount of energy (per unit of temperature) which cannot be used in a thermodynamic process and, at the same time, to measure the irreversibility of a system. At the beginning of the XX century L. Boltzmann (and others) developed the main ideas of the statistical mechanics. In particular he gave a more precise description of the concept of entropy as a measure of the randomness of a system. Its famous expression is

$$S = -k_B \ln \Omega$$

where S is the entropy, k_B is the Boltzmann constant and Ω is the number of possible microstates in the system.

However, in this thesis, we focus in the *entropy* as it is used in the field of Information theory. In the 1940 decade, the Information theory was developed by Claude E. Shannon [79] (reprinted in [80]). During that time computational science and telecommunications were as well developing, information theory was introduced as an approach to measure the information in communications. According to Shannon [81, 82], a measure of *information* should have these properties:

- It is additive. Therefore, if the signal is larger, the information should increase.
- It should express in some way the number of possible events and their respectively likelihood.
- It should be continuous. A small change in the probability of an event should generate, as well, a small change in the information.
- If all the events are equally likely then its value is maximum.

Entropy was defined as a measure of the average uncertainty of a value in a message. So it is calculating *information* as form of uncertainty. Shanon choose the term *entropy* (used in thermodynamics and statistical mechanics) to emphasize the concept of an uncertainty function, as it was suggested by John von Neumann [83]. The Shannon Entropy H is defined as

$$H = -\sum_{i=1}^{n} p_i \log_2 p_i \tag{3.1}$$

where p_i is the probability of the i^{th} value in a time series. Logarithms are used in base 2 so information is given in bits.

Let us calculate the entropy of a system with two possibilities, for example a yes/no question. There a two possible outcomes so their respectively probabilities are p and $q = 1 - p$. Figure 3.1 illustrates the Shannon entropy as a function of p. Imagine the question is: "Is the sun going to arise tomorrow?". If we are completely certain of the outcome then $p = 1$ and the entropy is zero as no information can be extracted. However, for a different question as "Is it going to snow this Christmas?" the answer has some yes/no probability and the entropy is non zero. Furthermore if the two possible outcomes

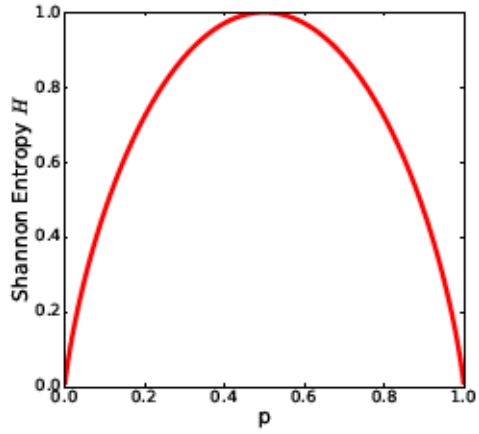

Figure 3.1: Shanon Entropy in a system with two possible outcomes p and $q = 1 - p$.

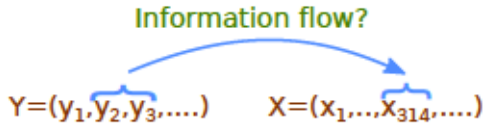

Figure 3.2: Can the previous values in Y be used to determine future values in X.

have the same probability then the entropy is maximum showing a maximum uncertainty.

Here we apply the concept of entropy to time signals of the form $X = (x_1, x_2, \ldots)$. These signals will be the data obtained from the detectors (in a experiment) or from the results of numerical simulations. For example the signal could be the temporal values of the electrostatic potential of the plasma at the edge. To calculate the entropy of one of these signals is relatively simply, first a probability distribution function (pdf) is generated from the signal then the Eq. 3.1 is applied.

The aim of this chapter is to describe a technique (the Transfer Entropy) which measures the information contained in different signals and quantifies an information flow. The idea is: can the information contained in previous values of signal Y be used to *predict* future values in X? (see Fig. 3.2)

The first approach to this issue is the *Mutual Information* which

is defined as [84]

$$I(X;Y) = \sum p(x_i, y_i) \log_2 \frac{p(x_i, y_i)}{p(x_i)\, p(y_i)} \tag{3.2}$$

where $p(x_i, y_i)$ is a joint pdf. It quantifies the amount of information shared by the two variables X and Y. Therefore if the two processes are independent $p(x_i, y_i) = p(x_i)\, p(y_i)$ so $I(X;Y) = 0$. The disadvantage of this approach is that it does not show any direction of information flow because the technique is symmetric $I(X;Y) = I(Y;X)$.

We introduce the variables

$$x_n^{(j)} = (x_{n-k}, \ldots, x_{n-k\cdot j}) \tag{3.3}$$

$$y_n^{(l)} = (y_{n-k}, \ldots, y_{n-k\cdot l}) \tag{3.4}$$

where $k, j, l \in \mathbb{N}$, they represent a vector with a set of values of size j (or l) in X and Y which take into account the preceding values. The Transfer Entropy is defined as the measurement of the information transfer from those previous events to the corresponding time series X or Y. The Transfer Entropy measuring the information flow from Y to X is

$$T_{Y\to X} = \sum p\left(x_{n+1}, x_n^{(j)}, y_n^{(l)}\right) \log_2 \frac{p\left(x_{n+1} | x_n^{(j)}, y_n^{(l)}\right)}{p\left(x_{n+1} | x_n^{(j)}\right)}. \tag{3.5}$$

The pdfs of the form $p(a|b)$ are conditional probabilities of a under the condition of b, this way the conditional pdfs in the TE are considering the previous values not only in the same X but also in Y. The summation is indicating a sum over the corresponding bins of the pdfs (for a detailed explanation see Appendix B). If Y is independent of signal X then $p\left(x_{n+1} | x_n^{(j)}, y_n^{(l)}\right) = p\left(x_{n+1} | x_n^{(j)}\right)$ so $T_{Y\to X} = 0$.

The use of the vectors $x_n^{(j)}$ and $y_n^{(l)}$ in the Transfer Entropy definition allows to analyze the TE in different time scales. However, for simplicity, in all this work we keep $j = l = 1$ so the vectors become scalars

$$x_n^{(j)} = x_{n-k} \tag{3.6}$$

$$y_n^{(l)} = y_{n-k} \tag{3.7}$$

and k turns into a *time lag*. Therefore the Transfer Entropy can be rewritten as

$$T_{Y\to X}(k) = \sum p(x_{n+1}, x_{n-k}, y_{n-k}) \log_2 \frac{p(x_{n+1}|x_{n-k}, y_{n-k})}{p(x_{n+1}|x_{n-k})}. \quad (3.8)$$

The conditional probabilities can be rewritten knowing that $p(a|b) = p(a,b)/p(b)$ so the Transfer Entropy becomes

$$T_{Y\to X}(k) = \sum p(x_{n+1}, x_{n-k}, y_{n-k}) \log_2 \frac{p(x_{n+1}, x_{n-k}, y_{n-k})\, p(x_{n-k})}{p(x_{n-k}, y_{n-k})\, p(x_{n+1}, x_{n-k})}. \quad (3.9)$$

Therefore the TE is calculated through these four pdfs. The probability distributions must be calculated using a discrete system of m bins in each dimension. For example $p(x_{n-k})$ has only m bins but for $p(x_{n+1}, x_{n-k}, y_{n-k})$ the number of bins is m^3. To have statistical significance the number of bins should be kept small compared to the to total amount of data [69]. In our numerical simulations the available time series generated will be lower than 10^3 so it implies that the m should be as well small (it is called *coarse graining* in the literature). We choose $m = 3$ in all this work unless it is explicitly written. The maximum value for the Transfer entropy is $\log_2 m$.

Notice that one of the advantage of this technique is that is directional so, in general, $T_{Y\to X} \neq T_{X\to Y}$. This way the Transfer Entropy identifies the direction of the information flow between two processes. In addition the TE can identify non-linear interaction which can be not detected by traditional methods.

3.2 Application of the Transfer Entropy

The Transfer Entropy is a quite new technique and not a large amount of information is available. Therefore, in the next subsections we provide some examples on how the Transfer Entropy is applied.

3.2.1 Analytical example

Mos of the time the TE is implemented computationally due the large number of calculations. However, here we apply this technique to an easy possible case where the problem can be solved by hand.

Imagine a person sends a sequence of signals $\{x_i\}$ generated randomly with values 1 and 0. A second person, when receives the signals $\{x_i\}$, responds, with a time delay of 1 with a sequence of signals $\{y_i\}$. So:

$$y_{i+1} = x_i$$

In this case both sequences have only two values 1 and 0. Then, choosing $m = 2$, one can trivially calculate the main PDFs for the calculation of TE. We will calculate one "time lag" which means taking $k = 0$. The probability distribution of the first signal is

$$p(x_n) \to p(0) = 0.5 \quad p(1) = 0.5$$

The joint PDFs are

$$\begin{aligned}
p(x_n, y_n) &\to p(0,0) = 0.25 \quad p(1,0) = 0.25 \quad p(0,1) = 0.25 \quad p(1,1) = 0.25 \\
p(x_{n+1}, x_n) &\to p(0,0) = 0.25 \quad p(1,0) = 0.25 \quad p(0,1) = 0.25 \quad p(1,1) = 0.25 \\
p(y_{n+1}, y_n) &\to p(0,0) = 0.25 \quad p(1,0) = 0.25 \quad p(0,1) = 0.25 \quad p(1,1) = 0.25
\end{aligned}$$

and

$$\begin{aligned}
p(x_{n+1}, x_n, y_n) \to & p(0,0,0) = 0.125 \quad p(0,0,1) = 0.125 \quad p(0,1,0) = 0.125 \\
& p(0,1,1) = 0.125 \quad p(1,0,0) = 0.125 \quad p(1,0,1) = 0.125 \\
& p(1,1,0) = 0.125 \quad p(1,1,1) = 0.125
\end{aligned}$$

$$\begin{aligned}
p(y_{n+1}, x_n, y_n) \to & p(0,0,0) = 0.25 \quad p(0,0,1) = 0.25 \quad p(0,1,0) = 0 \\
& p(0,1,1) = 0 \quad p(1,0,0) = 0 \quad p(1,0,1) = 0 \\
& p(1,1,0) = 0.25 \quad p(1,1,1) = 0.25
\end{aligned}$$

Then the transfer entropy (from $\{y_i\}$ to $\{x_i\}$) using Eq. 3.9 is

$$T_{Y\to X} = p(0,0,0)\log_2\frac{p(0,0,0)\,p(0)}{p(0,0)\,p(0,0)} + p(0,0,1)\log_2\frac{p(0,0,1)\,p(0)}{p(0,1)\,p(0,0)} +$$
$$p(0,1,0)\log_2\frac{p(0,1,0)\,p(1)}{p(1,0)\,p(0,1)} + p(0,1,1)\log_2\frac{p(0,1,1)\,p(1)}{p(1,1)\,p(0,1)} +$$
$$p(1,0,0)\log_2\frac{p(1,0,0)\,p(0)}{p(0,0)\,p(1,0)} + p(1,0,1)\log_2\frac{p(1,0,1)\,p(0)}{p(0,1)\,p(1,0)} +$$
$$p(1,1,0)\log_2\frac{p(1,1,0)\,p(1)}{p(1,0)\,p(1,1)} + p(1,1,1)\log_2\frac{p(1,1,1)\,p(1)}{p(1,1)\,p(1,1)}.$$

Substitute the terms by the values already calculated. All the terms are equal so

$$T_{Y\to X} = 8\cdot\frac{1}{8}\log_2\frac{1/8\cdot 1/2}{1/4\cdot 1/4} = 0$$

which was the expected result since there is no information flow from $\{y_i\}$ to $\{x_i\}$. Similarly we calculate the information flow in the other direction. In that case not all the terms will be equal so

$$T_{X\to Y} = 4\cdot\frac{1}{4}\log_2\frac{1/4\cdot 1/2}{1/4\cdot 1/4} + 4\cdot 0 = 1$$

which is the obvious solution since $y_{i+1} = x_i$

3.2.2 Two simple signals

This example is more complex than the previous one but it explains the basic features of Transfer Entropy. We apply the Transfer Entropy method to two simple signals. The upper panel on Fig. 3.3 shows those signals. The signal X (solid line) is composed by two Gaussian functions ("A" and "C") and signal Y (dashed line) by one Gaussian ("B") but at an intermediate time. In the lower panel, the Transfer entropy results are plotted for both directions. First, we focus on the $T_{X\to Y}$. The TE shows at time lag 300 a peak. That time is not arbitrary but it is the time between the peaks "A" and "B" in signal X and Y. The TE peak is showing that the signal Y can be predicted by the information in the signal X with a time delay 300. Basically, it is the effect of "A" on "B". "C" in signal X has no impact in the TE (in this case) because it happens after "B" in signal Y.

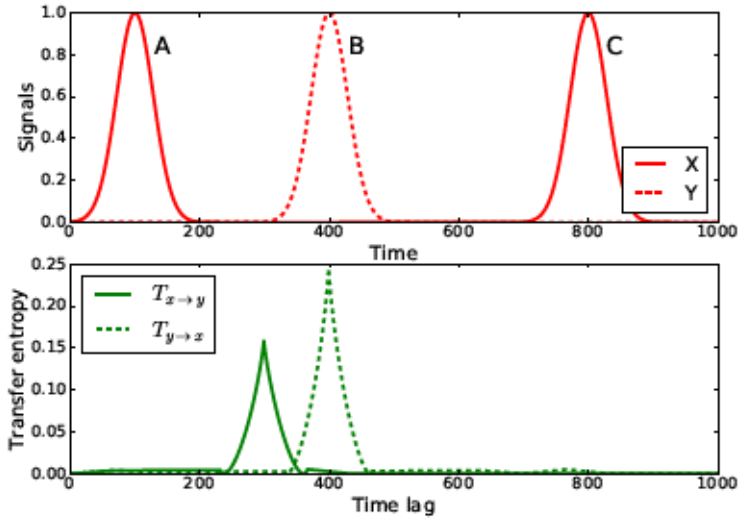

Figure 3.3: Transfer entropy results (lower plot) obtained by the signals in the upper plot.

Now, we interpret the $T_{Y\to X}$. We observe a peak in the transfer entropy at a time lag 400. That time is the delay between "B" and "C". The TE is indicating that "C" could be predicted by "B" which occurred a time 400 before. It is showing the effect of "B" on "C".

Therefore, $T_{X\to Y}$ is showing the flow information from "A" to "B" and $T_{Y\to X}$ the flow information from "B" to "C".

One should notice that the Transfer entropy in both directions have different size. The reason is that for $T_{Y\to X}$ most of the information in signal Y ("B") is flowing to signal X ("C") . However, for $T_{X\to Y}$ only *half* of the information of X ("A") is flowing to signal Y.

We should mention that a signal with higher or lower amplitude has no effect in the Transfer Entropy. That feature (which is not shown in the example) can be important once we use the technique. That allows us to identify the flow of information (and causality) between two signals even if one of them is smaller than the other.

3.2.3 Predator-prey model

The predator-prey model is a pair of coupled non-linear differential equations which have been used, with variations, in biological systems to study the interaction between two different species (one acting as a

prey, the other as a predator). Here we use the known Lotka-Volterra model [85, 86]. Let us call x the number of preys (rabbits) and y the number of predators (foxes), then the Lotka-Volterra equations are

$$\frac{dx}{dt} = \alpha x - \beta xy$$
$$\frac{dy}{dt} = \delta xy - \gamma y$$

where $\alpha, \beta, \gamma, \delta$ are the parameters that describe the interactions. The term αx describes the natural growth of rabbits. The negative term βxy correspond to the decrease of population due to hunting. Similarly the effect is positive in the population of foxes with δxy. Finally the natural death of foxes is illustrated by γy.

The dynamics of the system is quite intuitive. Starting from a high rabbit population and low number of foxes, it makes increase the number of foxes due to available food. As there are more foxes the rabbit population decreases. Due to the lack of preys, foxes die. The decrease of foxes generates the increase in rabbit population. And then the cycle repeats again with these 4 steps. That dynamics will produce a periodicity in both populations. The increase or decrease of populations depends on the parameters of the system but in general the functions are not symmetric. The upper plot in Fig. 3.4 illustrates that dynamics for the parameters $\alpha = \beta = \gamma = \delta = 1$, units of the signals are arbitrary. The mentioned periodicity can be observed in signals.

The Transfer Entropy will be applied to the signal but this time it is going to be compared with the results of the cross-correlation. The cross-correlation (CC) is a technique which measures the similarity between two signals f and g and is defined as

$$f \star g = \int_{-\infty}^{\infty} f^*(t)\, g(t+\tau)\, dt \tag{3.10}$$

where τ is the time lag and the f^* indicates the complex conjugate of f.

The CC is applied to results of the predator-prey model, the results are shown in the middle panel in Fig. 3.4. The function shows maximums (in absolute value) of correlation at some time lags (positive

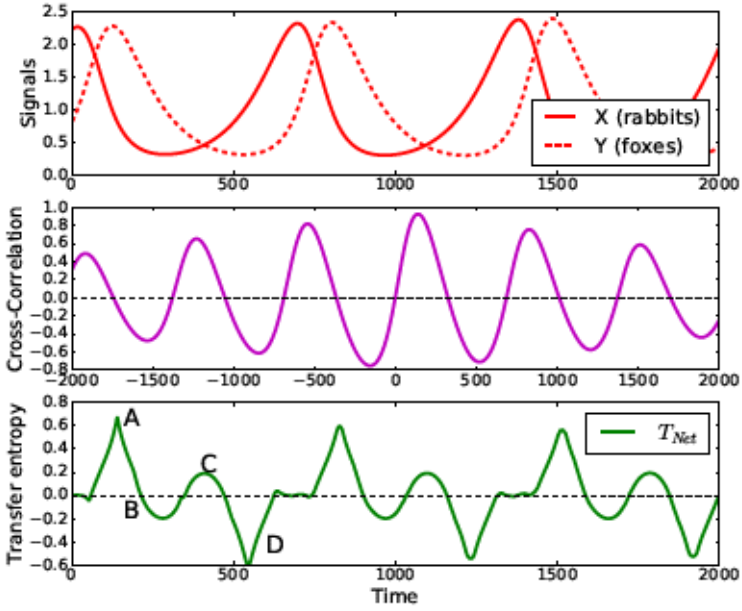

Figure 3.4: Predator-prey model. The upper plot shows the time evolution of both populations. Middle and lower plots show the results of the cross-correlation and Transfer Entropy respectively.

and negative). The time lag in Eq. 3.10 is shifting one of the functions respect the other one, so the maximums we observe on the figure are indicating when the two functions are approximately superposed (or the opposite). The cross-correlation shows a periodicity similar to the original signals. However, the CC technique does not provide any more information about the system.

On the other hand, the lower plot in Fig. 3.4 shows the net transfer entropy which is defined as $T_{\text{Net}} = T_{X\to Y} - T_{Y\to X}$. It is an interesting measurement where we can see the net amount of information flowing and, more importantly, their direction. In our example the T_{Net} has the same periodicity of the predator-prey signals (about 600 time steps). In each periodicity we can observe four regions indicated by letters A, B, C and D. The region A is indicating an information flow from X to Y, it illustrates the effect that a high number of rabbits (X) makes increase the amount of foxes. On B the information flow is flowing in the opposite direction, as the number of foxes (Y) is high then the rabbit population decreases (X). C region illustrates the fact that that decrease of rabbits (X) produces a decrease in fox population (Y). Finally the cycle is closed in D where the lack of predators (Y) generates an increase in rabbit population (X).

In conclusion, the net transfer entropy has detected the 4 different steps in the model. Furthermore, it is capable to indicate the causality of those steps showing the correct information flow in the coupled system.

Chapter 4

Heat propagation in TJ-II

One of the main challenges in magnetically confined fusion plasmas is to understand transport. Heat transport plays an important role in the confinement time and it is crucial for a viable future nuclear reactor. For decades, scientific community has proposed different approaches to understand and describe this transport.

One of the most used tools to study heat transport, in experiments or numerical simulations, are the perturbative methods. They involve the insertion of a small perturbation in the plasma and then its response is studied.

In this chapter, we propose an approach to study heat transport based on perturbative methods. A TJ-II plasma is simulated using the resistive MHD model described in Sec. 2.3.5. Instabilities in the model are driven by pressure gradients, in this case, resistive interchange modes. Once the plasma is in steady state, a heat perturbation is set and then its evolution is analyzed.

During this chapter we study the evolution of single perturbations and how far they differ from a diffusive system. Furthermore, pulses at different radial locations evolve in a different way due the effect of the poloidal velocity. That effect is analyzed using the Transfer Entropy (TE) technique. The same study is applied to a different TJ-II magnetic configuration and similar conclusion are obtained. Finally, in the last section, experiments using the TE are discussed and compared with the numerical results.

The Transfer Entropy appears to be a useful technique to study heat transport. The technique allows to identify the propagation of heat pulse and follow its temporal evolution over the system. This

is even more powerful in fusion plasma experiments where traditional heat perturbation transport techniques (as linear correlation or conditional averaging [68]) do not offer enough clarity.

In the next sections we will observe that heat transport is affected by the radial shear of the poloidal velocity of the plasma. The poloidal flow is generated by turbulence via the Reynolds stress. The role of the turbulent fluctuations and the generation of a perpendicular flow is studied in detail in Chapter 7

The magnetic configuration is an important element in the generation of the poloidal flow. The rational numbers in the rotational transform determine the location of closed magnetic field lines. We are using an MHD model based on resistive interchange modes so instabilities are extended along the closed magnetic field lines. Therefore, turbulence intensifies in the low order rationals surfaces. As the poloidal velocity is partly described by the turbulence, the location of the main rational surfaces may have an impact in the poloidal velocity profile. Furthermore, the low magnetic shear in the TJ-II produce a low density of low-number rationals. As a consequence, it is easy to identify the impact of the rational surfaces (and the flow associated to them) on heat transport.

In most of this chapter numerical simulations will be based on the standard magnetic configuration (called 100_44) in TJ-II, however more examples will be given using a different configuration (in particular 100_46). Obviously, the two configurations have different rational surfaces so turbulence vortices may be generated at different locations and, consequently, other poloidal velocity profile will appear. Note that poloidal flow is not completely determined by the magnetic configuration, other factors as temperature and density profiles may be significant.

Part of the content in this Chapter has been published in Ref. [1]: B.Ph. van Milligen, J.H. Nicolau, L. García, B.A. Carreras and C. Hidalgo. *"The impact of rational surfaces on radial heat transport in TJ-II"*. Nucl. Fusion **57**, 056028 (2017).

4.1 Steady state plasma

The perturbative approach is going to be applied to a steady state plasma. Here we use a resistive MHD model based on interchange

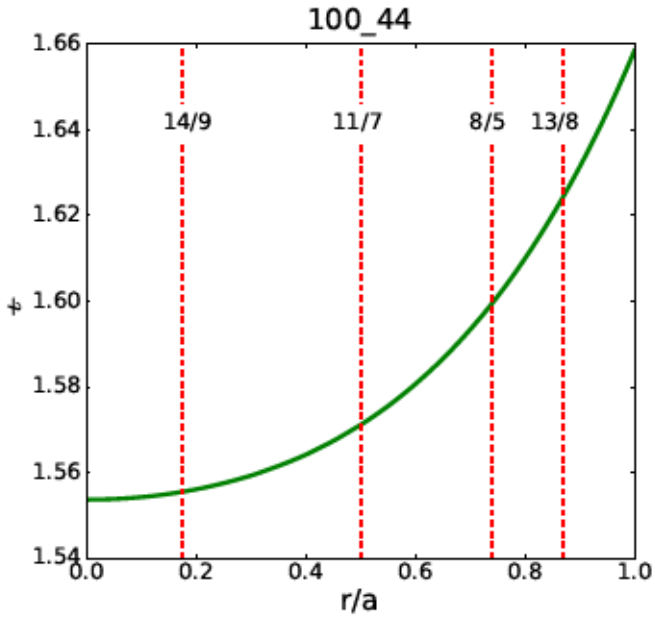

Figure 4.1: Rotational transform for the "standard" magnetic configuration 100_44 in TJ-II. Main rational surfaces are indicated with vertical lines.

modes described in Sec. 2.3.5 to reach a steady state. We use the standard magnetic configuration in TJ-II called 100_44 (see rotational transform in Fig. 4.1) where the values indicate the current through the external field coils. The initial profiles are the typical of ERCH heated plasmas in TJ-II.

The variables in the numerical code are decomposed in Fourier components where m and n are the poloidal and toroidal numbers respectively. In the present numerical calculations we introduce the resonant helicities, corresponding to the q profile, up to $m = 100$ which give a total number of angular components of 446. The value $m = 100$ is chosen because it is a value of m large enough where resistive interchange turbulence is saturated through dissipation [61].

In the simulations, $S = 2 \times 10^5$, $\beta_0 = 10^{-3}$, $\bar{\omega}_{*e} = 2 \times 10^{-4}$, $\bar{\omega}_{ci} = 500$. The diffusivity parameters used are $D_\perp = \chi_\perp = 0.1a^2/\tau_R$ and $\mu = 0.05a^2/\tau_R$. The parallel electron heat conductivity is $\chi_\parallel = 2\times10^6 a^2/\tau_R$. The diffusivities for the average temperature and density evolution are $D_{0\perp} = \chi_{0\perp} = 0.3a^2/\tau_R$. The collisional flow damping rate is $\hat{\mu} = 40\tau_R^{-1}$.

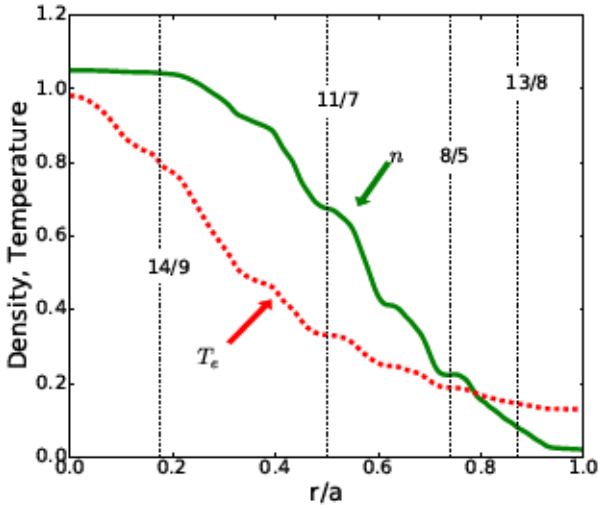

Figure 4.2: Density (solid green line) and electron temperature (dotted red line) profiles at the steady state. Main rationals surfaces are indicated by vertical dashed lines

The equations (see Sec. 2.3.5) are numerically advanced until the plasma is at steady state. Figure 4.2 shows the density and electron temperature profiles at that state. The profiles are not static but for our analysis the change is not relevant. A source term is included during the numerical simulations to keep the profiles. The solid green line and the dotted red line are the density and electron temperature profile respectively. Vertical dashed lines indicate the location of main rational surfaces. The temperature and density values are normalized to the maximum of their equilibrium profiles. For the duration of our studies the profiles can be taken as constant.

At steady state an average poloidal flow $\langle V_\theta \rangle$ is present in the plasma (brackets indicate a poloidal and toroidal average). Even though the velocity profile is not constant, it fluctuates around an equilibrium profile. Figure 4.3 is showing the temporal average poloidal flow, the time interval of the average is much longer ($\sim 0.1\tau_R$) than any of the following studies. The solid green line represents the temporal averaged poloidal flow, the other two dashed and dotted curves indicate one standard deviation from the mean value in the temporal average. It can be observed that the poloidal flow change is small for

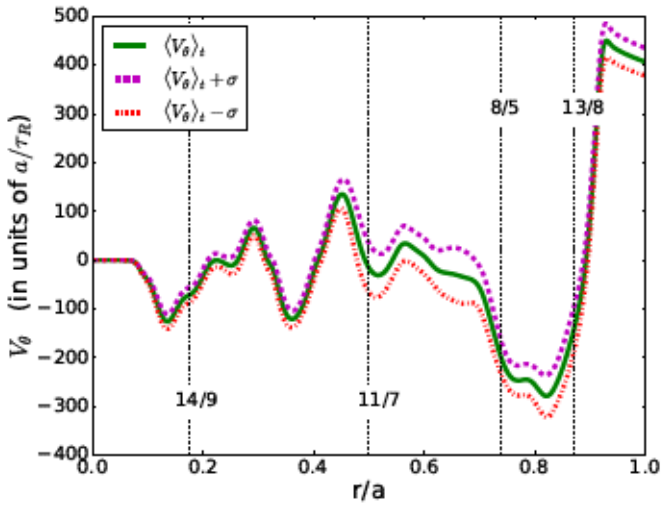

Figure 4.3: Temporal averaged poloidal velocity at steady state (solid green line). Dashed and dotted lines indicate one standard deviation from the mean value.

long times, so for the duration of the heat perturbation the flow can be taken as constant. This characteristic is important as the poloidal flow will be relevant in the heat propagation.

4.2 Single heat perturbation

In the present study we use perturbations to analyze heat transport. Therefore, a single instantaneous perturbation is set in the electron temperature profile. As any other perturbative method, these perturbations have to be large enough to allow us to study its evolution but at the same time small to not alter the plasma conditions. Hence, in all this thesis, we use perturbations with a Gaussian shape

$$\Delta T_e \cdot e^{-(r-r_0)^2/2\sigma^2} \tag{4.1}$$

where $\Delta T_e = 1.5$,the maximum is centered in r_0 and the width is $\sigma^2 = 0.005$. So the perturbation is narrow enough to focus in the transport around the initial location and the mass of the perturbation is suitable to follow the perturbation itself but is negligible for the total mass in the temperature profile.

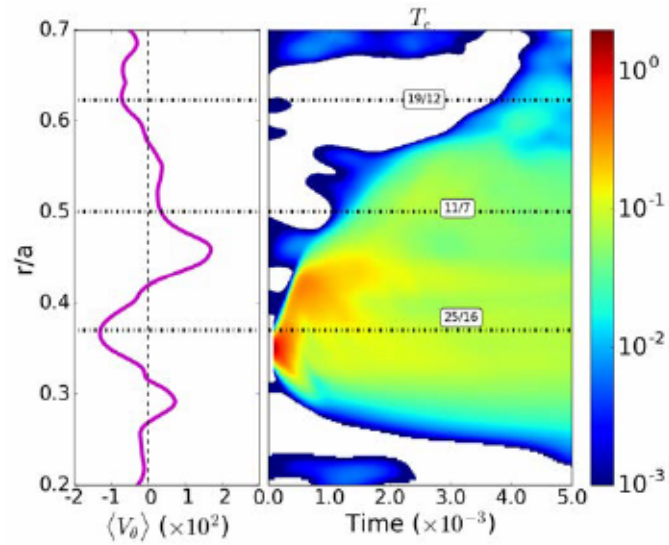

Figure 4.4: Right panel shows the temporal evolution of a heat propagation initially located $r/a = 0.35$. The left panel illustrates the average poloidal velocity before the perturbation.

As a first example we set a perturbation at the radial location $r/a = 0.35$ in the plasma at the steady state described in Sec. 4.1. The pulse is placed instantaneously so no previous heating is taken into account. The temporal evolution of this pulse is illustrated in the right panel in Fig. 4.4. For a better visualization, the initial (just before the pulse) electron temperature profile is subtracted so only the evolution of the perturbation is shown. The left panel shows the average poloidal velocity $\langle V_\theta \rangle$ at a time immediately before to the pulse introduction. Time and velocity units are normalized to τ_R and a/τ_R respectively. The heat perturbation evolves in time and it shows a radial propagation. One can observe that the propagation is not symmetrical but the outward direction is dominant. Furthermore, the time evolution shows a non continuous radial propagation, for example the propagation is faster from $r/a = 0.35$ to $r/a = 0.47$ than the propagation from $r/a > 0.47$. So the perturbation seems to be slowed down and most of the pulse is partly *trapped* around $r/a \approx 0.45$ as it is visible in a red color in the figure.

We suggest that the reason of the slow down of the perturbation seems to be the poloidal flow in the plasma. In this example the perturbation is trapped around $r/a \approx 0.45$ and it is in this radial

region where the radial shear of the poloidal flow $d\langle V_\theta \rangle / dr$ is strong. Furthermore at $r/a \approx 0.48$ the perturbation is slowed down and again, a strong radial shear in the poloidal flow is present. More examples will be given in the next sections to support this idea: the average poloidal flow may be the cause of the slow down in heat perturbations.

4.3 Diffusive model

In this section we compare the results from the heat perturbation in the MHD model from Sec. 4.2 with the results from a diffusive model. Here we show that the transport we observe cannot be described in a diffusive way. For a quantitative analysis of transport see Chapter 6 where transport is characterized using effective diffusivities.

The first attempt to study transport is to compare it with a diffusive model. It is a broadly known description of many physical systems and an analytical solution can be obtained. In one dimension the model is described by the equation

$$\frac{\partial T_e}{\partial t} = D\frac{\partial^2 T_e}{\partial^2 r} \tag{4.2}$$

where D is the constant diffusion term. That simple equation can describe easily the (diffusive) transport which rely on the D parameter. Depending on the D value, it will imply a faster or slower transport.

Here we simulate a system governed by Eq. 4.2. The numerical value of D is chosen to reproduce a diffusive propagation at similar time scales as the MHD model. The aim is to compare qualitatively the propagation in the two different systems. To mimic the MHD results, the same temperature profile is used and the system is evolved until the profile becomes smooth. A small source is added to keep the profile and, once the profile is in a steady state, a perturbation is introduced. The heat perturbation has the same characteristics as before and is located at the same radius $r/a = 0.35$. Figure 4.5 illustrates the time evolution of a perturbation in our MHD model (solid green line) and the 1D diffusive system (dashed black line). From left to right the panels are showing different time steps $t_1, t_2 \ldots t_8$. Clearly the perturbation in the plasma does not behave in a diffusive manner. The propagation is not symmetrical and it seems to slow down at some radius. On the other hand, in the diffusive system, the perturbation smoothly broadens and the peak keeps in the same radial point.

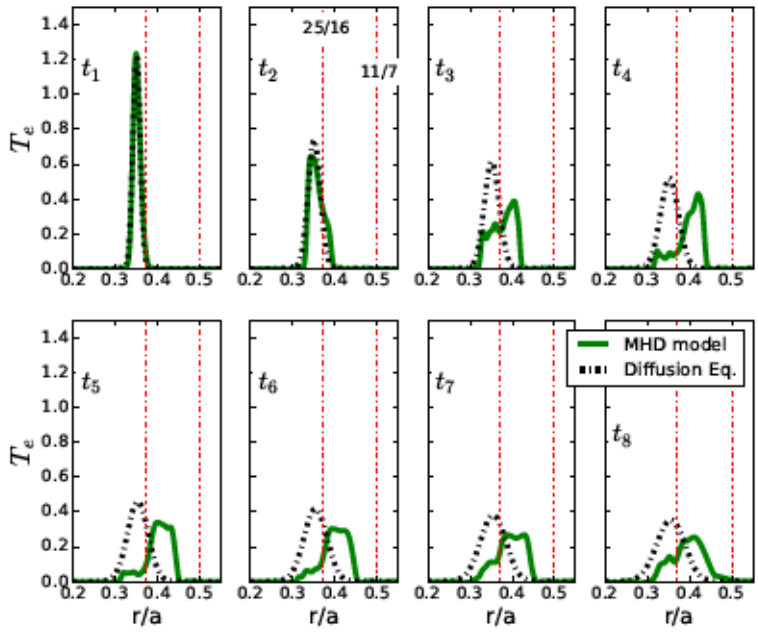

Figure 4.5: The different panels show the temporal evolution of the same heat perturbation for the MHD model (solid green line) and using the diffusion equation (dashed black line).

Therefore, as the heat propagation in fusion plasmas is not diffusive we try to analyze it and describe some of its characteristics in the next sections.

4.4 Heat perturbations at different locations

In Sec. 4.2 the time evolution of a heat perturbation in our model was shown. The radial propagation was observed to be non-diffusive and, at certain radial locations, the propagation was changing. It would be interesting to study the radial heat propagation along the plasma. However, one single perturbation only allows to analyze transport in the surrounding areas because for longer times the perturbation is too weak. Therefore, to study heat transport we set pulses at different locations and then extract their temporal evolution.

We set heat perturbations at different radial locations. To avoid interaction between perturbations, each pulse is run in a different numerical simulation but all of them are starting from the same initial steady state plasma. Figure 4.6 shows in the five right panels the temporal evolution of five perturbations initially located at $r/a = 0.2$, $r/a = 0.25$, $r/a = 0.35$, $r/a = 0.45$ and $r/a = 0.55$ respectively. The left panel illustrates the average poloidal flow at a time before the introduction of the heat perturbations.

One can observe in Fig. 4.6 that all the perturbations show different radial propagation. The inner perturbations seem to propagate slower than the ones located at outer regions which is consistent with experimental results in other devices [51]. Furthermore, in all of them the radial propagation is changing as the pulse is propagating and at certain radial locations the perturbation seems to slow down.

We suggest that the reason of the slow down of the perturbations is the presence of a radial shear of the poloidal flow $d\langle V_\theta \rangle / dr$. The pulse at $r/a = 0.20$ propagates radially outward until it is slowed down around $r/a \approx 0.28$ because in the radial region $r/a \approx 0.30$ there is a strong shear. The second pulse ($r/a = 0.25$) is mostly trapped in its initial position because of the same shear region as before. The perturbation initially located at $r/a = 0.35$ is partially trapped around $r/a \approx 0.40$ where another strong shear region is present. However the pulse still propagates until it reaches $r/a \approx 0.58$ where it is slowed

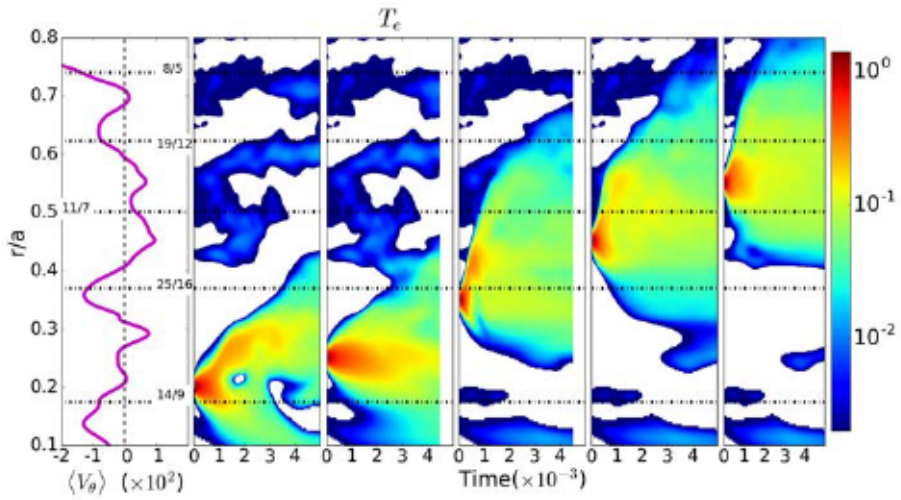

Figure 4.6: Left panel indicates the average poloidal flow before the perturbations. The five right panels show the temporal evolution of a heat perturbation at $r/a = 0.2$, $r/a = 0.25$, $r/a = 0.35$, $r/a = 0.45$ and $r/a = 0.55$.

down because the strong shear. The fourth pulse ($r/a = 0.45$) shows as well radial propagation but it is as well slowed down around $r/a \approx 0.58$. Finally the last perturbation at $r/a = 0.55$ seems to be partially trapped in its initial location (see red color in the figure) although it shows also outward radial propagation.

Therefore in all the different cases the radial shear of the flow has affected the heat propagation. As in some radial positions the pulse is slowed down or partially trapped, we suggest the presence of (mini) transport barriers. In Chapter 7 we focus on the poloidal flow generation and its involvement in the transport barriers.

4.5 Transfer entropy

In numerical simulations is relatively easy to identify heat perturbations, for example in the last sections we could qualitatively analyze their temporal evolution. However in fusion experiments that can be a laborious task because for instance, most perturbative methods use a modulated signal instead of a single perturbation [87] or signals can be very noisy due to the background plasma. Therefore a statistical

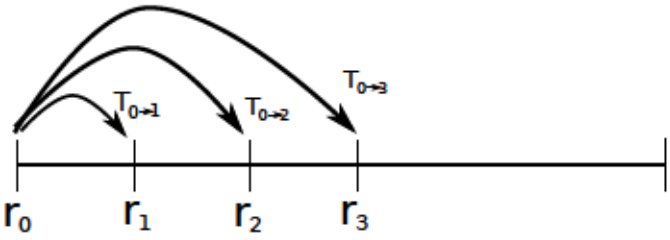

Figure 4.7: Schematic of the calculation of Transfer Entropy for heat transport.

analysis of the signals obtained by detectors becomes crucial.

Some of the traditional methods for signal analysis are for example the linear correlation or conditional averaging. Here we use the Transfer Entropy (TE) technique which was described in detail in Chapter 3. The TE measures the information in the different signals and quantify an information flow between them. So having two signals, the technique quantifies if the previous information contained in one signal can be used to predict the other signal. The TE has demonstrated to be a robust technique compared with other correlation techniques.

For convenience the Transfer Entropy (Eq. 3.9) is rewritten here

$$T_{Y\to X}(k) = \sum p(x_{n+1}, x_{n-k}, y_{n-k}) \log_2 \frac{p(x_{n+1}|x_{n-k}, y_{n-k})}{p(x_{n+1}|x_{n-k})}. \quad (4.3)$$

The TE is applied to the results from previous sections in the following way. In the numerical simulations (and in the experiments) the electron temperature is measured during some time at different radial locations. From each of these locations a time signal of the temperature is obtained. We set as the reference signal the one located at the initial location of the heat perturbation, then we apply the TE from that reference signal (Y in Eq. 4.3) to all the other signals. So, in other words, if we have signals at different radius $r_0, r_1, r_2 \ldots$ the TE is calculated as $T_{0\to1}, T_{0\to2}, T_{0\to3} \ldots$ (see the schematic in Fig. 4.7). Therefore for each radial location we obtain a TE function which is the result of applying Eq. 4.3 from the reference signal Y to the temperature signal X measured in the particular radial location. All these TE functions (one TE function for each radius) can be gathered in the same way as, for example, the right panel in Fig. 4.4.

The TE is applied to the numerical results from the time evolution of the heat perturbation described in Sec. 4.2. In this case the reference

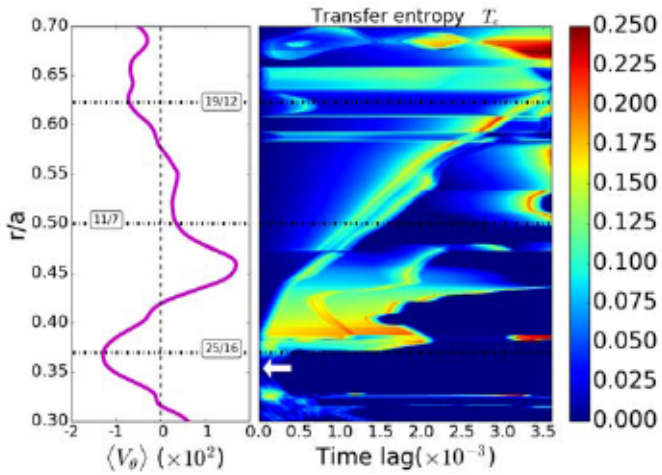

Figure 4.8: Right panel shows the Transfer Entropy result for a perturbation initially located (white arrow) at $r/a = 0.35$ (Fig. 4.4). The left panel illustrates the average poloidal velocity before the perturbation.

signal will be located at the same place as the initial location of the perturbation, $r/a = 0.35$. All the TE functions obtained for each radial location are gathered and plotted in the right panel in Fig.4.8. The white arrow indicates the radial location of the reference signal Y (and the initial location of the perturbation) and the left panel is showing again the average poloidal velocity before the perturbation.

Notice that Fig. 4.8 is showing information flow and not temperature. So, what are we seeing? For example, the high TE area at $r/a \approx 0.55$ and time lag 2×10^{-3} is actually telling that what happened at $r/a = 0.35$ (reference signal) is affecting at $r/a \approx 0.55$ after a time lag 2×10^{-3}. In spite of the fact that we are observing information, the TE is reproducing the radial propagation of the perturbation as we observed in Fig. 4.4. The information is flowing radially outward and the *trapping* region around $r/a \approx 0.40$ is also observed.

The Transfer Entropy results from heat perturbations, as in Fig. 4.8 may be a bit noisy so to avoid this issue we proceed as follows. We simulate 8 heat perturbations at the same radial location but using a different plasma background (we launch the perturbation at different times in the steady state). The eight simulations are run independently and equivalent results are obtained because the plasma profiles are reasonably similar as we noticed in Sec. 4.1. Then the TE is ap-

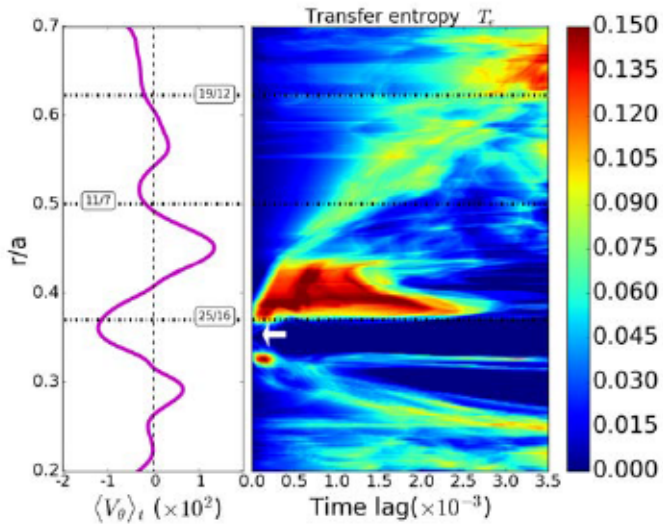

Figure 4.9: Right panel shows the average Transfer Entropy result for eight perturbations located at $r/a = 0.35$ (as in Fig. 4.8). The left panel illustrates the temporal averaged poloidal velocity during the steady state.

plied to these numerical results and the eight cases are averaged. As a consequence the TE results are much clearer as it can be seen in Fig. 4.9. The radial outward propagation is visible and the high TE area around $r/a \approx 0.4$ shows as well the trapping region.

Now, as it was done in Sec. 4.4, the heat transport is analyzed at different radial locations but this time using the Transfer Entropy. We apply the TE to the numerical data from heat perturbations located at different radial regions. All the cases are independent simulations so there is no interaction between perturbations.

Figure 4.10 shows in the five right panels the Transfer Entroppy results for heat perturbations initially located (white arrow) at $r/a = 0.20$, $r/a = 0.25$, $r/a = 0.35$, $r/a = 0.45$ and $r/a = 0.55$ respectively. The left panel is the temporal averaged poloidal velocity. For a better visualization, the TE is normalized in each panel to its maximum, in particular the maximum values are 0.3, 0.25, 0.15, 0.25, and 0.15. In all cases the information flow is showing a similar propagation to the one exhibited by the temperature data (see Fig. 4.6).

A radial outward propagation is observed in all perturbations in Fig. 4.10 and it seems that radial transport is faster in the outer loca-

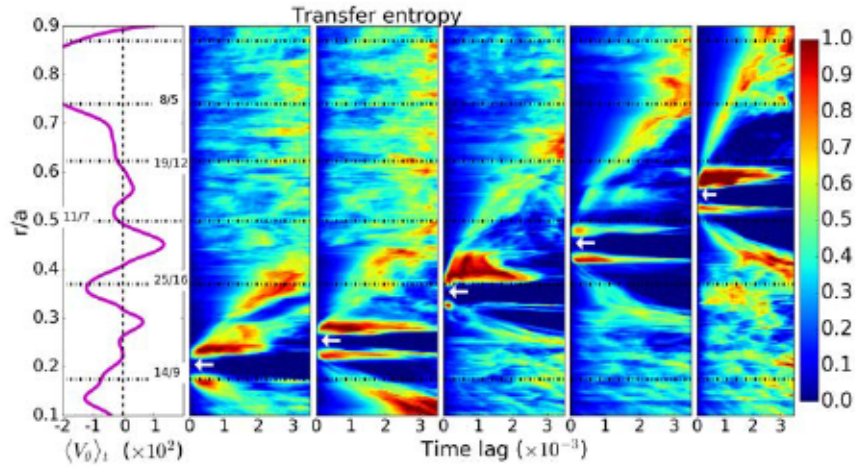

Figure 4.10: Left panel shows the temporal averaged poloidal velocity. The right five panels show the heat evolution, using the Transfer Entropy, of five perturbations at different radial locations.

tions. Again we observe trapping regions which are characterized by a high TE horizontally extended. As we suggested before (Sec.4.4) the trapping regions should be related to the presence of mini transport barriers. These barriers, as we analyze in Chapter 7, may be due to the radial shear in the poloidal flow. The heat perturbations are trapped or slowed down around these areas and the Transfer Entropy can identify these regions. For example, a trapping regions is observed around $r/a \approx 0.28$ in the second and third panel. Another region where the perturbations seem to slow down is around $r/a \approx 0.38$, visible in the second, third and fourth panels. In $r/a \approx 0.6$ another transport barrier is seen in the sixth panel. All these trapping areas are located next to (or into) a radial shear region.

4.6 Cross-correlation

One of the goals of this chapter, and this thesis, is to show that the Transfer Entropy is a viable technique to study heat transport in Fusion plasmas. Therefore we should compare it with other approaches. In this section we apply the cross-correlation (CC) technique to our numerical simulations and compare it with the TE results.

The cross-correlation is a technique which indicates the similarity

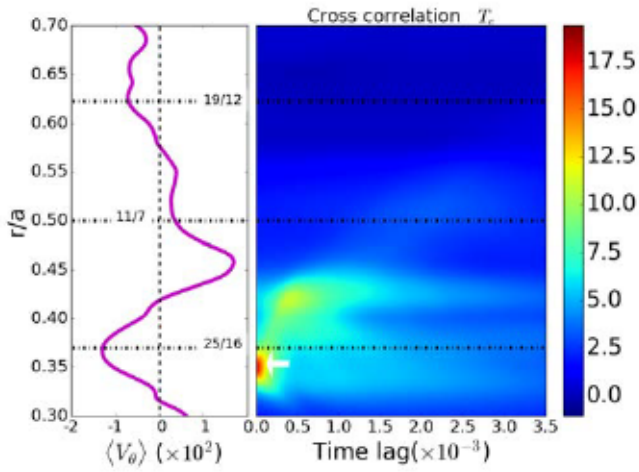

Figure 4.11: Left panel shows the averaged poloidal velocity. The right panel shows the Cross correlation results for a heat perturbation in $r/a = 0.35$ (white arrow).

between two functions (f and g). So basically it compares two time signals and can detect similar "events" in previous times. The cross-correlation function is defined as

$$f \star g = \int_{-\infty}^{\infty} f^*(t)\, g(t+\tau)\, dt \tag{4.4}$$

where f^* indicates the complex conjugate of function f and τ is the time lag.

Here we apply the cross-correlation to the numerical data obtained for the heat perturbation initially located in $r/a = 0.35$ (see Sec. 4.4). As in the TE example, the CC is applied from a reference signal to all the other signals at each available radial location. Figure 4.11 shows in the right panel the cross-correlation results. We can observe a high CC area around $r/a \approx 0.40$ which is a similar result to the TE in Fig. 4.9. It corresponds to a trapping region. However no much more information can be extracted from Fig. 4.11, the radial propagation is not clear and only is visible in a short radial region. Therefore the Transfer Entropy is more suitable for the study of heat transport. In experiments, where is more difficult to identify perturbations, the Transfer Entropy can be even more useful.

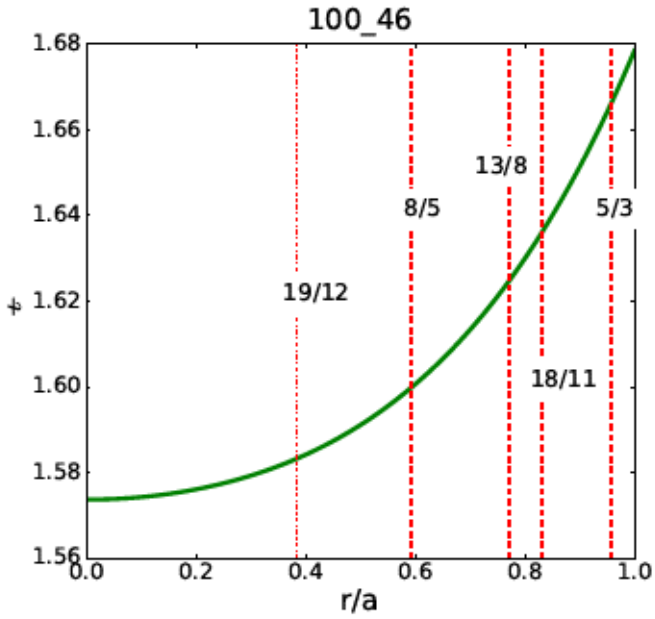

Figure 4.12: Rotational transform for the magnetic configuration 100_46 in TJ-II. Main rational surfaces are indicated with vertical lines.

4.7 Magnetic configuration 100_46

All the previous results in this chapter correspond to a TJ-II plasma using the *standard* magnetic configuration called 100_44. The numerical results suggested that the average poloidal flow generated in the plasma was affecting the heat transport. Since the flow is partly determined by the position of rational surfaces (see Chapter 7), it is going to be interesting to perform the same analysis but under a different magnetic configuration.

In the TJ-II device the current in the different coils determine the magnetic configuration so the location of main rational surfaces can be modified through that current. In this section we study the heat transport in a plasma under the magnetic configuration 100_46 (see rotational transform in Fig. 4.12). In these configuration we have most of the low order rationals from the standard configuration but their locations have been displaced. For example the 8/5 is located in an inner radial position and the 5/3 appears at the edge. Therefore, having a different configuration will allow a different poloidal flow

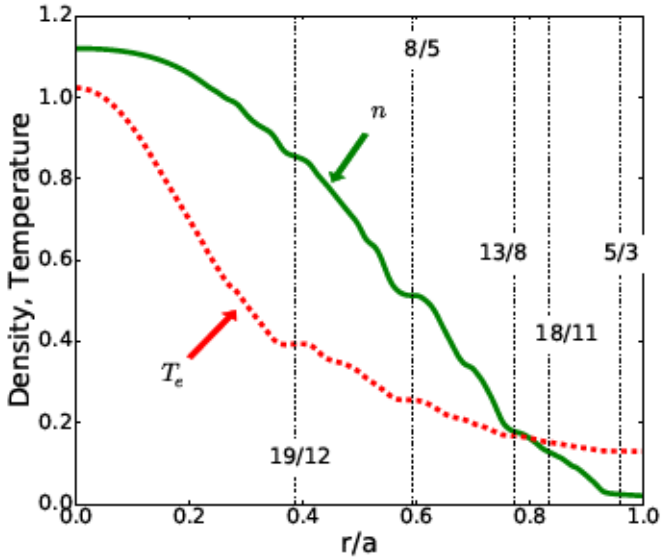

Figure 4.13: Density (solid green line) and electron temperature (dotted red line) profiles at the steady state in the 100_46 magnetic configuration. Main rationals surfaces are indicated by vertical dashed lines.

profile.

4.7.1 Steady state plasma

Before starting with the analysis of heat transport we need a steady state plasma. The plasma is modeled using the same resistive MHD model (described in Sec. 2.3.5) which main instabilities are the interchange modes. Obviously, this time the plasma is simulated using the magnetic configuration 100_46. The parameters used in the simulations are the same as 100_44.

Again, as the variables are decomposed in Fourier components, we use in the numerical simulations only the resonant helicities corresponding to the q profile up to $m = 100$. These condition implies that 528 angular components are used.

Model equations (Sec. 2.3.5) are numerically advanced and after a transient time the plasma reaches a steady state. The electron temperature and density profiles at the steady state are shown in Fig. 4.13. The vertical lines are indicating the position of the new rational sur-

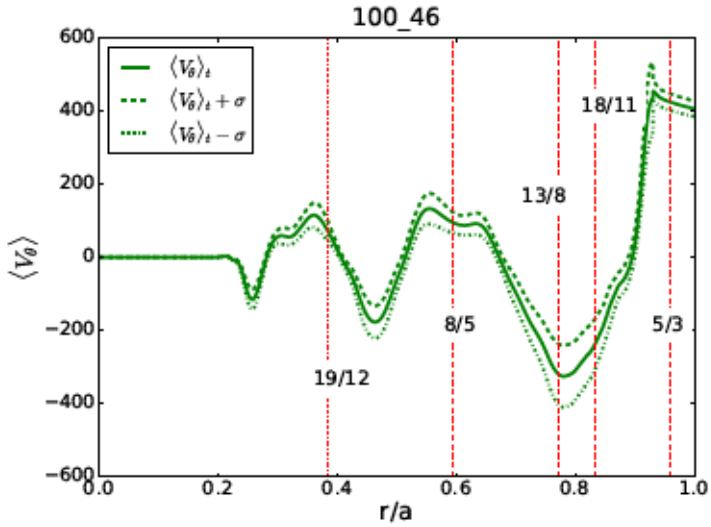

Figure 4.14: Temporal averaged poloidal velocity at steady state(solid green line) fro the 100_46 magnetic configuration. Dashed and dotted lines indicate one standard deviation from the mean value.

faces. Note that the temperature and density profiles are not static and they are evolving in time. Although a source term is added to keep the profiles stable during the steady state, the profiles are not constant and can change. However for our analysis the profiles can be taken mostly constant.

At the steady state a poloidal flow is present in the plasma. Figure 4.14 shows in solid line the temporal averaged poloidal flow. The temporal range of the the average is much longer than any of our studies ($\sim 0.05 t_R$). The dashed and dotted lines represent one (positive and negative) standard deviation from the average. One can observe that there is no much variation of the poloidal flow, it oscillates around an "equilibrium" value. Therefore during our simulations the poloidal velocity is taken almost constant.

4.7.2 Heat perturbations

Heat transport in a 100_46 TJ-II plasma is analyzed following the same approach as previous sections. Once the plasma is in the steady state, a heat perturbation is set at some radial location and its temporal evolution is studied. The propagation of the heat pulse is examined

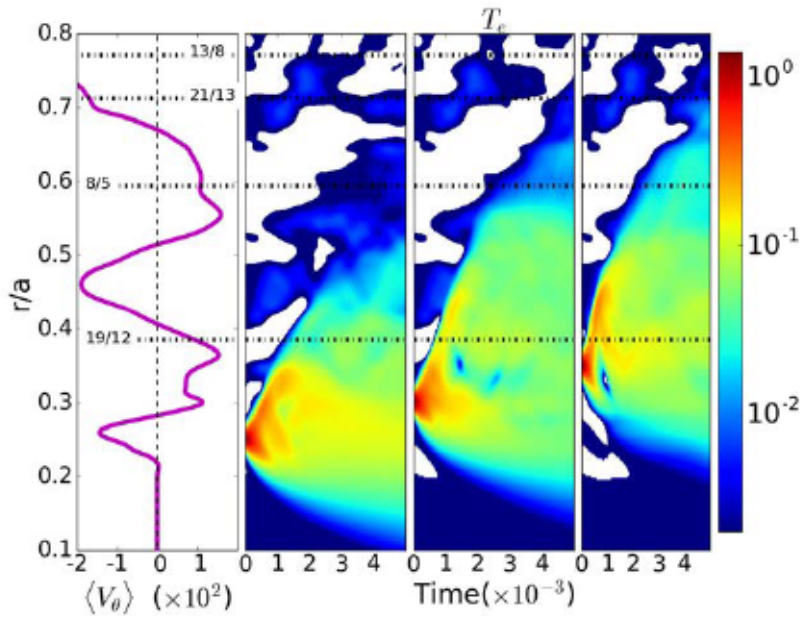

Figure 4.15: Left panel indicates the averaged poloidal flow before the perturbations. The five right panels show the temporal evolution of a heat perturbation at $r/a = 0.25$, $r/a = 0.30$ and $r/a = 0.35$.

first observing the propagation of temperature of the perturbation itself and then using the Transfer Entropy.

We are going to set heat perturbations at certain locations as we did in Sec. 4.2. Note that the perturbations have to be small enough to keep the plasma "stable". Here three heat perturbations are launched at three radial locations with the same steady state plasma but in independent simulations. Figure 4.15 shows in the three right hand side panels the temporal evolution of the heat perturbations initially located at $r/a = 0.25$, $r/a = 0.30$ and $r/a = 0.35$ respectively. The left panel shows the average poloidal velocity just before the perturbation.

The three perturbations in Fig. 4.15 are exhibiting a radial outward propagation but not at the same rate in each case. There are radial regions where the perturbations seem to be slowed down or trapped. For a better analysis we will use the Transfer Entropy.

The Transfer Entropy is applied to the numerical results in the same way as it was done in Sec. 4.5. The TE is calculated from a reference temperature signal in the initial radial location of the pulse to signals at different radius. The TE results are averaged over 6

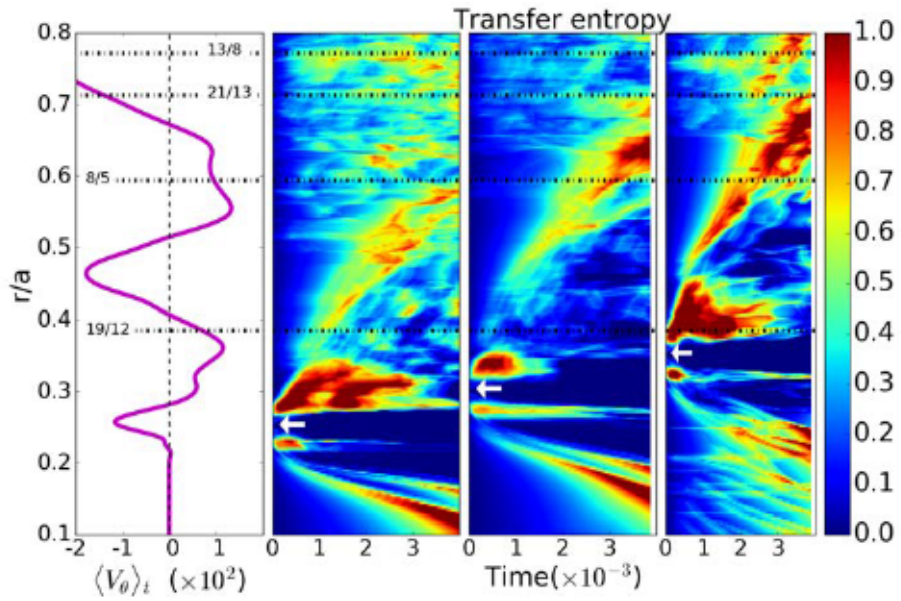

Figure 4.16: Left panel shows the temporal averaged poloidal velocity. The three five panels shows the heat evolution, using the Transfer Entropy, of three perturbations at different radial locations.

independent simulations with different (but very much alike) plasma background in order to have a better representation of the TE. Figure 4.16 is showing the TE results from the perturbations described in Fig. 4.15. The left panel is showing the temporal averaged poloidal velocity (same as Fig. 4.14), the other three panels show the TE results of a heat perturbation initially located at $r/a = 0.25$, $r/a = 0.30$, $r/a = 0.35$ respectively (white arrow). All the cases, as expected, show a radial propagation but at certain location high horizontal TE areas indicate a region where the perturbation is trapped. In the first perturbation a trapping region is observed around $r/a \approx 0.3$ which may be caused by the radial shear of the poloidal flow around that area and the strong shear just ahead at $r/a \approx 0.40$. In the second perturbation a small trapping region appears around $r/a \approx 0.35$ just before the strong radial shear in $r/a \approx 0.40$. Another high TE are appear at $r/a \approx 0.65$ which is a consequence of the very strong radial shear just starting in that point. In the third panel the same trapping region in $r/a \approx 0.65$ is present, furthermore another trapping region seems to emerge at $r/a \approx 0.4$ due to the radial shear in that location.

4.8 Experimental results

Experiments in the TJ-II stellarator have reported similar conclusions to the numerical simulations presented in this chapter. In a similar way, the Transfer entropy was applied to the electron temperature signals in a perturbative method (in this case perturbations induced by the heating). It was found that propagation of perturbation was not smooth and trapping areas were identified. Here we summarize the experimental results in Ref. [1].

In the experiment the plasma, in different discharges, is heated by the Electron Cyclotron Resonant Heating (ECRH). The average electron density is $\bar{n}_e = 0.5 \cdot 10^{19} m^{-3}$ and the electron temperature is a peaked function with a maximum at $r/a = 0$ approximately of 1KeV. The TJ-II has 12 Electron Cyclotron Emission (ECE) channels which measure the local electron temperature at 12 different radial locations [36].

The current in the external coils in TJ-II allows to determine the magnetic configuration in the device. In Ref. [1] several discharges were performed using different configurations with similar plasma parameters.

The ECRH is depositing energy in the core and spontaneous temperature fluctuations can occur [88, 89]. These perturbations may lead to a radial outward propagation of themselves or as a cascade [90]. The Transfer entropy is used in order to identify the transport of these spontaneous perturbations. Note that, in contrast to our numerical results, there are several perturbations occurring in the discharge and not only one as in the simulations.

The Transfer Entropy is applied to the electron temperature signals in the same way as the numerical simulations in this chapter. A reference signal is set (here at $\rho = r/a = 0$) and, using Eq. 4.3, the TE is applied from that reference signal to all the other signals located at different radial locations. The TE results are averaged for several discharges with same characteristics.

Figure 4.17 is showing the Transfer Entropy results for discharges using the magnetic configuration 100_44 (see Fig. 4.1). The reference signal is set at $\rho = r/a = 0$ and the horizontal dashed lines indicate the location of the main rational surfaces. The white dots in the radial axis display the radial location of the ECE detectors. The figure has been obtained averaging over 29 discharges. A radially outward propagation

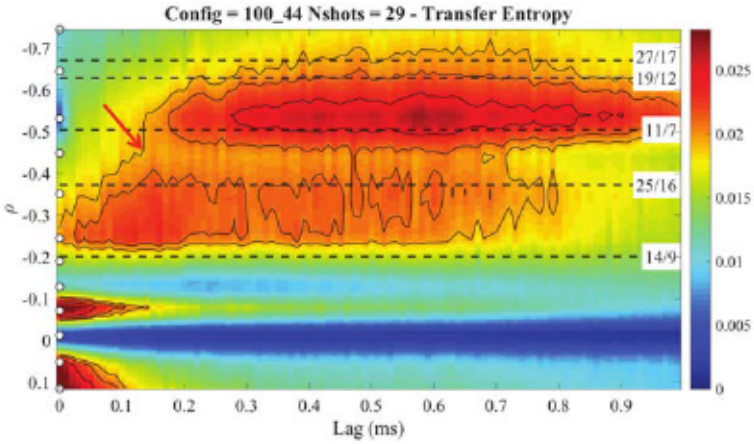

Figure 4.17: Transfer entropy of heat perturbations for the magnetic configuration 100_44. Horizontal dashed lines indicate main rational surfaces.

is clearly observed in the TE. Furthermore, two trapping regions are observed in $\rho \approx 0.3$ and $\rho \approx 0.55$ where a high TE value is extended horizontally. A red arrow indicates a "step" in the radial propagation as it has been observed in the numerical results.

Similarly the same study can be done for discharges with the 100_50 magnetic configuration. Figure 4.18 is illustrating the TE results.The reference signal is set also at $\rho = 0$. Again we observe a radial outward propagation of the perturbations and a trapping region is visible around $\rho \approx 0.55$.

Reference [1] analyses the TE for other magnetic configuration and analogous results were obtained. The TE was able to detect a radial propagation and the location of trapping regions. In that publication it was suggested that the "jumps" and trapping regions were due the presence of rational surfaces. However in our numerical simulations we observed that the radial shear of the poloidal flow (which is connected with the position of the rational surfaces) is the possible explanation for the trapping regions.

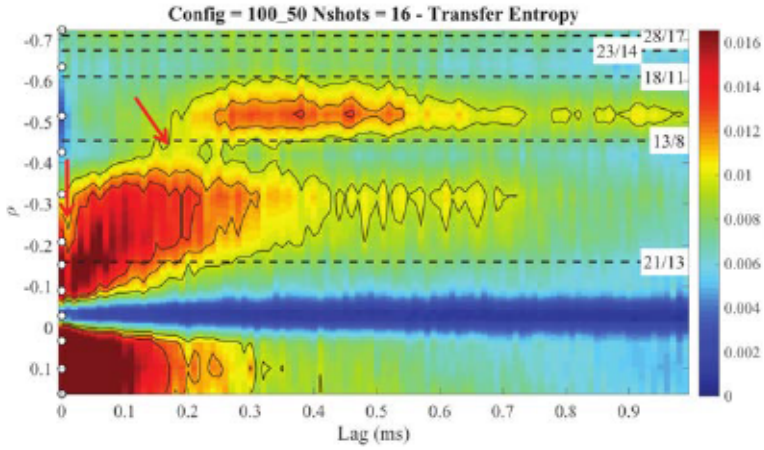

Figure 4.18: Transfer entropy of heat perturbations for the magnetic configuration 100_50.

Chapter 5

Heat propagation in W7-X

In this Chapter we apply the same approach to W7-X plasmas as we did in Chapter 4 for TJ-II. Using a perturbative method, heat transport is analyzed in numerical simulations, then the results are compared with experiments. The Transfer Entropy (TE) becomes again a useful technique to study heat transport.

W7-X stellator, as the TJ-II device, has a low magnetic shear which offers a low density of low order rational surfaces. Hence, the analysis of the impact of these surfaces (and the flow associated to them) in heat transport is clearer.

Similarly to Chapter 4, a W7-X plasma is simulated using the resistive MHD model (see Sec. 2.3.5) which main instabilities are pressure-driven modes. Once the plasma reaches the steady state, heat perturbations are set in the plasma and their time evolution is analyzed using the Transfer Entropy technique. The TE results are used to describe the heat transport. As in the previous chapter, transport exhibits a non diffusive behavior with radial areas of fast transport and other areas where the perturbations are slowed down. So heat transport seems to be dependent on the radial location and the radial shear of the poloidal flow may be the cause.

Finally, in Sec 5.3, the numerical simulations are compared with experimental results. Electron temperature signals from different discharges in the first campaign of W7-X were analyzed using the Transfer Entropy. Both numerical and experimental results exhibit same conclusions.

Part of the content of this chapter has been published in Ref. [3]: B.Ph van Milligen, U. Hoefel, J.H. Nicolau, M. Hirsch, L. García, B.A.

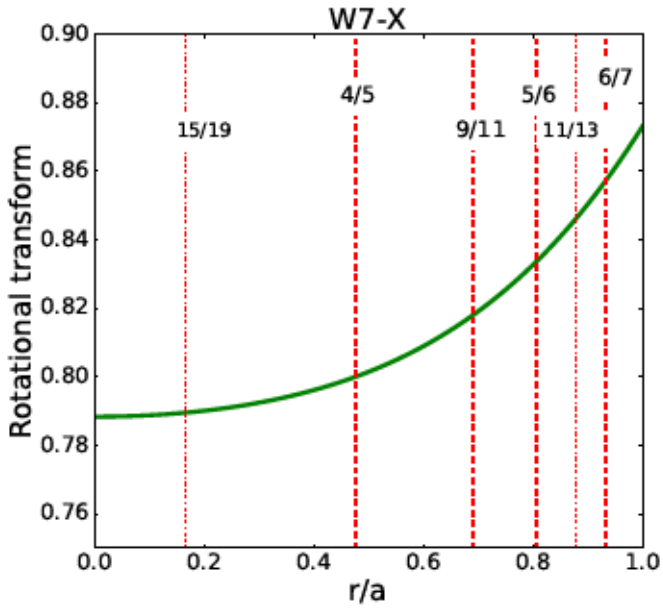

Figure 5.1: Rotational transform for the "standard" magnetic configuration in the first campaign in W7-X. Main rational surfaces are indicated with vertical lines.

Carreras and C. Hidalgo. *"Study of radial heat transport in W7-X using the transfer entropy"*. Nucl. Fusion **58**, 076002 (2018).

5.1 Steady state plasma

Before applying the perturbative method a steady state plasma is needed. Using the MHD model described in Sec. 2.3.5 a W7-X plasma is simulated. We use the *standard* magnetic configuration (see Fig. 5.1) frequently used in the experimental discharges. The initial density and electron temperature profiles are taken from the experimental results [3].

The numerical code FAR decomposes the variables in a Fourier expansion where m and n are the poloidal and toroidal numbers respectively. Only the resonant helicities according to the ι profile are added. We decide to include all the resonant helicities up to $m = 100$ which gives a total number of angular components of 425. The maximum value of m is not arbitrary but it is a large value which guarantees

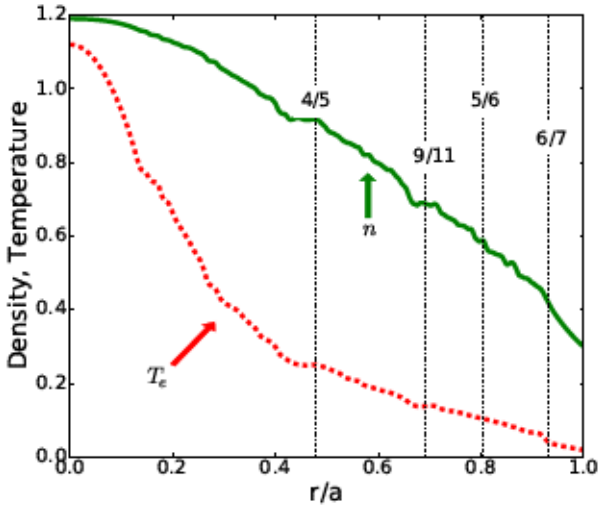

Figure 5.2: Density (solid green line) and electron temperature (dotted red line) profiles at the steady state. Main rationals surfaces are indicated by vertical dashed lines

that resistive interchange turbulence is saturated through dissipation [61].

The parameters used in the code are $S = 1.9 \times 10^6$, $\beta_0 = 10^{-3}$, $\bar{\omega}_{*e} = 2 \times 10^{-4}$ and $\bar{\omega}_{ci} = 500$. The diffusivity parameters used are $D_\perp = 0.1a^2/\tau_R$, $\chi_\perp = 1.0a^2/\tau_R$ and $\mu = 0.05a^2/\tau_R$. The parallel electron heat conductivity is $\chi_\parallel = 2 \times 10^6 a^2/\tau_R$. The diffusivities for the averaged temperature and density evolution are $D_{0\perp} = 0.3a^2/\tau_R$ and $\chi_{0\perp} = 0.2a^2/\tau_R$. The collisional flow damping rate is $\hat{\mu} = 40\tau_R^{-1}$.

Using that parameters in the model, the equations (Sec. 2.3.5) are numerical advanced until a steady state is reached by the plasma. Figure 5.2 illustrates the density (solid line) and electron temperature (dotted line) profiles at the steady state. A source term is included in the model to keep these profiles in a stationary state. The profiles are not constant but their changes are negligible in the present study.

In the next section heat transport will be analyzed together with the average poloidal flow $\langle V_\theta \rangle$ where the brackets indicate a poloidal and toroidal average. In our studies the flow is stationary and fluctuates around an equilibrium profile. Figure 5.3 is showing a temporal average of the poloidal flow $\langle V_\theta \rangle_t$. The temporal average has been

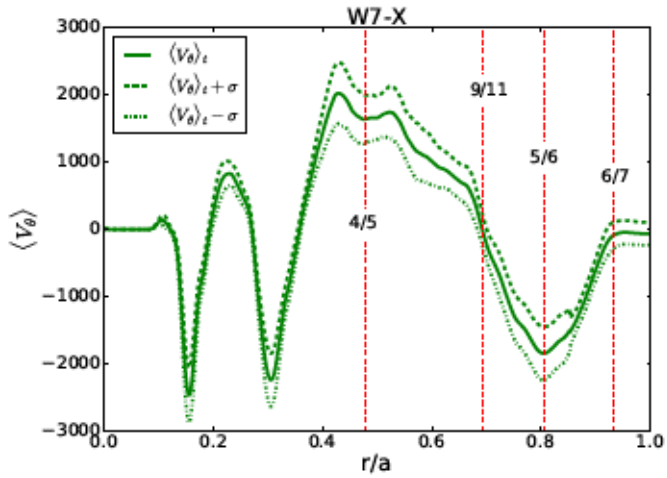

Figure 5.3: Temporal averaged poloidal velocity at steady state(solid green line). Dashed and dotted lines indicate one standard deviation from the mean value.

calculated for a $\Delta t = 0.05 t_R$ which is a time much longer than any of our studies. The solid line represents the temporal average and the dashed and dotted indicate one standard deviation σ from that average so the distance between the two lines is 2σ. From that figure we can conclude that the fluctuations in the poloidal flow must be small.

5.2 Heat perturbations

Heat transport is analyzed following similar proceeding as in Chapter 4. We set a heat pulse in our steady state plasma and then study its temporal evolution. The pulse must be small to not perturb in excess the plasma but at the same time large enough to be able to analyze its evolution. Consequently, we use perturbations with a Gaussian shape with a maximum $\Delta T_e = 1.5$ and width $\sigma^2 = 0.005$.

Five simulations are run independently and a heat perturbation is set in each one. Each perturbation is localized in a different radial location in order to analyze transport in different radial regions. Figure 5.4 shows in the right five panels the time evolution of the perturbations initially located at $r/a = 0.2$, $r/a = 0.25$, $r/a = 0.35$, $r/a = 0.45$ and $r/a = 0.55$ respectively. The temperature profile just before introducing the perturbations has been subtracted to plot

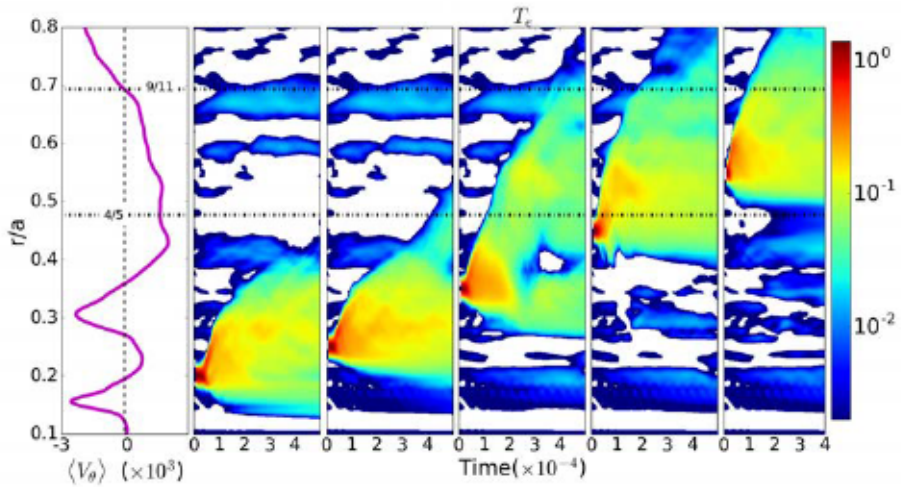

Figure 5.4: Left panel indicates the average poloidal flow before the perturbations. The five right panels show the temporal evolution of a heat perturbation at $r/a = 0.2$, $r/a = 0.25$, $r/a = 0.35$, $r/a = 0.45$ and $r/a = 0.55$.

only the evolution of pulses. The left panel is illustrating the average poloidal flow before the perturbations.

All the perturbation in Fig. 5.4 exhibit an outward radial propagation, however that propagation is different in each case. Note that the outer perturbations seem to propagate faster than the inner ones which is consistent with experimental results in other devices [51]. Moreover, as time advances the perturbations propagate but at certain radial location the propagation seems to slow down.

The way that propagation changes at different radial locations suggested us that the reason might be the presence of a radial shear in the poloidal flow $d\langle V_\theta \rangle / dr$. For example in $r/a \approx 0.32$ the propagation seems to slow down in the first and second perturbation. In the third perturbation, there is radial propagation but part of the perturbation seems to be trapped around the initial radial location (where a high shear in the flow is present). Fourth and fifth perturbations exhibit a trapping region around $r/a \approx 0.58$ where a small (but radially extended) shear region appears. In Sec. 5.2.1 the Transfer Entropy will be applied to this numerical data and this behavior will become more evident.

5.2.1 Transfer Entropy analysis

Here we apply the Transfer Entropy technique to the numerical results in Fig. 5.4 of heat perturbations in a W7-X plasma. The technique was introduced in Chapter 3 and it has been already applied to the numerical results in TJ-II plasmas in Sec. 4.5.

The Transfer Entropy is able to quantify the information flow from two signals. Essentially it measures the information contained in both time signals and identify if previous information is affecting to present events. Having two signals $X = (x_1, x_2, \ldots)$ and $Y = (y_1, y_2, \ldots)$ the Transfer Entropy quantifies the amount of information in bits which signal X can be *predicted* using not only the information in X but also the information contained in Y.

As we are focused in heat transport, we are interested in how perturbations are propagating in time. In our numerical simulations (and in experiments) we measure the electron temperature for certain time at various radial locations and we want to analyze how a perturbation, initially located at some radius, is affecting other radial locations at future times. To do such analysis the TE can be applied from the signal located to the initial radial location (Y) to the other signal established in a different location (X). So the TE should be able to identify if the perturbation (initially observed in Y) is affecting at future times the temperature values in the radial location of X.

Therefore the Transfer Entropy can be applied from the *reference* signal Y (set in the initial radial location of the perturbation) to different signals X corresponding to the time signal of temperature at different radial locations. This approach can be applied to the numerical simulations from Fig. 5.4 for each perturbation case. The TE results are plotted in the five right panels in Fig. 5.5 which correspond to the perturbations initially located at$r/a = 0.2$, $r/a = 0.25$, $r/a = 0.35$, $r/a = 0.45$ and $r/a = 0.55$ respectively. The white arrow indicates the radial location of the reference signal in the TE calculation which is set in purpose in the initial location of the perturbations. The TE results in each panel has been averaged for six independent simulations of a perturbation with similar background (same as we did in Sec. 4.5)

The TE results from Fig. 5.5 show how the information is propagated during the evolution of the heat perturbations. However, despite of seeing information flowing, the results are showing the same prop-

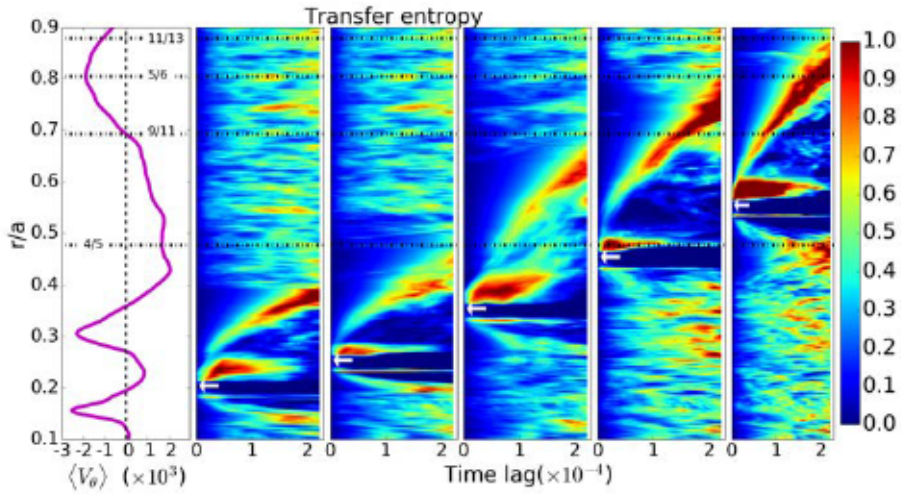

Figure 5.5: Left panel shows the temporal averaged poloidal velocity. The right five panels show the heat evolution, using the Transfer Entropy, of five perturbations at different radial locations.

agation as the pulses. All the perturbations show a radial outward propagation, although the outer ones exhibit a faster propagation than the inner ones. Furthermore we can identify some high TE areas extended horizontally which indicate a *trapping* zone. The appearance of these trapping areas suggest the presence of (mini) transport barriers. The generation of these mini transport barriers may be due the radial shear in the poloidal flow.

The first perturbation in Fig. 5.5 shows a trapping region around $r/a \approx 0.25$ probably because the strong flow shear in $r/a \approx 0.28$. In the first, second and third perturbation a trapping region appears around $r/a \approx 0.37$ where a strong shear is present. Fourth and fifth perturbations show a high TE area but propagating outwards. However, the fifth perturbation shows a trapping region around $r/a \approx 0.6$, whose reason seems to be the weak shear but for an extended radial region.

5.3 Experimental results

Here we summarize some of the experimental results published in Ref. [3]. In that work the Transfer Entropy was applied to experimen-

tal data from electron temperature measurements in the first campaign in W7-X [39]. The approach used is similar to the numerical simulations presented in Sec. 5.2, using a perturbative method (perturbations induced by the external heating) the TE is applied to the data to analyze heat transport. The experimental results exhibit analogous conclusions.

In the different analyzed discharges the plasma is heated by the Electron Cyclotron Resonant Heating (ECRH). The density was low $\bar{n}_e = 1 \sim 2 \cdot 10^{19} m^{-3}$ and the power deposited by the ERCH was of the order $P_{\text{ECRH}} = 0.6 \sim 2MW$ which allow a peaked temperature profile with a maximum of $4 \sim 5$ KeV. The W7-X device contains 32 Electron Cyclotron Emission (ECE) channels covering a large radial region which measure the local electron temperature [91, 92].

The external coils generate the magnetic configuration in W7-X. In this work different magnetic configurations were analyzed. In spite of the fact that in the discharges the pressure and the (bootstrap) currents were low, the experimental data was analyzed taking into account that the iota profile could be slightly deviated from the rational surfaces in vacuum.

During the ECRH heating, spontaneous heat perturbations may appear in the discharges [89] and can propagate outward. Using the Transfer Entropy it was possible to analyze these perturbations and their radial propagation in the plasma.

The approach in the experiment is identical to the numerical simulations in this chapter. The electron temperature is measured at different radial locations during ECRH discharges. The Transfer Entropy is applied to the temperature signals as we did in Sec. 5.2.1. Figure 5.6 is showing the TE results having the reference probe at $\rho = r/a = 0.2$. The vertical axis represents the radial direction and the white dots on it show the position of the ECE detectors. The horizontal thin dashed lines indicate the location of the main rational surfaces. During this discharge the *standard* magnetic configuration was used (same as in the numerical simulations).

The high TE areas in Fig. 5.6 show a radial outward propagation and one of the possible *paths* is emphasized with a thick dashed curve. The heat transport seems to be not smooth and trapping regions appear in the high TE areas in $\rho = 0.4$ and $\rho = 0.7$. The heat transport seems to "jump" between these trapping regions because between them the TE is low.

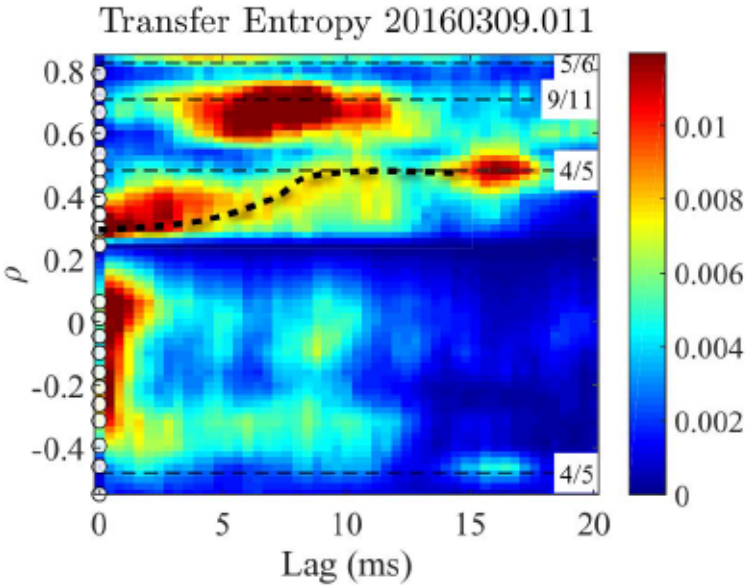

Figure 5.6: Transfer entropy of heat perturbations for the standard magnetic configuration. Horizontal dashed lines indicate main rational surfaces.

Figure 5.7 is showing the TE results for another discharge but using a different magnetic configuration. For this configuration (called "3" in Ref. [3]) the rational surfaces are shifted, the dashed horizontal lines indicate the new locations. Again we observe a radial outward propagation with stagnation regions. Thick dashed curves highlight the paths of the radial propagation.

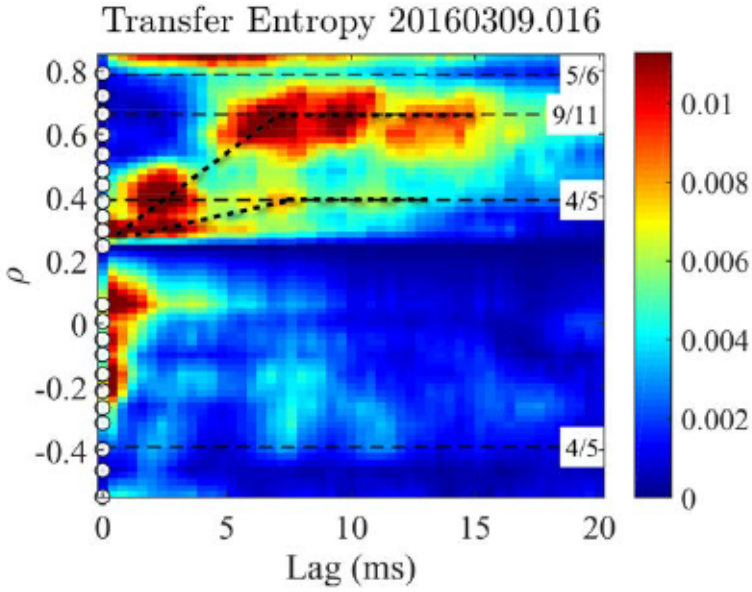

Figure 5.7: Transfer entropy of heat perturbations for a different magnetic configuration.

Chapter 6

Quantifying transport: Effective diffusivity

In Chapters 4 and 5 heat transport in two stellarators was analyzed using the Transfer Entropy (TE) technique. However the analysis was only done qualitatively, we could only identify whether the radial propagation was "faster" or "slower" and the presence of trapping regions. So, the following question arises: can the Transfer Entropy *quantify* heat transport? In this Chapter we propose an approach, based on the TE technique, to estimate an effective diffusivity in Fusion Plasmas.

Heat transport in magnetically confined fusion plasmas has been an important issue for decades. Experimental observations have shown that transport cannot be explained within the classical transport theory as it obeys a non-diffusive behaviour [93]. One possible approach is to use *effective diffusivities* to quantify transport. These approach "averages" transport in a certain region and estimates an effective coefficient (diffusivitty) which reproduces a similar behavior within the diffusive theory.

In the spirit of the "q-comb" model [94, 95], here we use an approach which assumes that the heat diffusivity is a local quantity and depends on the radial position. So for a small radial interval the diffusivity is a constant. As a result, we obtain a heat diffusivity which is a function of the radius. Using the Transfer Entropy and perturbative methods, a local effective diffusivity is estimated for small radial regions in simulations of TJ-II plasmas.

To demonstrate the effectiveness of our approach (based on the TE), it is applied first to a known diffusive model. Then it is used

in numerical simulations of TJ-II plasma for two different magnetic configurations. The effective diffusivities yielded from this approach are compared with the ones obtained from local quantities (flux and gradient).

Most of the content in this Chapter has been published in Ref. [4]: J.H. Nicolau, L. García, B.A. Carreras and B.Ph van Milligen. *"Applicability of Transfer Entropy for the calculation of effective diffusivity in heat transport"*. Phys. Plasmas **25**, 102304 (2018).

6.1 Transfer Entropy approach

A diffusive model in one dimension is described by the following expression

$$\frac{\partial T_e}{\partial t} = D\frac{\partial^2 T_e}{\partial r^2}. \tag{6.1}$$

where the constant D is the diffusivity and T_e is the quantity which is diffusing (for convenience temperature). The solution of this equation is the well known probability distribution function

$$P\left(r,t\right) = \frac{1}{\sqrt{2\pi\sigma^2}}\mathrm{e}^{-\left(\frac{r^2}{2\sigma^2}\right)} \tag{6.2}$$

where the variance is $\sigma^2 = 2Dt$. The average of r integrating from the center of the perturbation is

$$\langle r\rangle = \int_0^\infty rP(r,t)\,dr = \sqrt{\frac{4Dt}{\pi}}. \tag{6.3}$$

These general results are only valid if the diffusivity D is constant throughout the system and in the absence of other ingredients (such as convection and specific boundary conditions). That is neither the case in Fusion plasmas nor our numerical simulations. However we propose an approach where we assume that D is constant for a small radial region and, therefore Eq. 6.3 is valid in that region too.

In this approach, a perturbation is introduced at a specific radial location and then its time evolution is analyzed. As the perturbation is diffused, its amplitude decays. The transfer entropy is useful to circumvent this problem, as it visualizes the propagation, regardless of the amplitude of the signal. In spite of the fact that TE does not

measure heat propagation directly, it is still a good representation of the geometric evolution of the perturbation. This was already shown in the modulation experiments reported in Ref. [3]. Thus, it should be possible to extract an effective diffusivity D that is just a measure of this geometric expansion.

In the next sections, we are able to compare this estimate of an effective D with other, more traditional techniques. Note that the average or standard deviation of the perturbed quantities does not provide good results, due to the fact that D is not constant across the system. In the approach proposed here, we calculate

$$\langle r \rangle = \frac{\int r\ TE\ dr}{\int TE\ dr} \tag{6.4}$$

from the TE results, but only over small radial intervals, assuming that the diffusivity is constant in those intervals.

6.2 Applicability

6.2.1 Diffusive model

To illustrate the method based on the TE approach, it is first applied to a cylindrical system where the diffusion equation (Eq. 6.1) becomes

$$\frac{\partial T_e}{\partial t} = \frac{1}{r}\frac{\partial}{\partial r}\left(rD\frac{\partial T_e}{\partial r}\right). \tag{6.5}$$

The diffusion coefficient in this system is defined as

$$D = \begin{cases} D_0, & 0 \leq r < 0.5 \\ 10D_0, & 0.5 \leq r \leq 0.6 \\ 5D_0, & 0.6 < r \leq 1 \end{cases}$$

and $D_0 = 10^{-8}$ in our numerical simulations. In this way, the system has three regions with constant (but different) diffusivity.

Using a source to maintain a steady state profile, a perturbation is introduced at $r = 0.25$ and its temporal evolution is studied. The

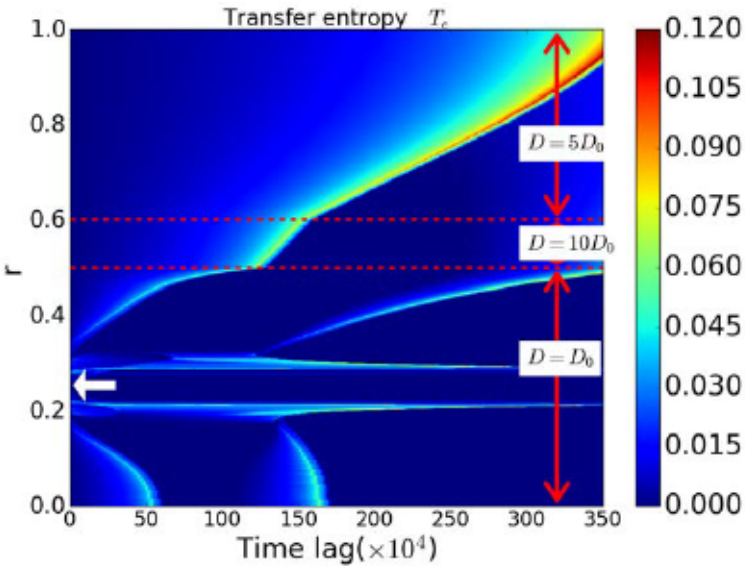

Figure 6.1: Transfer Entropy for a perturbation located in $r = 0.25$ in the diffusive model. Vertical arrows indicate the actual values of diffusivity in that radial region.

Transfer Entropy is calculated from the location of the pulse to all other radial positions (similar as it was done in Sec. 4.5)

Figure 6.1 shows the Transfer Entropy illustrating the radial propagation of the perturbation. The white arrow indicates the initial location of the pulse and the reference signal. Red horizontal dashed lines illustrate the boundaries between regions with same diffusivity. The vertical arrows show the real diffusivity value in that radial region. The radial propagation of the perturbation is clearly seen in the Transfer Entropy. Furthermore the propagation changes as the perturbation crosses the boundary with a different diffusivity. A second trace in TE at higher time lag in Fig. 6.1 is associated with modifications and nonlinear responses of the equilibrium to the propagation of the pulse.

Now we take small radial intervals and calculate the $\langle r \rangle$ using Eq. 6.4. In general the intervals must be smaller than the actual regions of variation of D to avoid mixing the effect of various D values. Here we use different radial intervals of the same size $\Delta r = 0.05a$. Figure 6.2 shows the results of that method applied to the perturbation in Fig. 6.1. Initially, the $\langle r \rangle$ curves are horizontal, showing only

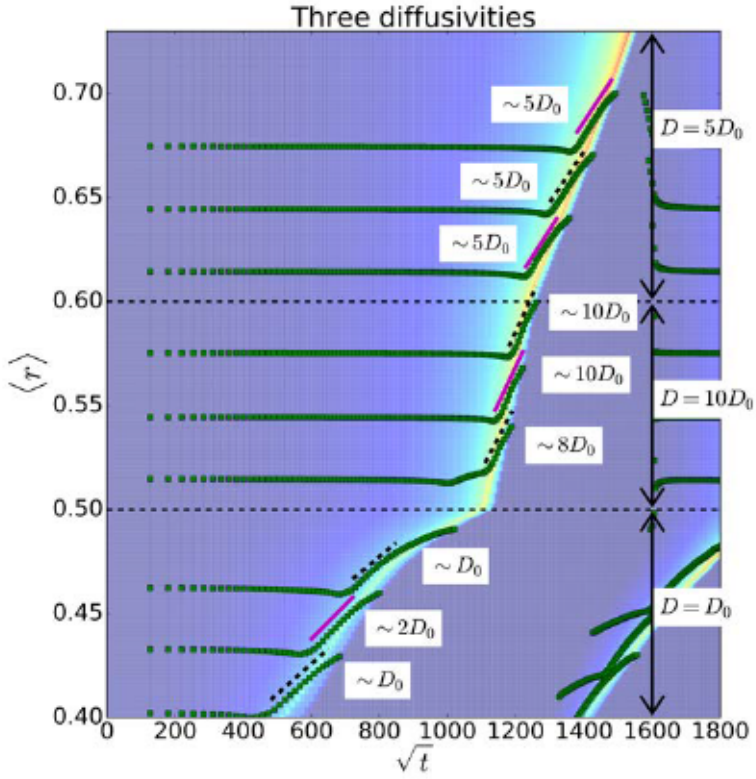

Figure 6.2: Average $\langle r \rangle$, calculated over small radial intervals, as a function of the squared root of time, from the Transfer Entropy results in a simple diffusive system. Arrows indicate the preset values of diffusivity D and their corresponding regions. For each case, a fit line is shown, from which an effective value of the diffusivity can be obtained. The background shows the Transfer Entropy.

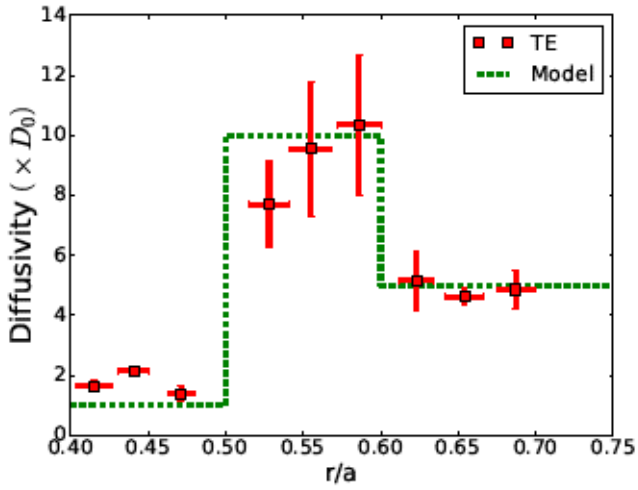

Figure 6.3: Comparison between effective diffusivities obtained from the Transfer Entropy (red dots) and the preset model diffusion coefficients (green dashed line).

the average of the interval because the pulse has not arrived yet. The transfer entropy is plotted in the background, illustrating the radial propagation of the perturbation. All curves show a linear variation at times that match the "arrival" of the perturbation in the corresponding region. A straight line is fitted to the curves and, using Eq.6.3, corresponding values of D are obtained.

The values of D obtained from Fig. 6.2 are now compared in Fig. 6.3, where the red dots represent the values obtained using the transfer entropy technique and the dashed line is the actual diffusion coefficient in the model. The errors in the TE curve are obtained as follows. The horizontal error is not an actual error but the radial interval (the vertical direction in Fig. 6.2) of the linear fit. The vertical error is more complex as it exhibits the effect of choosing the region to fit and its impact on the D calculation. The error is obtained using the maximum likelihood method [96] and it takes into account all the reasonable linear fittings in the region of interest. The likelihood L is defined as

$$\log L\left(i_{\min}, i_{\max}\right) = \sum_{i_{\min}}^{i_{\max}} -\frac{\left(y\left(i\right) - y_{\text{fit}}\left(i\right)\right)^2}{2\left(\Delta y\left(i\right)\right)^2} \tag{6.6}$$

where $[i_{\min}, i_{\max}]$ is the $\sqrt{t}$ interval (the horizontal direction in Fig. 6.2)

where the linear fit is made. So, a perfect fit such that $y(i) = y_{\text{fit}}(i)$ would yield $\log L = 0$. From all the different values of L we pick the ones which $L > \max(L)/e$, then we average all the slope values satisfying this condition to get the final slope for the D calculation. The error is obtained from the standard deviation of this average.

The effective diffusivities obtained from the TE in Fig. 6.3 are not exactly equal to the preset values, but show the same trend and have the same amplitude. In the region $r < 0.5$, the calculated D is small and close to the real D value. In the next region, $0.5 < r < 0.6$, the effective diffusivity is significantly higher than in the preceding region, the values do no match exactly the real D but they are close. In the third region, $r > 0.6$, the effective D decreases in accordance with the decrease of real D.

6.2.2 MHD model

Here, we calculate the average $\langle r \rangle$ from the different Transfer Entropy results from MHD simulations in Sec. 4.5. As in the diffusive example (Sec. 6.2.1), the average of r is calculated in small radial intervals assuming, again, that the diffusivity is constant in each region.

Figure 6.4 shows the average $\langle r \rangle$ of small radial intervals of size $0.07a$ as a function of $\sqrt{t}$, for the perturbation located at $r/a = 0.35$ (the second case in Fig. 4.10). The Transfer Entropy is represented in the background, showing the radial propagation of the perturbation. We choose the region to fit the slope as the time where the perturbation arrives to this radial location which is easily obtained by superposing the Transfer Entropy. An effective diffusivity D can be then calculated using Eq.6.3 by making a linear fit.

In order to assess the effectiveness of the Transfer Entropy technique, we compare the values obtained from TE with estimates of D from other approaches. One simple way to obtain the diffusivity, in the context of (heat) transport, is using Fourier's Law $\Gamma = -D\nabla T_e$ where $\Gamma = \langle \tilde{V}_r \tilde{T}_e \rangle$ is the heat flux and ∇T_e is the electron temperature gradient. Both quantities are averaged poloidally and toroidally. The electron temperature gradient can be obtained from the T_e profiles.

Using the Transfer Entropy, the effective diffusivity D can be obtained for the different cases in Sec. 4.5. Likewise, from the simulations we can calculate the heat flux and temperature gradient and then apply $D = -\Gamma/\nabla T_e$.

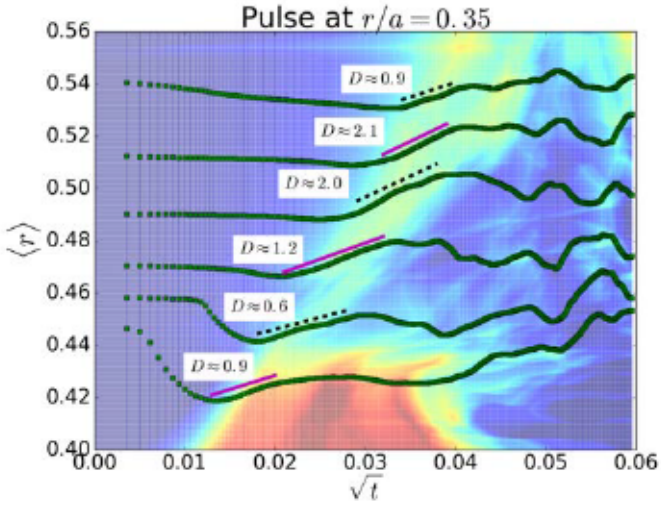

Figure 6.4: Results from resistive MHD simulations. Dotted lines show the average value $\langle r \rangle$, calculated from the Transfer Entropy, for a perturbation launched at $r/a = 0.35$, as a function of the squared root of time. Each dotted curve is the average over a small radial interval. The slope of the fit lines shown are used to calculate and effective D, using Eq. 6.3. The background shows the Transfer Entropy.

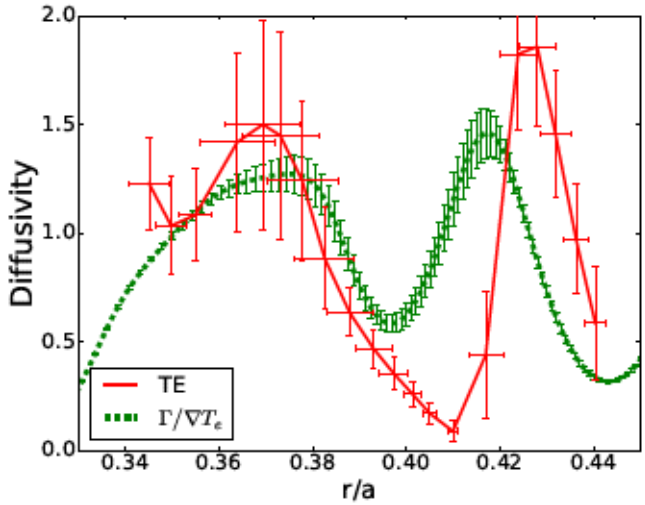

Figure 6.5: The green dotted line is the effective diffusivity D calculated from the temperature gradient and the heat flux corresponding to the pulse launched at $r/a = 0.25$. The solid line is the effective D obtained from the Transfer Entropy.

Figures 6.5, 6.6 and 6.7 show a comparison between the diffusivity from the TE approach and from Fourier's Law for the perturbations launched at $r/a = 0.25$, $r/a = 0.35$ and $r/a = 0.45$, respectively. The dotted line represents the ratio $|\Gamma/\nabla T_e|$ where Γ and ∇T_e have been averaged in time over the duration of the pulse. The solid line represents the D values obtained by taking small radial intervals and applying Eq. 6.3 to the TE (as in Fig. 6.4). The error bars in the $|\Gamma/\nabla T_e|$ curve are obtained from the standard deviation of the temporal variation of Γ and ∇T_e. One can observe that the two different approaches are showing similar trends and values for diffusivity D. One may conclude that the Transfer Entropy is capable of analyzing heat transport and making a correct estimate of the effective diffusivity.

Note that the Transfer Entropy is a measure of information flow among signals and it is not an actual measurement of diffusivity. However, using the TE technique we obtain similar values to $|\Gamma/\nabla T_e|$ during the perturbation (see Fig. 6.5, 6.6 and 6.7). Some of the discrepancies observed in these figures, and in the next examples, may be due to the nature of the two different approaches. The TE measures

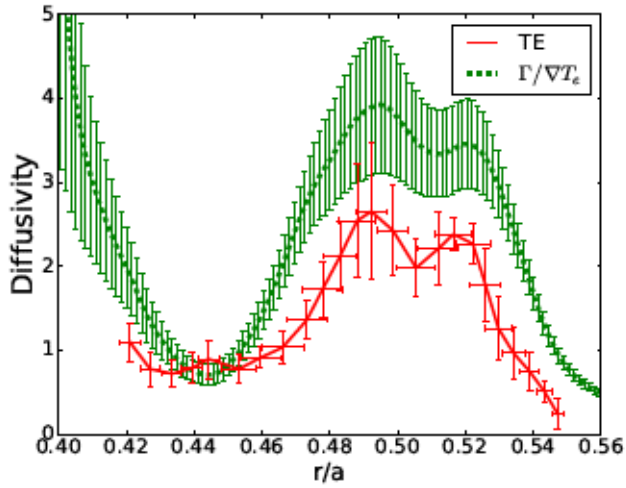

Figure 6.6: Same as Fig. 6.5 but for a perturbation launched at $r/a = 0.35$.

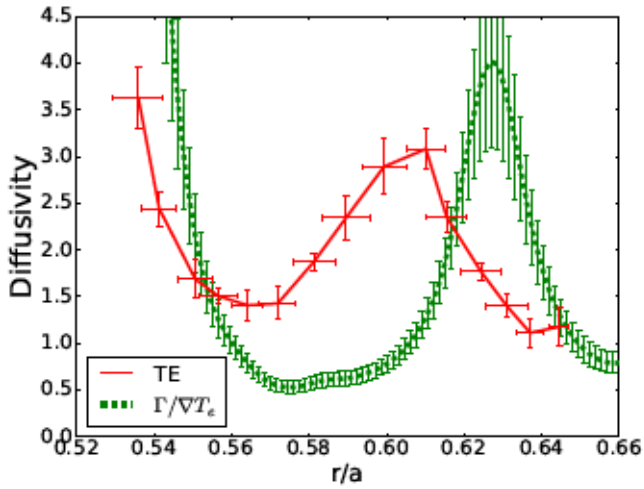

Figure 6.7: Same as Fig. 6.5 but for a perturbation launched at $r/a = 0.45$.

the propagation of information, which is not fully equivalent to the propagation of heat, as discussed in Ref. [3]. So it is unsurprising that an effective diffusivity deduced from the TE cannot be identical to the diffusivity deduced from traditional methods.

6.2.3 Magnetic configuration 100_46

Here we provide more examples of the TE technique using a different magnetic configuration. We use the plasma described in Sec. 4.7 which is simulated under the magnetic configuration 100_46. In this configuration, the 8/5 rational surface is located in an inner region and the 5/3 appears at the edge. The parameters of the plasma are the same as in Sec. 6.2.2 but the density and temperature profiles are different as well as the poloidal flow. Therefore, the regions of "high or low" diffusivity should be different.

As before, different heat perturbations are introduced in the plasma. The transfer entropy technique is again used to analyze the heat transport, as in Sec. 6.2.2, similar conclusions are obtained. The TE exhibits radial heat propagation and radial trapping regions. These regions are not the same as in the previous configuration, due to the fact that the rational magnetic surfaces and the poloidal flow are not the same.

Again, the TE is used to calculate the effective diffusivity with the $\langle r \rangle$ method. These results are compared to the diffusivity from Fourier's law, $D = -\Gamma/\nabla T_e$. Figures 6.8 and 6.9 exhibit the diffusivities obtained with both approaches for perturbations launched at $r/a = 0.25$ and $r/a = 0.30$, respectively. Again, trends are more or less similar.

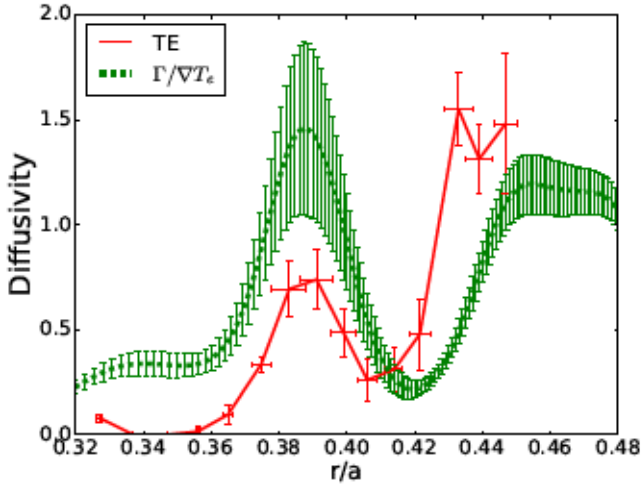

Figure 6.8: The green dotted line is the effective diffusivity D calculated from the temperature gradient and the heat flux corresponding to the pulse launched at $r/a = 0.25$ in the 100_46 configuration. The solid line is the effective D obtained from the Transfer Entropy.

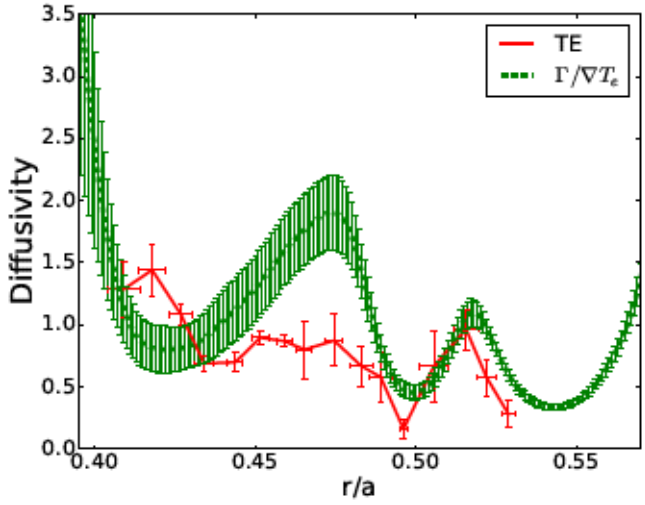

Figure 6.9: Same as Fig. 6.8 but for a perturbation initially located at $r/a = 0.30$.

Chapter 7

Transport barriers and turbulent vortices

In Chapters 4 and 5 heat transport in two different stellarators has been analyzed. The approach was based on perturbative methods, thus heat pulses were located at different radial locations and their temporal evolution were analyzed. We observed that heat perturbations radially propagate faster or slower at different radial regions. Similar conclusions were obtained using the Transfer Entropy technique. We concluded that the radial shear of the poloidal flow was an important factor to determine the radial heat transport.

In this Chapter the poloidal flow in the plasma is analyzed. The aim is to identify (and characterize) some of the elements that involve the poloidal flow generation. Plasma turbulence, as resistive interchange modes in our MHD model, will play an important role in this issue. The turbulent fluctuations will determine the average poloidal flow. Furthermore, turbulent vortices are observed in the main low order rational surfaces.

In the last section of this Chapter, we focus on the heat transport barriers and its relation with the poloidal flow.

7.1 Turbulence and perpendicular flow

In our model (see Sec. 2.3.5) the perpendicular velocity, $\vec{E} \times \vec{B}$, is obtained by

$$\overrightarrow{V_\perp} = -\nabla\Phi \times \hat{\zeta}. \tag{7.1}$$

so the radial and poloidal components are

$$V_r = -\frac{1}{r}\frac{\partial \Phi}{\partial \theta} \qquad V_\theta = \frac{\partial \Phi}{\partial r}. \tag{7.2}$$

Hence the perpendicular velocity is determined by the electrostatic potential Φ.

On the other hand, it has been shown [62] that in a model based on the resistive interchange modes the average poloidal flow is generated by the fluctuating components of the velocity $\tilde{V}_r \tilde{V}_\theta$. These fluctuating terms are determined by the turbulence so the nature of this turbulence will have an impact on the flow generation. How the average poloidal flow is generated is discussed in detail in Section 7.2.

Interchange modes are one specific type of pressure-driven turbulence. They are characterized by having constant perturbations along the magnetic field lines so the effect intensifies in the closed field lines. In a fusion plasma device the magnetic configuration establishes the location of the closed field lines or rational surfaces. Fluctuations are located around rational surfaces so in these locations a high average poloidal flow will be generated as it will be shown in Section 7.2.

Therefore, we focus now in the study of these fluctuations caused by the interchange instabilities. A simplified analytical expression for a fluctuation caused by the interchange modes should be of the form

$$\Phi_{m,n} = A e^{-\frac{(r-r_s)^2}{w^2}} \cos\left(m\theta + n\zeta\right) \tag{7.3}$$

where r_s is the radial location of the rational surface, w indicates the width of the fluctuation and A is an arbitrary amplitude of the fluctuation. Basically the fluctuation is a Gaussian-like function centered in the rational surface r_s along the field line as a helix. Then the perpendicular components of the velocity (using Eq. 7.2) are

$$V_r = \frac{Am}{r} e^{-\frac{(r-r_s)^2}{w^2}} \sin\left(m\theta + n\zeta\right) \tag{7.4}$$

$$V_\theta = -\frac{2A\left(r-r_s\right)}{w^2} e^{-\frac{(r-r_s)^2}{w^2}} \cos\left(m\theta + n\zeta\right). \tag{7.5}$$

As a consequence, the V_r shows an angular shift so the radial velocity is maximum between fluctuations and the V_θ is proportional to Φ

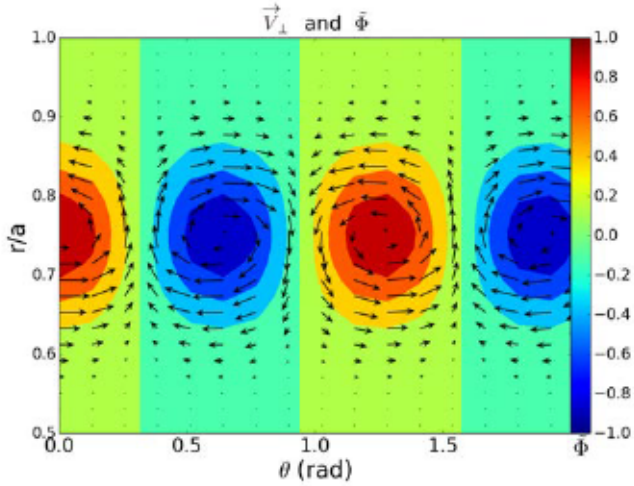

Figure 7.1: Analytical electrostatic potential fluctuation Φ for the 8/5 rational surface. The arrows represent the perpendicular velocity generated by this electrostatic potential.

but has a minimum at $r = r_s$. To visualize these results, we take the $n = 8/m = 5$ component from the 100_44 magnetic configuration in TJ-II. Figure 7.1 shows in colors the $\Phi_{8,5}$ for a fixed toroidal angle. The arrows illustrate the direction and magnitude of the perpendicular velocity generated by this electrostatic potential fluctuation. Clearly the perpendicular velocity generated by this turbulent fluctuations is forming vortices centered in these fluctuations. Since these fluctuations are distributed along the field lines, the generated vortices must have the same structure. The structure of these vortices is studied in detail in Chapters 8 and 9.

However, the presence of these vortices does not imply the generation of an average flow. In fact, in the next section (Sec. 7.2) we are going to demonstrate that this model of fluctuation does not contribute to the generation of an average flow.

7.2 Average poloidal flow

The poloidal flow generation under the MHD model of pressure-driven turbulence with diamagnetic effects has been studied, for example, in Ref. [62] and [97]. To obtain an expression for the poloidal flow evolu-

tion, the momentum balance equation (see Eq. 2.50) can be averaged on the flux surface, which in the cylindrical geometry of our model is a poloidal and toroidal angular average. So, in general, the average for a function f is

$$\langle f(r,\theta,\zeta)\rangle = \frac{1}{4\pi^2}\iint f(r,\theta,\zeta)\ d\theta\ d\zeta. \tag{7.6}$$

Therefore, the function can be decomposed in an average and fluctuating part $f = \langle f\rangle + \tilde{f}$. Note that the $\langle f\rangle$ is equal to the $(0,0)$ component in the Fourier decomposition since all the other components vanishes in the angular average.

Averaging the momentum balance equation we obtain the equation for the average poloidal flow

$$\frac{\partial \langle V_\theta\rangle}{\partial t} = -\frac{1}{r^2}\frac{\partial}{\partial r}\left(r^2 S_{r\theta}\right) - \mu \langle V_\theta\rangle, \tag{7.7}$$

where $S_{r\theta}$ is the non-diagonal $r\theta$ component of the stress tensor

$$S_{r\theta} = \left\langle \tilde{V}_r \tilde{V}_\theta \right\rangle - S^2 \left\langle \tilde{B}_r \tilde{B}_\theta \right\rangle. \tag{7.8}$$

The two terms of $S_{r\theta}$ are the electrostatic (or Reynolds stress in physics of fluids) and magnetic components respectively. The electrostatic term arise from the convective term in the momentum equation and the magnetic component emerges from the parallel derivative in the parallel current. In our model, and due to the parameters we use to study TJ-II, the magnetic component is going to be negligible as the resistive interchange instability is basically electrostatic.

Equation 7.7 accounts for the interaction between poloidal flow and turbulence. The first term, which involves the effect of turbulence perturbations, is a growth term. As the turbulence increases the poloidal flow increases as well. However the $\mu\langle V_\theta\rangle$ is a dissipative term so as the $\langle V_\theta\rangle$ increases the dissipation becomes significant and the poloidal flow may stabilize.

The increase of the average poloidal flow is an important factor in turbulence suppression [97, 47, 98]. An increase in (the radial shear of) the average poloidal flow may diminish the turbulence and so the Reynolds stress. Therefore, poloidal flow and turbulence interacts as a predator-prey model (see Fig. 7.2), as one increases the other decreases. Eventually the system reaches a steady state where average

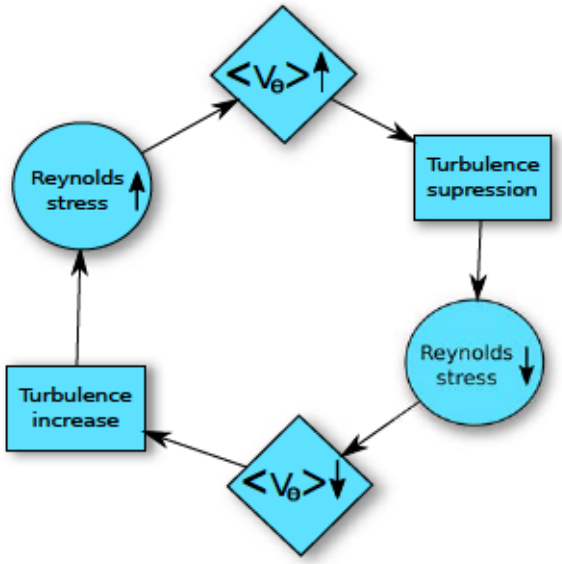

Figure 7.2: Flowchart of the interaction of the poloidal flow and turbulence.

poloidal flow and turbulence exhibit an equilibrium.

First we can calculate the average poloidal flow generated by the analytical example described in previous section (Sec. 7.1). In that example we presented a single fluctuation with the basic characteristics of resistive interchange modes. The perpendicular components of the velocity V_r and V_θ were already obtained in Eq. 7.4 and 7.5 so that allows to calculate the electrostatic term in the stress tensor

$$\langle V_r V_\theta \rangle \propto \iint sin\,(m\theta + n\zeta)\cos\,(m\theta + n\zeta)\;\; d\theta\; d\zeta = 0. \qquad (7.9)$$

Since the stress tensor is zero, and it is the dominant term in $S_{r\theta}$, no average flow be generated according to Eq. 7.7. This particular result is valid when there is no rotation and only one parity (sine or cosine) is included in the Fourier expansion. In our model, which includes diamagnetic terms, fluctuations have both sine and cosine components,

$$\tilde{\Phi} = \sum_{m,n} \left[\Phi^C_{m,n} \cos\,(m\theta + n\zeta) + \Phi^S_{m,n} \sin\,(m\theta + n\zeta)\right]. \qquad (7.10)$$

Let's take one single mode (m, n) to see its contribution to the Reynolds

stress, so

$$\left\langle \tilde{V}_r \tilde{V}_\theta \right\rangle_{m,n} = \frac{1}{4\pi^2} \frac{m}{r} \iint \left[\Phi^C_{m,n} \sin(m\theta + n\zeta) - \Phi^S_{m,n} \cos(m\theta + n\zeta) \right] \times \left[\frac{\partial \Phi^C_{m,n}}{\partial r} \cos(m\theta + n\zeta) - \frac{\partial \Phi^S_{m,n}}{\partial r} \sin(m\theta + n\zeta) \right] d\theta \, d\zeta \tag{7.11}$$

and after some calculations

$$\left\langle \tilde{V}_r \tilde{V}_\theta \right\rangle_{m,n} = \frac{1}{2} \frac{m}{r} \left[\Phi^C_{m,n} \frac{\partial \Phi^S_{m,n}}{\partial r} - \Phi^S_{m,n} \frac{\partial \Phi^C_{m,n}}{\partial r} \right] \neq 0 \tag{7.12}$$

which in general is not zero. So, even a single mode contributes to the generation of an average flow. The result including all the modes is

$$\left\langle \tilde{V}_r \tilde{V}_\theta \right\rangle = \frac{1}{2} \sum_{m,n} \frac{m}{r} \left[\Phi^C_{m,n} \frac{\partial \Phi^S_{m,n}}{\partial r} - \Phi^S_{m,n} \frac{\partial \Phi^C_{m,n}}{\partial r} \right] \tag{7.13}$$

so the Reynolds stress is a contribution of all the modes.

The average perpendicular flow $\left\langle \vec{V}_\perp \right\rangle$ can be calculated using Eq. 7.1 and the $(0,0)$ component of the electrostatic potential $\Phi(0,0)$. We use numerical data from a steady state plasma, the same described in Chapter 4 for the magnetic configuration 100_44 in TJ-II. For an arbitrary time, both quantities (velocity and potential) are represented in Fig. 7.3 where the colors show the $\Phi(0,0)$ and arrows show the magnitude and direction of the perpendicular flow generated by this potential. The resultant perpendicular velocity, as we use the $\Phi(0,0)$, has a radial component equal to zero. The poloidal direction of the velocity is given by the gradient of the electrostatic potential so radial shear in the velocity is observed in the figure.

In a similar way, we can obtain the perpendicular velocity from the fluctuating part of the electrostatic potential. Figure 7.4 is showing these results. In the figure there are three radial locations where fluctuations are clearly present around $r/a \approx 0.37$, $r/a \approx 0.50$ and $r/a \approx 0.62$ corresponding to the rational surfaces 25/16, 11/7 and 19/12 respectively (see the rotational transform for the standard magnetic configuration in TJ-II in Fig.4.1). In this case the fluctuations are not as clear as in the analytical example but the perpendicular

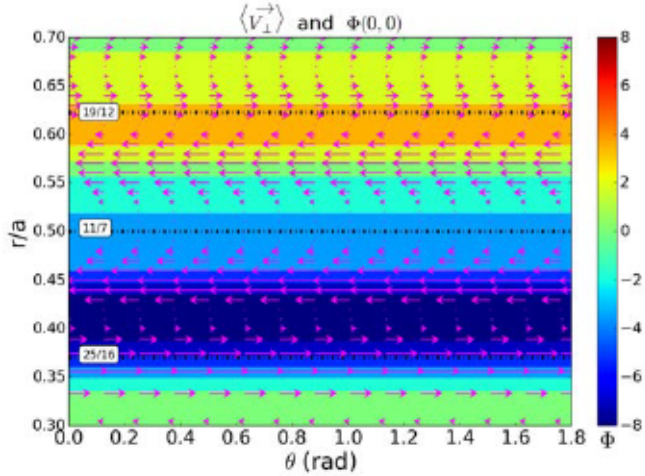

Figure 7.3: Electrostatic potential fluctuation $\Phi(0,0)$. Arrows represent the perpendicular velocity generated by this electrostatic potential. Numbers in white boxes indicate the radial position of the corresponding rational surface.

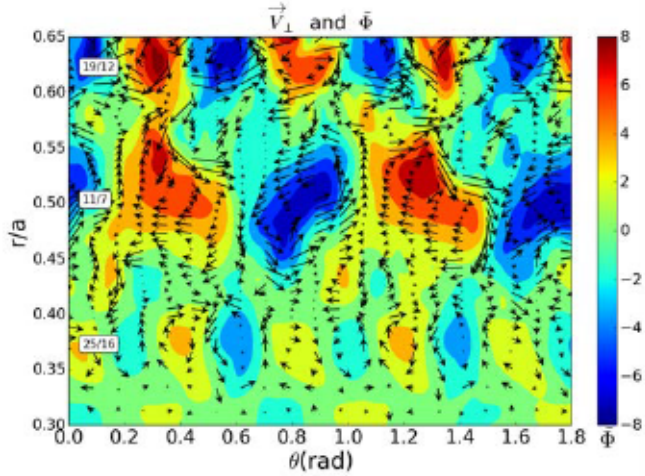

Figure 7.4: Electrostatic potential fluctuation $\tilde{\Phi}$ for a steady state plasma in TJ-II. The arrows represent the perpendicular velocity generated by this electrostatic potential.

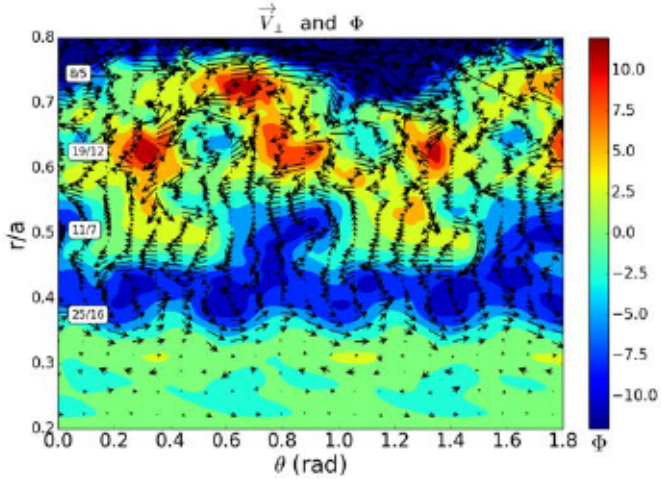

Figure 7.5: Total electrostatic potential Φ for a steady state plasma in TJ-II at a fixed toroidal angle. The arrows represent the perpendicular velocity generated by this electrostatic potential.

velocity is showing undoubtedly turbulent vortices around these fluctuations. These fluctuations (via Reynolds stress) may have a contribution in the average poloidal flow and are partly responsible to the global plasma rotation. Notice that the values in Fig. 7.4 are obtained for a fixed time and toroidal angle. In general these structures are evolving and rotating in the plasma as it will be shown in the next chapters.

There are two contributions to the total perpendicular velocity: one is the average poloidal flow and the other one is the fluctuating part. One may think that the fluctuating component is lower but, in fact, both quantities are comparable (see Φ values in Fig. 7.3 and 7.4). Therefore the total perpendicular velocity should exhibit both contributions, Fig. 7.5 shows the total electrostatic potential and perpendicular velocity for a fixed toroidal angle. This way the total perpendicular velocity shows a similar pattern as the average flow but with some fluctuations caused by the turbulent vortices, for example the region from $r/a = 0.35$ to $r/a = 0.45$, where a strong radial shear is observed. However there are other radial regions where the turbulent vortices seem to dominate as for example $r/a \approx 0.62$.

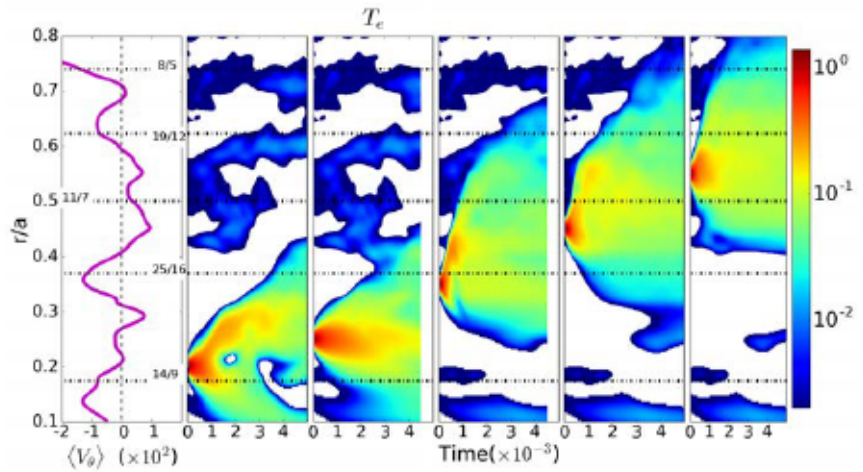

Figure 7.6: Left panel shows the average poloidal velocity before the perturbations. The right five panels display the heat evolution of five perturbations at different radial locations (same figure as Fig. 4.6).

7.3 Transport and poloidal flow

In Chapters 4 and 5 the heat transport was studied using heat perturbations. Heat pulses were set in the plasma and their temporal evolution were analyzed. In order to study heat transport across the plasma, various perturbations were introduced at different radial locations.

Here we focus in the numerical results obtained in Chapter 4. Figure 7.6 is showing (in the five right panels) the temporal evolution of five heat pulses at different radial positions, namely $r/a = 0.20$, $r/a = 0.25$, $r/a = 0.35$, $r/a = 0.45$ $r/a = 0.55$. They show the electron temperature difference from the initial profile (just before the perturbation). The left panel illustrates the average poloidal velocity just before the pulse is introduced. The horizontal dashed lines specify the location of the main low order rational surfaces. In all the cases the perturbations are propagating radially, however at some radial regions they propagate faster or slower. Particularly, we observe "trapping" regions, where the radial propagation is slowed down, around $r/a \approx 0.30$ $r/a \approx 0.4$, $r/a \approx 0.60$ and $r/a \approx 0.70$. In all these regions a strong radial shear in the average poloidal flow $d\langle V_\theta \rangle / dr$ is present (see left panel or Fig. 7.3). The shear in the poloidal flow acts as a transport barrier where the radial heat propagation is reduced, usually

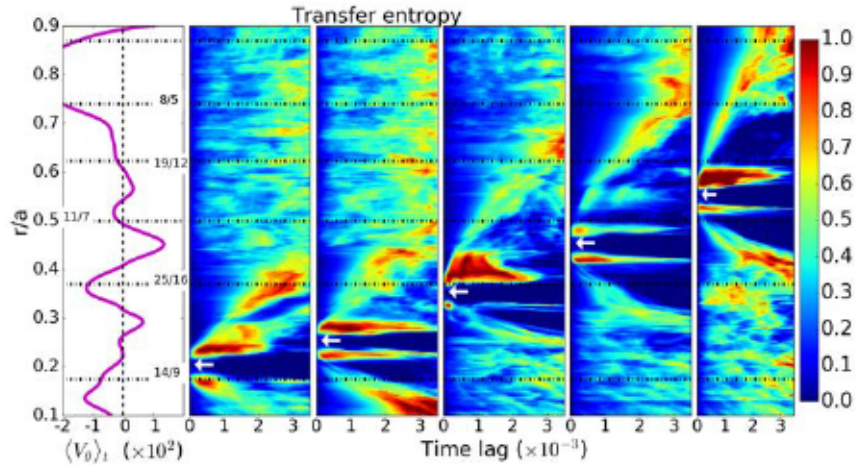

Figure 7.7: Left panel shows the temporal averaged poloidal velocity. The right five panels shows the heat evolution, using the Transfer Entropy, of five perturbations at different radial locations (same figure as Fig. 4.10).

the barriers are created between turbulent vortices.

In Chapter 4 the Transfer Entropy (TE) technique was used to analyze heat transport as well. The technique has become a powerful tool, especially in experimental plasmas, in the study of heat transport [1, 3]. The TE is applied to the heat perturbations in Fig. 7.6 (for more details see Sec. 4.5). The TE results are presented again in Fig. 7.7. The left panel is the poloidal flow averaged over a time ($\approx 0.1\tau_R$) much longer than a typical pulse propagation. The other five panels correspond to the Transfer Entropy result from the five heat perturbations in Fig. 7.6. The white arrows indicate the radial position of the reference signal in the TE calculation.

The TE results show, as well, a radial outward propagation at different rates. Furthermore, at some radial regions we observe high TE values during a long time lag period. Those "trapping" regions reveal the areas where heat perturbations are slowed down. For example, the area around $r/a \approx 0.25$ is observed in the second and third panel. Another trapping region around $r/a \approx 0.38$ is visible in the second, third and fourth panels. In $r/a \approx 0.6$ another transport barrier is seen in the sixth panel. All these trapping areas are located next to (or into) a radial shear region and coincide with the results in Fig. 7.6. Nevertheless the trapping region around $r/a \approx 0.6$ has low radial shear in the

temporal averaged poloidal flow. We suggest that in $r/a = 0.62$ the rational surface 19/12 is generating turbulent vortices in that location (see Fig. 7.5) which can be the reason to find a trapping region.

In conclusion, we introduced electron temperature perturbations to study radial heat transport on low magnetic shear stellarators. Heat transport was found non diffusive and different (mini) transport barriers were identified. These results were confirmed using the Transfer Entropy technique. The radial shear of the average poloidal flow was suggested as the cause of these barriers or trapping regions. During this chapter we went into detail about how the poloidal flow is generated. Our numerical simulations are based in an MHD model where resistive interchange modes are the main instabilities. The fluctuations in this kind of turbulence are causing the generation of turbulent vortices and, at the same time, an average poloidal flow.

Chapter 8

Filamentary structures in TJ-II

In Chapters 4 and 5 the radial heat propagation has been studied using the Transfer Entropy (TE) approach. One of the characteristics we observed is that heat propagation suggests the presence of transport barriers. The heat transport was affected by the radial shear of the poloidal flow. That poloidal flow is generated by the turbulence via the Reynolds stress [62] [99] as we haven pointed out in Chapter 7. In our MHD model (see Chapter 2), turbulence is dominated by pressure driven instabilities, in particular, resistive interchange modes.

The rotational transform represents the magnetic configuration of the fusion device, it is the ratio of poloidal turns by toroidal turns of the magnetic field. There are surfaces where the rotational transform is a rational number and the magnetic field lines are closed so they are known as rational surfaces. Around these surfaces turbulent structures may appear. Due to the nature of interchange modes, these instabilities are extended along the field lines so turbulent structures have the same geometry of the magnetic field lines. Therefore turbulent vortices generated by these instabilities follow a filamentary structure. For more details see Chapter 7.

The magnetic configuration of the TJ-II device exhibits a low magnetic shear. That means that there are few low rational surfaces and more distance among them. Under those circumstances, turbulent vortices located around the rational surfaces may extend in a large radial region with a periodicity determined by q (or in stellarators, the rotational transform $\iota = 1/q$). Since interchange turbulent vortices

must have the same geometry as the magnetic field, they should be present as filamentary structures at the rational surfaces.

Recent experiments (Ref. [5]) in the TJ-II showed filamentary structures using the Transfer Entropy technique. The purpose of this chapter is, using our MHD model, interpret that experimental observations and study the connexion with transport barriers. The goal is to understand the underlying physics of the experiment. Nevertheless the model does not intend to simulate the TJ-II in detail so it is used as a qualitative study. In this chapter, using the TE, some of the main properties of the filaments can be studied.

Most of the work presented here has been published in Ref. [5]: B.Ph. van Milligen, J.H. Nicolau, B. Liu, G. Grenfell, U. Losada, B.A. Carreras, L. García and C. Hidalgo. *"Filaments in the edge confinement region of TJ-II"*. Nucl. Fusion **58**, 026030 (2018).

8.1 Experimental background

Filamentary structures have been observed in the TJ-II device using several methods. First time, filamentary currents were detected using x-ray diagnostics [100]. They have been also observed using fast cameras in the SOL [101] [102]. Then, in Ref. [103] correlation between separated Langmuir probes was studied. Indirectly, using correlation analysis, filamentary structures were found along magnetic field lines of size $40 \sim 50$ meters in the parallel direction and only 7 cm in the perpendicular direction.

Recently, the Transfer Entropy (TE) method was applied to the experimental results obtained from two remote Langmuir probes [5]. A schematic of the experimental set up is shown in Fig. 8.1. The two Langmuir probes ("B" and "D") were located at different poloidal and toroidal angles in the device and were measuring the floating potential V_f at the same radius $r/a \approx 0.85$. Then a biasing probe was included in a different location with the purpose to generate an $E \times B$ flow at the edge of the plasma.

The probes are measuring during the discharges meanwhile the biasing probe is modulating the poloidal flow. The TE is then applied to the signals captured by the probes, from probe $V_f^{1,B}$ to $V_f^{2,D}$ in both directions. The results are shown in Fig. 8.2 where the left panel is showing one Transfer Entropy direction and the right panel is showing

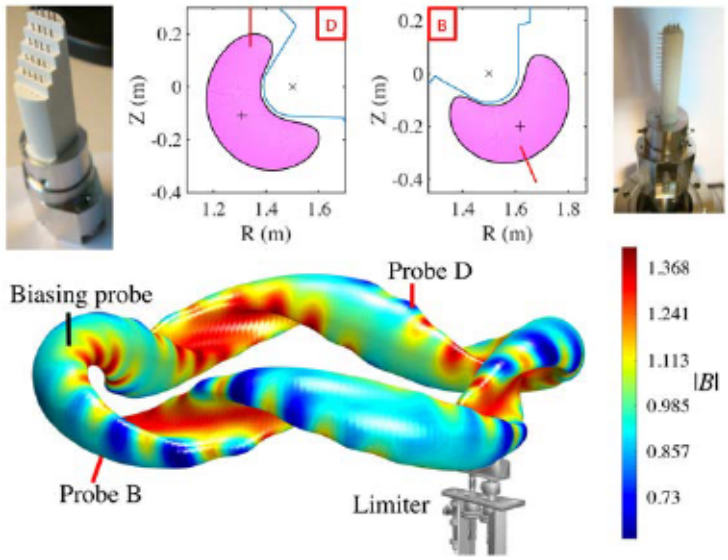

Figure 8.1: Schematic of the experimental set up. The two upper plots show the poloidal location of the two Langmuir probes in a poloidal cross section. The TJ-II diagram at the bottom is illustrating the toroidal position of the two Langmuir probes (B and D) and the biasing probe. The colors represent the magnetic field strength at the last closed flux surface. Picture taken from Ref. [5].

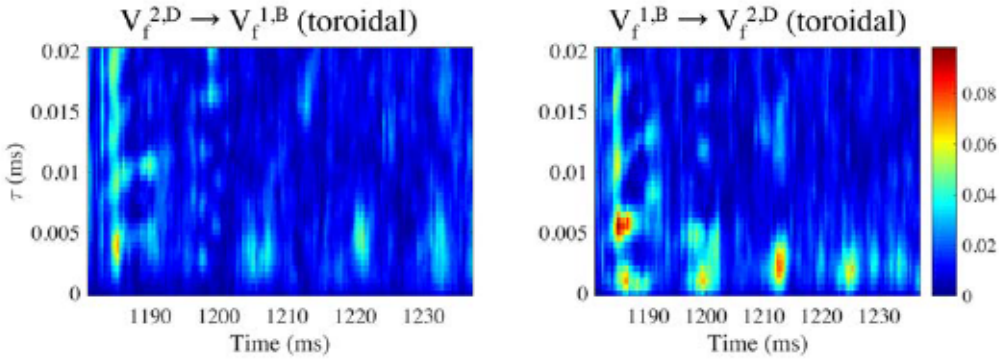

Figure 8.2: Transfer entropy for the floating potential signals of two separated Lagmuir probes $V_f^{1,B}$ and $V_f^{2,D}$. Picture taken from Ref. [5].

the opposite one. Clearly the right one has higher TE values which means that most of the information is flowing $V_f^{1,B} \rightarrow V_f^{2,D}$. Furthermore, one should observe that the high entropy areas in Fig. 8.2 are at times $t \approx 1180$, $t \approx 1200$, $t \approx 1215$ and $t \approx 1225$ms. Those times match exactly with the times where the biasing was set and the plasma was rotating poloidally. Hence, as the transfer entropy is high in only one direction and it coincides when the plasma is rotating we can conclude that the transfer entropy can detect not only when the plasma is rotating but also the rotation direction.

The high entropy areas have a time lag τ around $2 \sim 3$ microseconds. Notice that the probe pins are physically separated a few meters in the toroidal direction. At a first approximation, using the TJ-II parameters, that means the information is flowing at a speed of the order of 10^3 km/s which is not realistic. However, we suggest that there is a filamentary structure in the plasma which rotates poloidally. So the transfer entropy is in fact measuring the time delay of the filament when is crossing first the probe B then the probe D (see upper plots in Fig. 8.1). The Langmuir probes are separated in the poloidal plane only a few centimeters so that means a poloidal velocity around 2 km/s. That result is consistent with the $E \times B$ flow values generated by the biasing probe. In other words, the biasing probe is generating a poloidal flow which makes filaments rotate and those are detected by the Langmuir probes using the Transfer Entropy technique. Furthermore, the unidirectionality of the TE is indicating clearly the rotation direction.

The rotation of the filaments in a poloidal direction was also confirmed using a slightly different method. The Langmuir probes are wide enough to have some pins poloidally distributed but at the same radius. The Transfer entropy was applied to the signals from one single probe but from the pins in the poloidal direction. Similar conclusions were obtained, the TE could detect the rotation of the same piece of filament rotating in the poloidal direction. The TE could capture the time delay (and direction) when one filament crossed one pin and then the other ones.

8.2 Numerical simulations

Trubulent vortices have a filamentary structure and are aligned with magnetic fields lines [2, 104]. Hence, those filaments have the same periodicity as the magnetic field and evolve with the plasma itself. The perpendicular velocity in the plasma is

$$\overrightarrow{V_\perp} = -\nabla\Phi \times \hat{\zeta}. \tag{8.1}$$

In this sense, the poloidal flow is completely determined by the electrostatic potential Φ. Therefore, we study the topology of the Φ which is connected to the turbulent flow.

Using our MHD model, we measure the electrostatic potential at different angular locations. We apply the transfer entropy to these signals in order to study plasma rotation. The transfer entropy can detect whether a perturbation (filament) has crossed our measuring points.

First, we evolve our model equations (see Sec. 2.3.5) until the steady state is reached. In this simulations, we are using the (standard) magnetic configuration 100_44 in TJ-II which is the same as the experiment described in Sec. 8.1. As it was commented before, the low order magnetic rational surfaces generates low m turbulent vortices along the field lines. The low magnetic shear in TJ-II causes a radial extension of the turbulent structures in these surfaces. Under those circumstances, radially wide filamentary structures can be found in the plasma.

We focus on the topology of the fluctuations of the electrostatic potential Φ. For this reason we define the fluctuating electrostatic

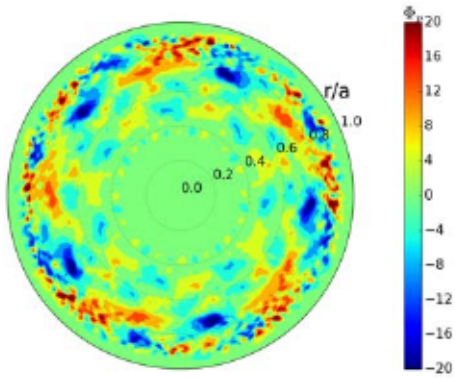

Figure 8.3: Fluctuating electrostatic potential Φ_p in a poloidal cross section in the steady state.

potential as

$$\Phi_p = \Phi - \langle \Phi \rangle$$

where the brackets indicate a poloidal and toroidal angular average. Figure 8.3 is showing the fluctuating electrostatic potential Φ_p in a poloidal cross section at some arbitrary time in the steady state. There are regions, at the same radius, with high or low Φ_p in a periodic way. They may have the periodicity of the rational surface. Some of the low order rational surfaces are easy to identify as the $n = 8/m = 5$ in $r/a \approx 0.75$ because the perturbed potential Φ_p is showing a poloidal periodicity $m = 5$ as expected. Furthermore, the perturbation has a wide radial extension but centered around the rational surface. That perturbation is as well extended along the field lines in the z direction forming a filamentary structure.

Now, we identify the discrete spatial points in our system where the fluctuating electrostatic potential is close to the maximum $\Phi_p > 0.9\Phi_{p\,\mathrm{max}}$ for a fixed time. These points are represented in a TJ-II geometry (for visualization purposes) in Fig. 8.4. Clearly these values are following a filamentary structure. In this case the values correspond to the 8/5 rational surface. For this reason we can state that there are filamentary structures in our numerical results. In this example the filament is complete and closes itself. In this work filaments are complete and not broken. That is not the case in, for example, the Scrape-Off Layer where structures can appear as broken filaments [105]. The fact of having broken filaments is crucial in the Transfer Entropy technique. The TE may not be able to detect filamentary

Figure 8.4: Spatial points in the system where $\Phi_p > 0.9\Phi_{p\,\max}$ represented in a TJ-II geometry.

structures if they are broken in two or more pieces. The reason is that the filament pieces can evolve in a different way and the TE cannot found the connection among them.

In the next section, methods to detect and obtain properties of the filaments will be presented. In the experiments (see Sec. 8.1), electric potential data from the edge is obtained using (two) Langmuir probes, however the extension to a high number of probes is not economically and practically feasible. Furthermore, locations inward (in the core) are not accessible by the experimental probes. On the other hand, numerical simulations allow us to explore the whole plasma at the desired spatial location. In this work, numerical time series are $0.1\tau_R$ long, enough time to more than one full poloidal rotation in many radial surfaces.

8.3 Length, periodicity and poloidal velocity

8.3.1 Filament length

In order to interpret the experiments in TJ-II, we measure the fluctuations of the electrostatic potential Φ_p using "artificial" probes in our numerical results. Numerical simulations allow to analyze all plasma locations as desired. A schematic of the angular location of the arti-

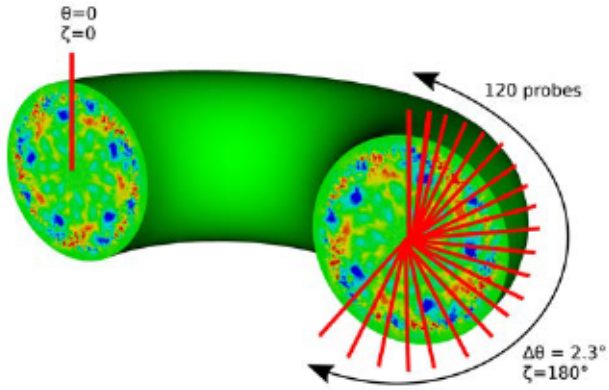

Figure 8.5: Schematic of the "artificial" probe set used in the numerical calculations.

ficial probes we use in the system is shown in Fig. 8.5. There is one reference probe located at $\theta = 0$ and $\zeta = 0$. Then, 120 probes are set at the opposite toroidal angle $\zeta = 180°$. They are separated a poloidal distance $\Delta\theta = 2.3°$, so the set is distributed along a poloidal angle approximately 270°.

$$\text{reference probe} \rightarrow \begin{cases} \theta = 0 \\ \zeta = 0 \end{cases} \qquad 120 \text{ probes} \rightarrow \begin{cases} \Delta\theta = 2.3° \\ \zeta = 180° \end{cases}$$

Notice that, as filaments are structures along field lines, they can be very long. In a poloidal cross section filaments seem to be separated a few centimeters. However, the connexion length between two points along the filament may be several meters long. This idea is illustrated in Figure 8.6. The shaded diagonal areas are the angular locations where the fluctuating potential is positive $\Phi_p > 0.1\Phi_{p\ \max}$ at the radial surface $r/a = 0.75$. The radial location is set on the magnetic rational surface $n = 8/m = 5$ intentionally so Φ_p is showing the expected periodicity in both angles (poloidal $m = 5$ and toroidal $n = 8$). In the same way the white areas are approximately the negative values of the fluctuating electrostatic potential Φ_p. The reference probe is the red square on $\theta = 0$ and $\zeta = 0$, and the other 120 probes are the red squares along $\zeta = 180°$. Then, a dotted diagonal line is indicating the

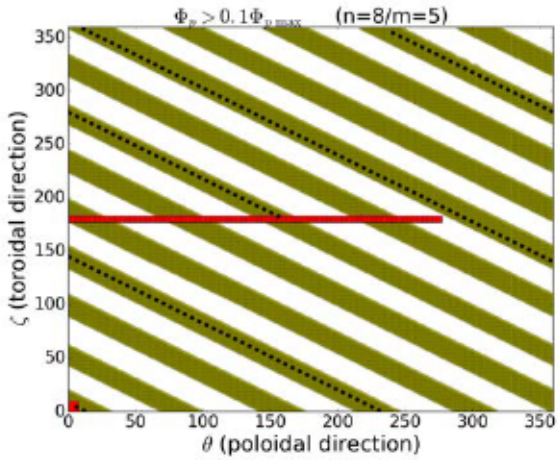

Figure 8.6: The shaded diagonal areas are showing the significantly positive fluctuating electrostatic potential Φ_p at the radial position $r/a = 0.75$, close to the 8/5 rational surface. The red square at (0,0) is the reference probe. The other 120 probes are indicated by the red squares at $\zeta = 180°$. A dotted diagonal black line is following a path between the reference probe an one of the other probes.

path from the reference probe to one of the other probes. As one can see, the path is doing more than two toroidal turns. We can illustrate the real length L of the path using the a and R_0 parameters from TJ-II and

$$L = \sqrt{(\Delta\theta \cdot r)^2 + (\Delta\zeta \cdot R_0)^2} \tag{8.2}$$

where $\Delta\theta$ and $\Delta\zeta$ are the total poloidal and toroidal angles respectively described by the path. The L expression is only valid in a cylindrical geometry. That means that the length path L is approximately 14.8 meters whereas the physical distance between probes (on opposite sides of the device) is just 4.8 meters. The connexion length between the reference probe to the other set varies depending on the probe. The connexion length between probes is not the total length of the filamentary structure which may be much longer. The total length of a filaments is

$$L_{\text{tot}} = 2\pi\sqrt{(nr)^2 + (mR_0)^2} \tag{8.3}$$

which in this case ($n = 8/m = 5$) the total length is approximately $L_{\text{tot}} \approx 48$ m. Notice that this length depends on the periodicity of the

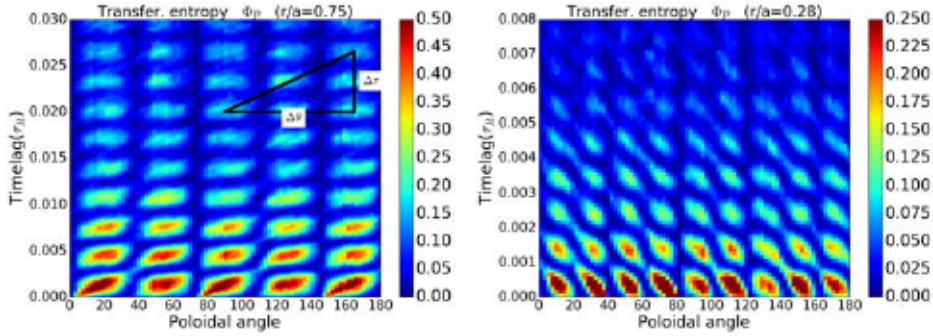

Figure 8.7: Transfer entropy between the reference probe at $\zeta = 0$ and the 120 set probe at $\zeta = 180°$. The left panel is showing the results from the porbes set at $r/a = 0.75$ and the right panel at $r/a = 0.28$. The upper part of the left plot is illustrating the method to calculate the poloidal velocity.

rational surface. Higher order rationals will be associated to longer filamentary structures.

The transfer entropy method can detect the connexion path between two probes only if the filament structure is not broken in more than two pieces. If so, there may not exist a path to connect both probes and the TE would not work. In this work filaments appear not to be broken.

8.3.2 Filament periodicity

As the filaments are rotating they are going to cross first the reference probe and then the other set of probes on the other side of the device (or the opposite depending on the poloidal velocity direction). This effect can be detected using the transfer entropy technique and it is the purpose of the probe set.

We set all the probes described before to a fixed radial position $r/a = 0.75$, which is close to the rational surface $n = 8/m = 5$, and measure the Φ_p. Simulations are run for a long time ($\sim 0.1\tau_R$), then we apply the TE from the reference probe data at $\zeta = 0$ to all the other probes at $\zeta = 180°$. All the results are gathered and plotted in the left panel in Figure 8.7. That is, each *column* at a given poloidal angle is showing the TE from the reference probe to a probe at the given angle. The plot shows, at a certain time lag, high entropy areas

periodically in the poloidal direction. The panel is showing only half of the poloidal angle but for a full poloidal angle there will be 10 high TE areas. Since we are in the the rational surface 8/5, the poloidal periodicity is $m = 5$. The reason why we are seeing a periodicity of 10 is due the fact that the TE is detecting all the filaments with the same periodicity in that surface which includes the positive and negative Φ_p values. That is why we observe twice periodicity in the Transfer entropy.

Notice that, as we pointed out in Sec. 8.3.1, the pieces of filament which are crossing the probes can be separated long distances (tens of meters in TJ-II) in the filament direction. Thus, at short time lags, the Transfer Entropy is detecting different pieces of the filament which may be separated long distances. In spite of that long distance, the TE is exhibiting a high value indicating a connexion.

One should expect that the TE would show high TE areas as the piece of filament which crossed the reference probe is passing through the other set of probes. However, the TE seems to drop as the time lag increases and we are not able to detect that behavior. We suggest that, as the filament is evolving while it rotates after some time the transfer entropy technique cannot identify it.

In the same way, the right plot in Figure 8.7 is showing the results applying the transfer entropy to Φ_p data from the probes set at the fixed radial position $r/a = 0.28$. Again, high TE areas shows a periodicity in the poloidal direction. Using the same arguments as before, we conclude that the transfer entropy is detecting a filamentary structure with a poloidal periodicity $m = 9$. That is consistent with the ι profile since the rational surface $n = 14/m = 9$ is nearby in $r/a = 0.18$.

8.3.3 Poloidal velocity

The plasma is rotating poloidaly in our system so filamentary structures as the Φ_p perturbation should rotate as well. As the filaments are rotating they should cross the probes set since they are distributed along the poloidal angle. This assumption can be observed in the TE results in Figure 8.7. Both panels are showing high TE areas with an elliptical shape and those ellipses are tilted. That tilt is due the fact that filaments are rotating in the poloidal direction as time advances. So as time increases their poloidal positions are changing. However, the tilt is different in the two panels, the left one seems to have a

positive slope and the left one a negative slope. The reason is that the poloidal velocity direction is the opposite in each panel. That slope can be a good estimator of the poloidal velocity.

We use the angle of the tilt to calculate the poloidal velocity of the filamentary structures. The upper right side of the left plot in Figure 8.7 illustrates a schematic of the method. The filament displaces an angle $\Delta\theta$ in a time $\Delta\tau$ so the poloidal velocity is

$$\langle V_\theta \rangle = \omega r = (\Delta\theta/\Delta\tau)\, r. \tag{8.4}$$

That method can be applied not only to the examples in Figure 8.7 but to other different radial locations. Poloidal velocity values with different sign (indicating a poloidal velocity direction) from filaments are obtained using the Transfer Entropy. These values should be compared with the poloidal velocity of the plasma obtained directly from the numerical code. Figure 8.8 is showing in a solid line the temporal average poloidal velocity $\langle V_\theta \rangle$ (average over a time $0.1\tau_R$) calculated from the code. The dashed and dotted lines are representing one standard deviation from the temporal average. That means that poloidal velocity is fluctuating over an average quantity but those changes are not significant. Then, red squares are the poloidal velocity values of the filamentary structures obtained by the Transfer Entropy at different radial locations. The results are consistent with the values from the code. Magnitude of the TE values are similar and, more importantly, the velocity direction matches with the $\langle V_\theta \rangle$ obtained from the code. Furthermore, those results show that the filamentary structures are rotating as the same speed as the plasma.

8.4 Radial width

In the previous section the length, periodicity and poloidal velocity of the filaments were studied using the same set of artificial probes. Here, the radial width of these structures is studied but the probe set should be modified so now it is distributed radially at a fixed angular position. The probes measure the electrostatic potential during the simulations. Then we apply the TE to the data from those simulations. The transfer entropy can detect the connexion between probes so it should be able to capture when (and where) a filament is crossing the reference probes. Therefore, as the probes are distributed radially,

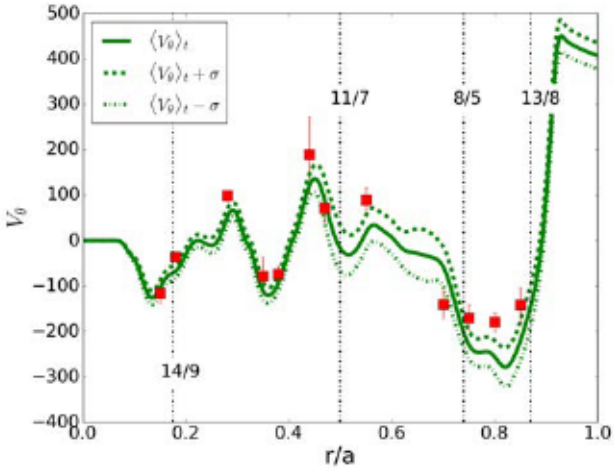

Figure 8.8: Solid line is representing the temporal average of the plasma poloidal velocity. Dashed and dotted lines indicates one standard deviation from the average. Red squares are the poloidal velocity values of the filaments using the TE.

the TE should indicate in what radial locations the filament has been detected.

The reference probe is kept in the same angular location at $\theta = 0$ and $\zeta = 0$. In this example the reference probe is fixed at $r/a = 0.75$ in order to calculate the radial width of the filamentary structure present in that rational surface in particular. The other probes are located at $\theta = 45°$ and $\zeta = 180°$. The set is made of 400 probes distributed radially with a radial spacing $\Delta r = 0.0025a$.

As before, numerical simulations are running in the steady state and the artificial probes are measuring the perturbations of the electrostatic potential Φ_p. Then the Transfer Entropy is applied from the reference probe at a fixed radius to all the other probes along the radial direction. Left panel in Fig. 8.9 is showing these results. So each *column* in the color map is the TE from the reference point to a probe located at that specific radial position. The red vertical dotted line is indicating the position of the reference probe which was set intentionally in the rational 8/5. The other vertical lines are displaying the position of the main rational surfaces. The figure exhibits high TE areas around the reference probe. That means that the TE technique

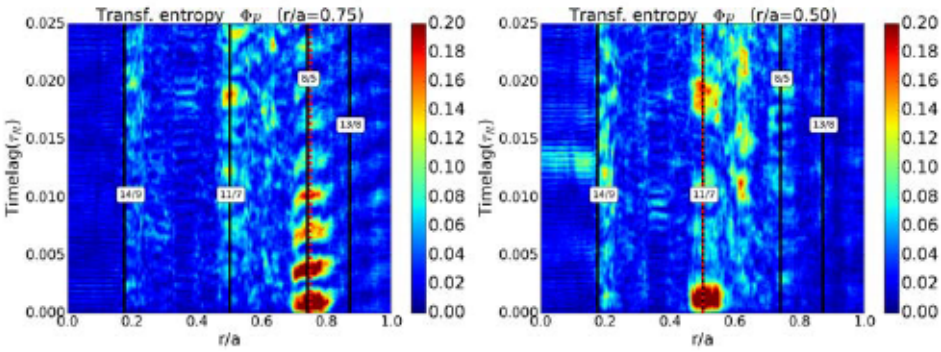

Figure 8.9: Transfer Entropy applied from a reference probe to a set of radially distributed probes. Vertical dotted red line is indicating the radial location of the reference probe (left panel $r/a = 0.75$, right panel $r/a = 0.50$).

has detected where the filament in the reference probe has crossed the probe set. As expected, the filament has been detected in the same radial surface. That is consistent with the idea of filaments being in the same magnetic rational surface. Moreover, the radial width of the high TE region could be a reasonable estimator of the radial width of the filamentary structure. On the other hand, as the time lag increases the high TE area appears repetitively, the reason is that the filament is rotating and is crossing the probes at those times. Furthermore the TE areas are decreasing in time probably because the filament is changing over time and the TE is not capable to detect it after a long time.

The right panel in Fig. 8.9 is showing a similar example. In this case the reference probe is set at the fixed radial point $r/a = 0.50$ which is approximately the location of the rational surface $n = 11/m = 7$. The angular position is fixed. A high TE region around the reference probe is observed as well. Again, that means that the filament is rotating in the same radial surface. The width of that region can be also a good approximation of the radial width of that filament.

To get the values of radial width of that filaments we can do a temporal average of the Transfer entropy for each radial position in Fig. 8.9. Figure 8.10 is showing the temporal average of TE for three cases: filaments 8/5, 11/7 and 14/9. The vertical dashed lines indicate the position of the rational surfaces studied. The three curves show

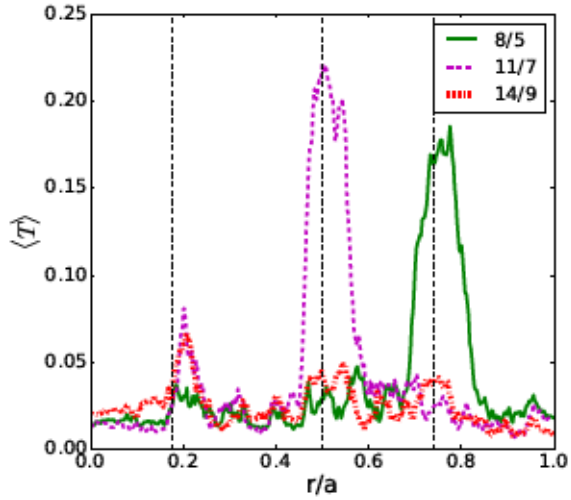

Figure 8.10: Temporal average Transfer entropy between a reference probe and a set of probes distributed radially at a different angular position. The radial position of the references (where the rational surfaces are located) are indicated by vertical dashed lines.

a peak almost centred to the rational surface. The radial width of the filamentary structures can be related to the radial width of these peaks.

This radial method is not only a good method to estimate radial width of filaments but to detect the location of filaments. The TE can identify is there is a connexion between the reference probe and the other radial set of probes.

However this method has a drawback. The TE technique is not able to detect simultaneous events. So, in a hypothetical case where a filament is not rotating (or very slowly) the TE would not detect it because: i) the filament is not moving and it is not crossing the set of probes or ii) the filament is on the probe set but it is not moving so the signals in the reference probe and the set probe are the same, with no time delay, so the TE cannot detect it.

Chapter 9

Filamentary structures in W7-X

In Chapter 8, using the Transfer Entropy (TE) technique, filamentary structures in the TJ-II device were studied. We were able to detect these structures and identify some of their properties. In this chapter we apply the same concepts and methods described in Chapter 8 in order to study filamentary structures in the W7-X stellarator.

First plasma in W7-X was produced in December 2015 and its operation has been improved since then. The first campaigns have been used to test and optimize first plasmas and the different diagnostics. At the moment of writing this thesis, no much work has been done yet in the study of filaments in the W7-X. However, in Ref. [106], using fast cameras it has been possible to observe filamentary structures at the Scrape-Off Layer. This preliminary observations surely will be improved and better diagnostics will be obtained in the future. The first campaigns are still far away to reach the desirable goals but there is a lot of work to be done.

The aim of this chapter is to show some of the properties that future experiments in filaments may exhibit in the W7-X. In this sense, the numerical results shown here may be used as a reference in future works. The TE can be used, as in Ref. [5], to study signals at different locations in the plasma to detect filamentary structures. The technique can capture the connexion among different points in the plasma.

The MHD model we are using for the W7-X has to be seen as a tool to provide some of the basic conditions that can be found in

W7-X plasmas. Under those conditions we study filaments present in the plasma. An MHD model (see Sec. 2.3.5), based on resistive interchanges modes, is used. Based on this kind of instabilities, turbulent structures may appear in the rational surfaces along the magnetic field lines. Therefore, these turbulent structures should exhibit a filamentary geometry. See Chapter 7 for more details.

As the TJ-II, the W7-X has a low magnetic shear. This characteristic allow us to apply the same methods as in Chapter 8 and obtain different results but the same general conclusions. A low magnetic shear implies that the density of low order rational surfaces is small. These surfaces are characterized by the rotational transform $\iota = n/m$ where the n/m illustrates the number of toroidal per poloidal turns of the magnetic field. Furthermore, the turbulent structures generated by the interchange instabilities may extend radially due to the low magnetic shear. The location of these structures in a wide radial region facilitates its detection and study.

9.1 Numerical simulations

As in Chapter 8, we focus on the electrostatic potential. The first reason is because the results presented here can be compared with future experimental observations as the ones in TJ-II [5] where Langmuir probes were used to measure the floating potential at the plasma edge. Second, the electrostatic potential defines the turbulent flow

$$\overrightarrow{V_\perp} = -\nabla\Phi \times \hat{\zeta}. \tag{9.1}$$

which seems to be the cause of transport barriers we have observed in previous chapters.

The MHD model which was first used in Chapter 5 is used now to measure the electrostatic potential at different plasma locations. Using the Transfer Entropy, we can detect the connexion between two separated signals. Therefore, the technique can identify filamentary structures and their rotation.

The different signals are obtained from numerical simulations in a steady state. The steady state is reached after evolving the model equations (see Sec. 2.3.5) using the (standard) magnetic configuration (see Fig. 5.1) in W7-X. As in the TJ-II, the low magnetic shear in that configuration develop a smaller number of low m magnetic flux

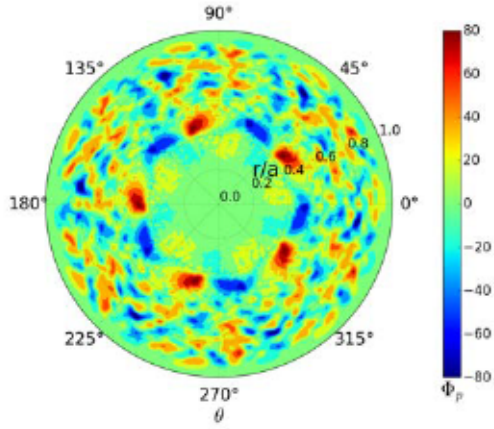

Figure 9.1: Fluctuating electrostatic potential Φ_p in a poloidal cross section in the steady state for the W7-X.

surfaces in the plasma and the turbulent vortices can extend in a wide radial region. Thus, large filamentary structures associated to rational surfaces can be detected easily.

In this chapter, the topology of the fluctuations of the electrostatic potential Φ is studied. Therefore the fluctuating electrostatic potential is defined as

$$\Phi_p = \Phi - \langle \Phi \rangle$$

where the brackets indicate a poloidal and toroidal angular average. Figure 9.1 is showing the Φ_p in a toroidal cross section at the steady state for some arbitrary time. It is clearly visible in $r/a = 0.45$ the effect of the main rational $n = 4/m = 5$ which is the most dominant under this magnetic configuration. At this location the poloidal periodicity of the fluctuation coincides with the $m = 5$. There are five regions where the fluctuations are positive and other five where are negative. In addition, one can observe the wide radial extension of the fluctuations centered in that surface. These fluctuations are extended along the field lines forming filamentary structures due the resistive interchange modes. At other radial locations, even with the presence of higher order rational surfaces, periodicities in the electrostatic perturbation are not as clear. However, other filamentary structures are present.

Figure 9.2 is illustrating (in a W7-X geometry for visualization purposes) the spatial points where the electrostatic potential is close

Figure 9.2: Spatial points in the system where $\Phi_p > 0.9\Phi_{p\,\max}$ represented in a W7-X geometry.

to the maximum $\Phi_p > 0.9\Phi_{p\,\max}$. Using this simply condition a filamentary structure emerges in the system.

This two previous results are showing that the perturbations in the electrostatic potential have a periodicity and then, they can show a filamentary structure.

In the next sections we will propose a method, based on the Transfer Entropy, to detect filamentary structures from different signals. The method can quantify some of the basic properties of the filaments as periodicity, length, poloidal velocity and radial width.

9.2 Filament properties

Usually experiments lack of enough measuring spatial points and the reasons can be economically or, most of the times, practical. For example, experiments in Ref. [5] are using two Langmuir probes to measure floating potential at the edge. Furthermore, probes cannot been introduced in the core because the plasma will be altered and the probes will be damaged.

On the other side, numerical simulations allow to explore the whole system. As an analogy of the experiment, we use a set of *artificial* probes (measuring points) distributed in the plasma. However this artificial probes can measure any radial location. In particular, we use the same set of probes described in Fig. 8.5. There is one probe (we call it *reference probe*) located at $\theta = 0$ and $\zeta = 0$, then at the opposite side of the cylinder $\zeta = 180°$ there is a set of 120 probes distributed along the poloidal direction extending a poloidal angle $\theta = 270°$. So

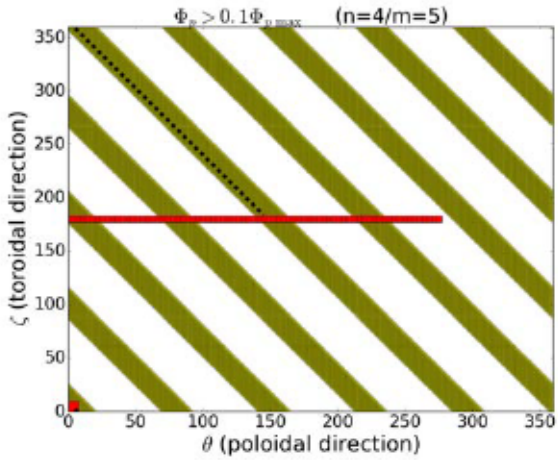

Figure 9.3: The shaded diagonal areas are showing the significantly positive fluctuating electrostatic potential Φ_p at the radial position $r/a = 0.45$, close to the 4/5 rational surface. The red square at (0,0) is the reference probe. The other 120 probes are indicated by the red squares at $\zeta = 180°$. A dotted diagonal black line is following a path between the reference probe and one of the other probes.

$$\text{reference probe} \rightarrow \begin{cases} \theta = 0 \\ \zeta = 0 \end{cases} \qquad 120 \text{ probes} \rightarrow \begin{cases} \Delta\theta = 2.3° \\ \zeta = 180° \end{cases}$$

9.2.1 Filament length

Filaments are usually very long structures which extend along the field lines. The purpose of the probes is to detect those filaments. However as the filaments are 3D structures, even probes located close to each other could detect different pieces of the filament. Figure 9.3 shows this idea. The diagonal shaded areas show the positive Φ_p values at the radial position $r/a = 0.45$, close to the $n = 4/m = 5$ rational surface. As one expects, it shows correctly the rational surface periodicity in this radial position. The reference probe is indicated by a red square at $\theta = 0$ and $\zeta = 0$. Then, at $\zeta = 180°$ the probes set is illustrated by red squares.

The shortest path in Fig. 9.3 between the reference probe and one

of the other probes is shown in a dotted diagonal line. In this case the probes are separated a toroidal angle $\Delta\zeta = 180°$ and poloidal angle $\theta \approx 160°$. The connexion length, and the piece of filament associated to it, can be calculated using

$$L = \sqrt{(\Delta\theta \cdot r)^2 + (\Delta\zeta \cdot R_0)^2} \tag{9.2}$$

so in this example $L \approx 17m$. This value is close to the physical distance (in a toroidal direction) between these probes.

That was the simple case. However, imagine we are interested in the connexion length between the reference probe and a measuring point which is located around $\theta \approx 100°$. In that case the connexion length will be much longer since it needs more than one toroidal turn to connect both probes. In this case the connexion length is $L = 52m$ even if the distance between probes is, as before, approximately 17m.

Therefore probes separated a poloidal angle $\theta = 50°$ (real separation 50 cm) are detecting pieces of filaments with different length. In experiments, where the number of probes is small, that can be relevant and should be taken into account.

9.2.2 Filament periodicity

The artificial probes measure the Φ_p during the steady state. As an example, the electrostatic potential is measured at $r/a = 0.45$ close to the rational surface 4/5. Then the Transfer Entropy is applied from the reference probe ($\zeta = 0$) to all the other probes ($\zeta = 180°$). The results are shown in Fig. 9.4 where each *column* is the TE result of applying the technique from the reference probe to each poloidal angle. As in Chapter 8, high TE areas are found, at the same time lag, to be periodic in the poloidal angle. For a full poloidal angle we found a periodicity equal to ten. That is twice the poloidal periodicity of the rational surface $m = 5$ and the reason is that the TE is detecting filaments with positive and negative values of Φ_p.

A periodicity in the time lag is as well observed because different pieces of the filament are crossing the probe. But after some time lag the TE diminishes probably because the filament is changing. However for long time lags the TE increases again, we suggest that is because the initial piece of filament crosses the probe again after a full poloidal rotation.

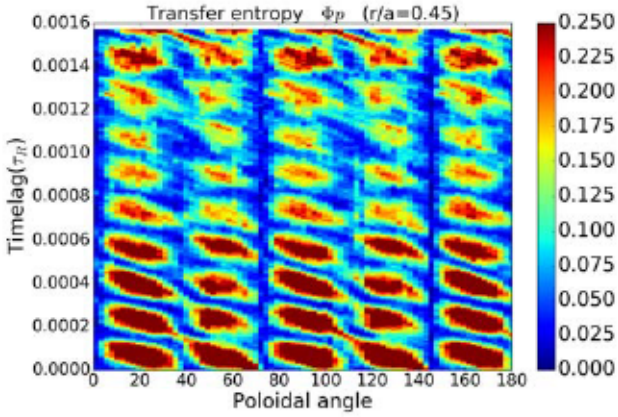

Figure 9.4: Transfer entropy between the reference probe at $\zeta = 0$ and the 120 set probe at $\zeta = 180°$. Electrostatic potential is measured at $r/a = 0.45$.

Similar results are obtained for Φ_p measurements at different radial locations. The TE can capture as well the periodicity of the rational surface where the measurements are taking place.

9.2.3 Poloidal velocity

In Fig. 9.4 the periodicity of the filament is studied. High TE areas indicate the detection of a piece of filament. These areas have a tilted elliptical shape. The tilt is due the fact that the filament is rotating and as the time lag increases the filament is displacing in the poloidal direction.

The tilt can be used as a tool to determine the poloidal velocity of the filament. The velocity can be calculated using (same as Eq. 8.4)

$$\langle V_\theta \rangle = \omega r = (\Delta\theta/\Delta\tau)\, r \tag{9.3}$$

where $\Delta\theta$ is the displaced poloidal angle in a time $\Delta\tau$. These values can be extracted from the figure as shown in the schematic at the upper right on the left panel in Fig. 8.7.

Therefore, by using the Transfer entropy we can calculate the poloidal velocity of filaments at different radial locations. On the other hand, the tilt in the high TE areas seems to have a negative slope as the poloidal angle increases in Fig. 9.4. The sign in the slope

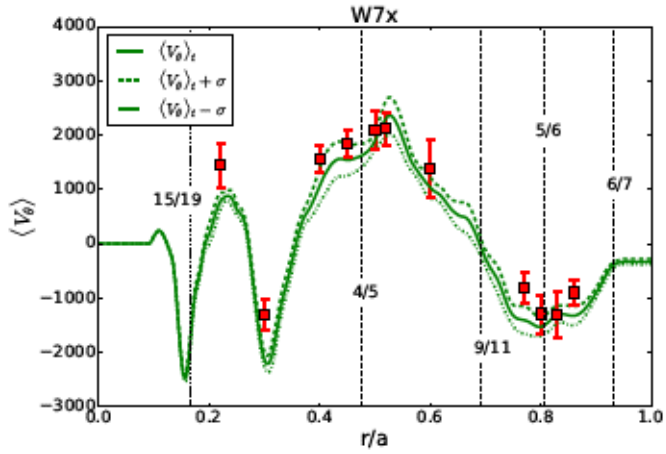

Figure 9.5: Solid line is representing the temporal average of the plasma poloidal velocity. Dashed and dotted lines indicates one standard deviation from the average. Red squares are the poloidal velocity values of the filaments using the TE.

is indicating as well the sign in the poloidal velocity as it was shown in Sec. 8.3.3.

Figure 9.5 shows the result of this method. The red dots indicate the poloidal velocity of the filaments at different radial positions. The solid green line is the average poloidal velocity calculated from the numerical code. The poloidal velocity has been time averaged for a time longer than a full poloidal rotation of many filaments. The dashed and dotted lines are indicating one standard deviation from the average poloidal velocity. The result obtained by the TE agrees with the plasma poloidal rotation obtained by the numerical code. Not only the values are in good agreement but the direction is the correct.

We can conclude that the filaments are rotating with the plasma itself at the same poloidal velocity.

9.3 Radial width

Now we study the radial width of these filamentary structures. As it was mentioned before, the W7-X has a low magnetic shear which allows that turbulent structures, driven by interchange modes, extend into a wide radial extension. Using the Transfer entropy we are able

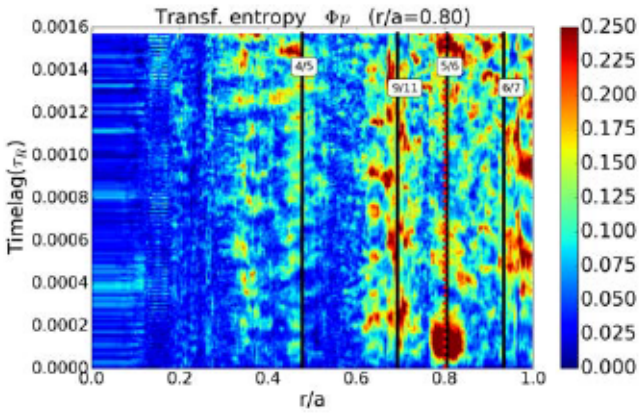

Figure 9.6: Transfer Entropy applied from a reference probe to a set of radially distributed measuring points. Vertical dotted red line is indicating the radial location of the reference probe.

to estimate a radial extension of that turbulent structures.

In the previous section we studied different properties of the filamentary structures as length, periodicity and poloidal velocity. All that properties were studied using the same measuring point configuration. In that section the probes were distributed along the poloidal angle so we were able to detect when a filament cross those measuring points. Here the probe configuration must be modified. The reference probe is kept at the angle $\theta = 0$ and $\zeta = 0$ and, for the next example, $r/a = 0.80$. That radial location is chosen on purpose as it is close to the rational surface $n = 5/m = 6$. The set of measuring points is at $\zeta = 180°$ and $\theta = 45°$ where 400 probes are distributed radially with a radial spacing $\Delta r = 0.0025a$

As before, we measure the fluctuation of the electrostatic potential. Then the Transfer Entropy is applied from the reference point to each of the measuring points distributed radially. Figure 9.6 shows the TE results. The colormap is built in this way: for each radial position the TE is calculated from the reference probe to a measuring point in that particular radial location. A dotted red vertical line indicates the radial position of the reference signal. Other vertical lines show the position of the main rationals. For short time lags a high TE area is observed around the radial location $r/a \approx 0.80$. The radial size of this high TE could be a good estimate of the radial size of the filamentary structure. For longer time lags other high TE areas appear at different

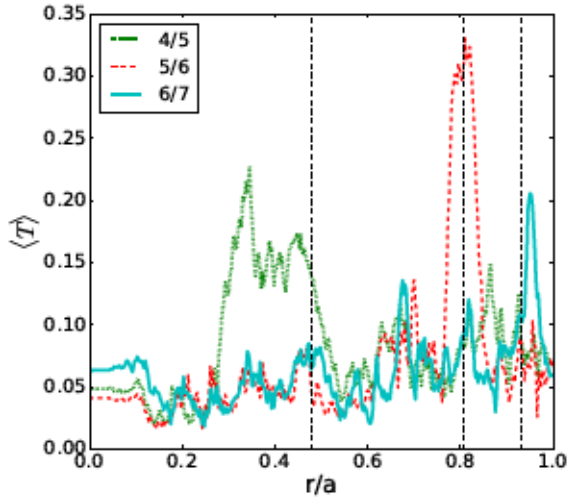

Figure 9.7: Temporal average Transfer entropy between a reference probe and a set of probes distributed radially at a different angular position. The radial position of the references (where the rational surfaces are located) are indicated by vertical dashed lines.

rational surfaces possibly due to a mode coupling. Future work could study these effects.

Using Fig. 9.6 we were able to estimate a radial width of a turbulent structure located around the $n = 5/m = 6$. The same study can be applied to different filamentary structures present in the plasma. Figure 9.7 shows the results of the method for three different cases: a turbulent structure generated at $n = 4/m = 5$ (dotted green line), $n = 5/m = 6$ (dashed red line) and $n = 6/m = 7$ (solid blue line) respectively. The 5/6 curve is the temporal average of the Transfer Entropy (see Fig. 9.6) over a time lag $\Delta\tau = 0.00025\tau_R$. The other two curves are obtained in a similar way but for a TE calculated in the reference probe at the radial location of rational surfaces 4/5 and 6/7 respectively. The three curves exhibit a peak around the radial location of the rational surface (vertical lines). The width of these peaks can be a good estimator of the radial width of the turbulent structures.

Chapter 10

Conclusions

In this thesis we have analyzed heat transport in the stellarators TJ-II and W7-X using an MHD model. To do so we have proposed a new technique called Transfer Entropy (TE). The TE has been presented as a novel technique to analyze time signals from numerical simulations or experiments. It is able to study heat transport and quantify it. Numerical simulations are compared with experimental results showing similar conclusions. Heat transport is being affected by the plasma rotation in the so-called (mini) transport barriers. These barriers are caused by the average flow generated by the instabilities in the plasma. Due the nature of these instabilities (interchange modes), turbulent vortices are present as filamentary structures. We have shown that the Transfer Entropy can detect and analyze these structures. Therefore we have seen how the Transfer Entropy is a powerful technique which can be used in plasma physics in the study of heat transport and filaments in fusion devices.

The Transfer Entropy is applied to TJ-II plasmas simulations in Chapter 4. Using a perturbative method we have shown that the TE can detect how heat perturbations are being transported in the plasma. Heat transport was observed to be not "smooth" so perturbations evolve differently at different radial locations. We observe regions where heat transport is faster and other regions where the perturbations seems to be trapped or slowed down. We call these regions mini transport barriers. The main reason for this distinct transport at different radius is the plasma rotation. The plasma rotates with an average poloidal flow which varies at each radial location. The radial variation (shear) in the poloidal flow seems to be main cause for

the transport barriers. The TE have been compared with the cross-correlation method and the Transfer Entropy exhibits better performance in the study of heat transport. Furthermore, the TE has been applied to numerical simulations of two TJ-II plasmas with different magnetic configuration and analogous conclusions are obtained: TE can analyze heat transport and this transport is being affected by plasma rotation. The numerical results are compared with the experiment showing similar conclusions.

Chapter 5 illustrates the analysis of heat transport in the W7-X stellarator. We have simulated the basic plasma conditions in that device and, using the perturbative method, the TE has been applied in order to examine heat transport. Transport barriers have been observed as well at different radial locations and the plasma rotation appears again to be the main reason of the non-continuous transport. Our numerical simulations have been compared with experimental results of the first campaign in W7-X. The experimental results shows, using the Transfer Entropy, that transport barriers appear in the plasma.

A quantitative approach to study heat transport, based on the Transfer Entropy, has been described in Chapter 6. In this approach we assume that heat transport is in general not diffusive but an effective diffusivity is applicable at small radial intervals. This way, for each radial position a value of diffusivity can be estimated assuming that in that small region diffusivity is constant. The approach has been applied to a simple diffusive model to demonstrate its effectiveness. Then it has been applied to our numerical simulations of TJ-II plasmas with different magnetic configurations. The TE approach results have been compared to diffusive values obtained by local quantities (gradient and flux) and similar values were obtained. Hence we have shown that the Transfer Entropy can be used as well as a tool to estimate and quantify heat transport.

The plasma rotation seems to be the reason to observe a non continuous transport. The interaction of turbulent instabilities produces an average poloidal velocity. In Chapter 7 we have seen how interchange instabilities create turbulent vortices. These vortices are 3D structures which are localized along the field lines at the rational surfaces. Such vortices have a filamentary geometry.

In Chapter 8 filamentary structures in the TJ-II have been analyzed using the Transfer Entropy. The work presented here interprets

and validates the experimental results. In that experiments the presence of filaments in TJ-II was observed using the TE technique. An analogous method is used in our numerical simulations. The TE is applied to the numerical data and different filamentary structures are detected. Furthermore, the TE can determine some of the properties of these structures. As it was expected, we found filaments around the main rational surfaces with a periodicity equal to the periodicity of the surface. The poloidal velocity of the filaments was estimated using the TE and it coincides with the plasma poloidal velocity so filaments are rotating with the plasma itself. The radial width of the structures can be as well determined by the TE. The filamentary structures are located at the rational surfaces but they are extended radially.

Filamentary structures in W7-X plasmas are analyzed as well using the Transfer Entropy in Chapter 9. The technique is applied to the numerical simulations of first plasmas in W7-X. Using the same method as the previous chapter, filaments have been found and certain properties as periodicity, velocity and radial width have been obtained. The numerical results presented here may be a guide to interpret future experiments in filaments in the coming experimental campaigns in W7-X.

Chapter 11

Conclusiones

En esta tesis hemos analizado el transporte de calor en los stellarators TJ-II y W7-X usando un modelo MHD. Para ello hemos propuesto una técnica novedosa llamada Transferencia de Entropía (TE). La TE ha sido presentada como una innovadora técnica para analizar señales temporales obtenidas a partir de simulaciones numéricas o experimentos. La TE es capaz de analizar el transporte de calor y cuantificarlo. Se han comparado simulaciones numéricas con resultados experimentales mostrando conclusiones similares. El transporte de calor se ve afectado por la rotación del plasma en las llamadas (mini) barreras de transporte. Estas barreras están causadas por el flujo promedio generado debido a las inestabilidades en el plasma. Debido a la naturaleza de estas inestabilidades (modos de intercambio), vórtices de turbulencia aparecen en el plasma como estructuras filamentarias. Hemos mostrado como la Transferencia de Entropía puede detectar y analizar esas estructuras. Por lo tanto, hemos mostrado como la Transferencia de Entropía es una poderosa técnica la cual puede ser usada en física de plasmas en el estudio de transporte de calor y filamentos en dispositivos de fusión nuclear.

La Transferencia de Entropía ha sido aplicada a simulaciones de plasmas en el TJ-II en el Capítulo 4. Usando un método perturbativo hemos mostrado que la TE puede detectar cómo perturbaciones de calor se transportan en el plasma. Se ha observado que el transporte de calor no es "suave" pues las perturbaciones evolucionan diferentemente en diferentes posiciones radiales. Observamos regiones donde el transporte de calor es más rápido y otras regiones donde las perturbaciones parecen ser atrapadas o frenadas. Llamamos a esas regiones mini bar-

reras de transporte. La principal razón para este distinto transporte en diferentes radios es la rotación del plasma. El plasma rota con un flujo promedio poloidal el cual varía en cada posición radial. La variación radial (cizalla) en el flujo poloidal parece ser la principal causa de las barreras de transporte. La TE ha sido comparada con el método de correlación cruzada y la Transferencia de Entropía muestra un mejor comportamiento en el estudio del transporte de calor. Además, la TE ha sido aplicada a simulaciones numéricas de dos plasmas en el TJ-II con diferente configuración magnética y se han obtenido conclusiones análogas: la TE puede analizar el transporte de calor y este transporte viene afectado por la rotación del plasma. Los resultados numéricos se han comparado con los experimentos mostrando conclusiones similares.

El Capítulo 5 ilustra el análisis del transporte de calor en el stellarator W7-X. Hemos simulado las condiciones básicas en ese dispositivo y, usando el método perturbativo, la TE se ha aplicado para analizar el transporte de calor. Se han observado también barreras de transporte en diferentes localizaciones radiales y la rotación del plasma parece ser la principal causa para ese transporte no continuo. Nuestras simulaciones numéricas se han comparado con los resultados experimentales de la primera camapaña en el W7-X. Los resultados experimentales muestran, usando la Transferencia de Entropía, que las barreras de transporte aparecen en el plasma.

Un método cuantitativo para estudiar el transporte de calor, basado en la Transferencia de Entropía, se describe en el Capítulo 6. En este método asumimos que el transporte de calor es en general no difusivo pero una difusividad efectiva se puede aplicar en pequeños intervalos radiales. De esta manera, para cada posición radial se puede estimar un valor de difusividad asumiendo que en una pequeña región la difusividad es constante. Este método has sido aplicado a un modelo simple difusivo para demostrar su efectividad. Luego se ha aplicado a nuestras simulaciones numéricas de plasmas en el TJ-II con diferentes configuraciones magnéticas. El método TE ha sido comparado con valores de difusividad obtenidos directamente de magnitudes locales (gradiente y flujo) y se han obtenido valores similares. Por consiguiente hemos mostrado que la Transferencia de Entropía puede usarse también como una herramienta para estimar y cuantificar el transporte de calor.

La rotación del plasma parece ser la razón por la que observamos

un transporte no continuo. La suma e interacción de todas estas inestabilidades produce un velocidad poloidal promedio. En el Capítulo 7 hemos observado cómo las inestabilidades de intercambio generan vórtices de turbulencia. Estos vórtices son estructuras en tres dimensiones que están localizadas a lo largo de las lineas de campo en las superficies racionales. De esta manera los vórtices tiene una geometría filamentaria.

En el Capítulo 8 las estructuras filamentarias en el TJ-II han sido estudiadas usando la Transferencia de Entropía. El trabajo presentado aquí interpreta y validas los resultados experimentales. En esos experimentos se observó la presencia de filamentos en el TJ-II usando la técnica TE. Un método análogo es usado en nuestras simulaciones numéricas. Hemos aplicado la TE a los datos numéricos y diferentes estructuras filamentarias se han observado. Además, la TE puede determinar algunas de las propiedades de estas estructuras. Como se esperaba, encontramos filamentos en las principales superficies racionales con una periodicidad igual a la periodicidad de la superficie. La velocidad poloidal de los filamentos fue estimada usando la TE y coincide con la velocidad poloidal del plasma por lo tanto los filamentos rotan con el propio plasma. El ancho radial de estas estructuras también puede ser determinado por la TE. Las estructuras filamentarias están localizadas en las superficies racionales pero se extiende radialmente.

Las estructuras filamentarias en plasmas del W7-X son también analizadas usando la Transferencia de Entropía en el Capítulo 9. La técnica es aplicada en simulaciones numéricas de los primeros plasmas en W7-X. Usando la misma metodología del anterior capítulo, encontramos filamentos y obtenemos algunas de sus propiedades como periodicidad, velocidad y anchura radial. Los resultados numéricos presentados aquí puede servir de guia para interpretar futuros experimentos en filamentos en las próximas campañas experimentales del W7-X.

Appendices

Appendix A

FAR code

The FAR code was developed at the Oak Ridge National Laboratory in the 1980's as a numerical code to solve fluid equations for toroidally confined fusion plasmas. Previous codes, as KITE, worked in a cylindrical geometry but FAR introduced the option of a toroidal geometry (**F**inite **A**spect **R**atio).

The numerical code uses an implicit method to solve linear fluid equations. The variables are expressed as a Fourier expansion of the form

$$f(r,\theta,\zeta,t) = \sum_{m,n} \left[f^s_{m,n}(r,t) \sin(m\theta + n\zeta) + f^c_{m,n}(r,t) \cos(m\theta + n\zeta) \right]. \tag{A.1}$$

The Fourier Components are discretized using finite differences in time and radial direction.

The equations are solved in the following way. The variables (or fields) can be written as a vector whose components are the modes (or Fourier harmonics) at different grid points at a given time $y^t = xt(l,j)$, where l is the mode index and j the radial point,

$$xt = \begin{pmatrix} xt(1) \\ \vdots \\ xt(j) \\ \vdots \\ xt(mj) \end{pmatrix}, \tag{A.2}$$

where mj is the total radial length and

$$xt\left(j\right)=\begin{pmatrix}\psi\left(j,l1\right)\\ \vdots\\ \psi\left(j,lmax\right)\\ \Phi\left(j,l1\right)\\ \vdots\\ \Phi\left(j,lmax\right)\\ \vdots\end{pmatrix}, \tag{A.3}$$

being ψ and Φ arbitrary fields.

The linear part of the equations can be written as

$$\mathcal{L}\frac{d}{dt}y=\mathcal{R}y \tag{A.4}$$

$$\mathcal{L}\left(\frac{y^{t+\Delta t}-y^{t}}{\Delta t}\right)=\mathcal{R}\left(\frac{y^{t+\Delta t}+y^{t}}{2}\right) \tag{A.5}$$

$$\left(\mathcal{L}-\frac{\Delta t}{2}\mathcal{R}\right)y^{t+\Delta t}=\left(\mathcal{L}+\frac{\Delta t}{2}\mathcal{R}\right)y^{t} \tag{A.6}$$

where y is the array of variables and $\mathcal{L}$ and $\mathcal{R}$ the tridiagonal matrices from the discretization of derivatives

$$\begin{pmatrix}A\left(1\right) & B\left(1\right) & 0 & 0 & \cdots & & & \cdots & 0\\ C\left(2\right) & A\left(2\right) & B\left(2\right) & 0 & \cdots & & & \cdots & 0\\ & \vdots & & \ddots & & & & & \\ 0 & 0 & \cdots & C\left(j\right) & A\left(j\right) & B\left(j\right) & 0 & \cdots & 0\\ & \vdots & & & & & \ddots & & \\ 0 & 0 & \cdots & \cdots & \cdots & 0 & C\left(mj-2\right) & A\left(mj-2\right) & B\left(mj-2\right)\\ 0 & 0 & \cdots & \cdots & \cdots & 0 & 0 & C\left(mj-1\right) & A\left(mj-1\right)\end{pmatrix}. \tag{A.7}$$

Once the matrices are defined, to time advance the equations we add $2\mathcal{L}$ and change the sign from the previous time step, for example $t_1 \rightarrow t_2$,

$$2\mathcal{L}\,y^{t_1}-\left(\mathcal{L}-\frac{\Delta t}{2}\mathcal{R}\right)y^{t_1}=\underbrace{\left(\mathcal{L}+\frac{\Delta t}{2}\mathcal{R}\right)y^{t_1}}_{\left(\mathcal{L}-\frac{\Delta t}{2}\mathcal{R}\right)y^{t_2}}. \tag{A.8}$$

The nonlinear components are explicitly added at each time step using the third order Adams-Moulton algorithm $\left(\sim O\left(\Delta t\right)^{3}\right)$ solved using a predictor-corrector method.

Appendix B

Transfer Entropy computation

Here we qualitatively explain how the Transfer Entropy (TE) is calculated. This appendix provides the main idea of the algorithm.

The Transfer Entropy is applied to two time series $X = (x_1, x_2, \ldots)$ and $Y = (y_1, y_2, \ldots)$. We define the variables

$$x_n^{(j)} = (x_{n-k}, \ldots, x_{n-k\cdot j}) \tag{B.1}$$

$$y_n^{(l)} = (y_{n-k}, \ldots, y_{n-k\cdot l}) \tag{B.2}$$

which are time series of previous states so $k, j, l \in \mathbb{N}$. The general definition of Transfer Entropy is

$$T_{Y\to X} = \sum p\left(x_{n+1}, x_n^{(j)}, y_n^{(l)}\right) \log_2 \frac{p\left(x_{n+1}|x_n^{(j)}, y_n^{(l)}\right)}{p\left(x_{n+1}|x_n^{(j)}\right)} \tag{B.3}$$

but for simplicity [69] we take $j = l = 1$ so the vectors $x_n^{(j)} = x_{n-k}$ and $y_n^{(l)} = y_{n-k}$ only have one value which depends on the "time lag" k. Then the Transfer entropy becomes

$$T_{Y\to X}(k) = \sum p\left(x_{n+1}, x_{n-k}, y_{n-k}\right) \log_2 \frac{p\left(x_{n+1}|x_{n-k}, y_{n-k}\right)}{p\left(x_{n+1}|x_{n-k}\right)}. \tag{B.4}$$

The conditional probabilities can be rewritten knowing that

$$p(x|y) = \frac{p(x,y)}{p(y)}, \tag{B.5}$$

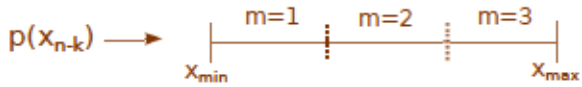

Figure B.1: Schematic of $p\left(x_{n-k}\right)$ construction using m bins.

so the Transfer Entropy is actually calculated using

$$T_{Y\to X}\left(k\right)=\sum p\left(x_{n+1},x_{n-k},y_{n-k}\right)\log_2\frac{p\left(x_{n+1},x_{n-k},y_{n-k}\right)p\left(x_{n-k}\right)}{p\left(x_{n-k},y_{n-k}\right)p\left(x_{n+1},x_{n-k}\right)}. \tag{B.6}$$

Therefore, we need to compute the four probability distribution functions (pdf) to calculate the TE. Each of the pdf is calculated using a discrete number of bins as we will show. The summation in the TE equation correspond to the sum of all these bins. We call m the number of bins in each dimension. For example, in $p\left(x_{n-k}\right)$ the number of bins is just m but for $p\left(x_{n+1},x_{n-k},y_{n-k}\right)$ the number is m^3. The number of bins must be kept small in order to guarantee statistical significance [69], which in the literature is known as *coarse graining*. Due to the amount of data which usually is obtained in plasma physics (specially in numerical simulations) this number should be small. In our simulations the data size is usually lower than 10^3 so $m=3$ is used in our analysis.

Notice that, during the pdf calculations, the time series are reduced as the value k increases. Therefore for high values of k the TE can be altered by the coarse graining. To avoid this problem, in all this work the TE is calculated for values of k up to half of the time series.

The pdfs are calculated in the following way. The easiest function is the $p\left(x_{n-k}\right)$ and it has only three bins. The pdf will be bounded by the minimum $(x_{\min})$ and maximum $(x_{\max})$ values of (x_{n-k}). Figure B.1 shows an schematic of the pdf divided in bins. To construct the pdf, for a fixed k, one goes through all the x_{n-k} values and, for each value of n, add one unit to the corresponding m bin. Then the pdf is normalized.

The $p\left(x_{n-k},y_{n-k}\right)$ is constructed in a similar way but in two dimensions. Figure B.2 illustrates the schematic of bins for this particular pdf. Here we go through all the n values in both signals x_{n-k} and y_{n-k} and we add one unit to the corresponding bin in Fig. B.2. The other two remaining pdfs $(p\left(x_{n+1},x_{n-k},y_{n-k}\right)$ and $p\left(x_{n+1},x_{n-k}\right))$ are obtained using the same method but in their respectively dimensions.

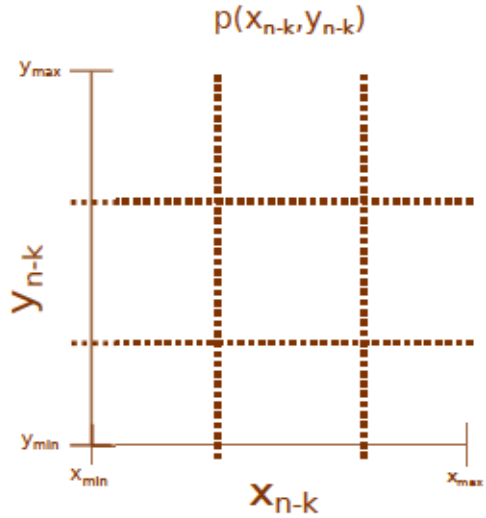

Figure B.2: Schematic of $p\left(x_{n-k}, y_{n-k}\right)$ construction.

In particular the $p\left(x_{n+1}, x_{n-k}, y_{n-k}\right)$ will be three-dimensional.

Once all the pdfs are generated, the next step to get the TE (Eq. B.6) is to sum all the bins. For each term in the summation the correct bin has to be choosen. To do so, imagine we take one bin in $p\left(x_{n+1}, x_{n-k}, y_{n-k}\right)$. That bin shares one or two dimensions with each of the other pdf

$$p\left(x_{n+1}, \underline{x_{n-k}}, \underline{y_{n-k}}\right) \quad \rightarrow \quad p\left(\underline{x_{n-k}}, \underline{y_{n-k}}\right) \tag{B.7}$$

$$p\left(x_{n+1}, \underline{x_{n-k}}, y_{n-k}\right) \quad \rightarrow \quad p\left(\underline{x_{n-k}}\right) \tag{B.8}$$

$$p\left(\underline{x_{n+1}}, \underline{x_{n-k}}, y_{n-k}\right) \quad \rightarrow \quad p\left(\underline{x_{n+1}}, \underline{x_{n-k}}\right), \tag{B.9}$$

notice that they share, by construction, the same boundaries in the same dimension.

As an example we take one bin in $p\left(x_{n+1}, x_{n-k}, y_{n-k}\right)$ which is the third in the x_{n+1} direction, the first in x_{n-k} direction and the second in y_{n-k} direction. To identify this bin we use the notation $p_{x,x,y}\left\{3,1,2\right\}$ where the natural numbers in the brackets indicate the position in each direction and the subindexes represent the dimensions. Therefore, using the same notation, the corresponding bins in the other three

pdfs will be

$$p\left(x_{n-k}, y_{n-k}\right) \rightarrow p_{x,y}\left\{1,2\right\} \tag{B.10}$$

$$p\left(x_{n-k}\right) \rightarrow p_{x}\left\{1\right\} \tag{B.11}$$

$$p\left(x_{n+1}, x_{n-k}\right) \rightarrow p_{x,x}\left\{3,1\right\}. \tag{B.12}$$

So, for this example, the term in the summation in the TE is

$$p_{x,x,y}\left\{3,1,2\right\} \log_2 \frac{p_{x,x,y}\left\{3,1,2\right\} p_{x}\left\{1\right\}}{p_{x,y}\left\{1,2\right\} p_{x,x}\left\{3,1\right\}}. \tag{B.13}$$

All the other terms in the TE are calculated in a similar way, then all the 27 terms are summed. This algorithm is valid for the calculation of the simplified Transfer Entropy (Eq. B.6) where the indexes $j = l = 1$. However for more general versions of the TE, these indexes may be larger than 1 and, as a consequence, the pdfs will be multidimensional.

Bibliography

[1] B.Ph. van Milligen, J.H. Nicolau, L. García, B.A. Carreras, C. Hidalgo, and the TJ-II Team. The impact of rational surfaces on radial heat transport in TJ-II. *Nuclear Fusion*, 57(5):056028, 2017.

[2] B.A. Carreras, I. Llerena Rodríguez, and L. García. Topological structures of the resistive pressure gradient turbulence with averaged poloidal flow. *Nuclear Fusion*, 54(10):103005, 2014.

[3] B.Ph. van Milligen, U. Hoefel, J.H. Nicolau, M. Hirsch, L. García, B.A. Carreras, C. Hidalgo, and the W7-X Team. Study of radial heat transport in W7-X using the transfer entropy. *Nuclear Fusion*, 58(7):076002, 2018.

[4] J. H. Nicolau, L. García, B. A. Carreras, and B. Ph. van Milligen. Applicability of transfer entropy for the calculation of effective diffusivity in heat transport. *Physics of Plasmas*, 25(10):102304, 2018.

[5] B.Ph. van Milligen, J.H. Nicolau, B. Liu, G. Grenfell, U. Losada, B.A. Carreras, L. García, C. Hidalgo, and The TJ-II Team. Filaments in the edge confinement region of TJ-II. *Nuclear Fusion*, 58(2):026030, 2018.

[6] Pedersen T. Sunn, M. Otte, S. Lazerson an P. Helander, S. Bozhenkov, C. Biedermann, T. Klinger, R.C. Wolf, H.S. Bosch, and the W7-X Team. Confirmation of the topology of the Wendelstein 7-X magnetic field to better than 1:100,000. *Nature Communications*, 7:13493, 2016.

[7] Roger Fouquet and Stephen Broadberry. Seven centuries of european economic growth and decline. *Journal of Economic Perspectives*, 29(4):227–44, November 2015.

[8] S. Bilgen. Structure and environmental impact of global energy consumption. *Renewable and Sustainable Energy Reviews*, 38:890 – 902, 2014.

[9] Massimo Livi Bacci. *A concise history of world population*. John Wiley & Sons, 2017.

[10] Peter M. Cox, Richard A. Betts, Chris D. Jones, Steven A. Spall, and Ian J. Totterdell. Acceleration of global warming due to carbon-cycle feedbacks in a coupled climate model. *Nature*, 408(3):184, 2006.

[11] John Cook, Naomi Oreskes, Peter T. Doran, William R. L. Anderegg, Bart Verheggen, Ed W. Maibach, J. Stuart Carlton, Stephan Lewandowsky, Andrew G. Skuce, Sarah A. Green, Dana Nuccitelli, Peter Jacobs, Mark Richardson, Bärbel Winkler, Rob Painting, and Ken Rice. Consensus on consensus: a synthesis of consensus estimates on human-caused global warming. *Environmental Research Letters*, 11(4):048002, 2016.

[12] United Nations (Climate Change). Paris agreement, 2015.

[13] Hualiang Lin, Tao Liu, Jianpeng Xiao, Weilin Zeng, Xing Li, Lingchuan Guo, Yonghui Zhang, Yanjun Xu, Jun Tao, Hong Xian, Kevin M. Syberg, Zhengmin (Min) Qian, and Wenjun Ma. Mortality burden of ambient fine particulate air pollution in six chinese cities: Results from the pearl river delta study. *Environment International*, 96:91 – 97, 2016.

[14] Shuxiao Wang, Jia Xing, Bin Zhao, Carey Jang, and Jiming Hao. Effectiveness of national air pollution control policies on the air quality in metropolitan areas of china. *Journal of Environmental Sciences*, 26(1):13 – 22, 2014.

[15] Wilfred L Kohl. *French nuclear diplomacy*. Princeton University Press, 2015.

[16] Jessica R. Lovering, Arthur Yip, and Ted Nordhaus. Historical construction costs of global nuclear power reactors. *Energy Policy*, 91:371 – 382, 2016.

[17] Georg Steinhauser, Alexander Brandl, and Thomas E. Johnson. Comparison of the chernobyl and fukushima nuclear accidents: A review of the environmental impacts. *Science of The Total Environment*, 470-471:800 – 817, 2014.

[18] Ministerio de Energia, Turismo y Agenda Cultural. *La energia en España 2016*. Gobierno de España, 2016.

[19] Samuel S.M. Wong. *Introductory nuclear physics*. Wiley-VCH, 1999.

[20] Jeffrey P. Freidberg. *Plasma Phyiscs and Fusion Energy*. Cambridge University press, Cambridge University Press, New York, 2007.

[21] Neill P. Taylor, Edward T. Cheng, David A. Petti, and Massimo Zucchetti. Overview of international waste management activities in fusion. *Fusion Technology*, 39(2P2):350–356, 2001.

[22] K. Huang. *Statistical Mechanics (2nd ed.)*. John Wiley and Sons, 1987.

[23] A.E. Costley. On the fusion triple product and fusion power gain of tokamak pilot plants and reactors. *Nuclear Fusion*, 56(6):066003, 2016.

[24] Martin Greenwald. Density limits in toroidal plasmas. *Plasma Physics and Controlled Fusion*, 44(8):R27, 2002.

[25] Francis F. Chen. *Introduction to Plasma Physics and Controlled Fusion*. Springer, 2016.

[26] C. M. Braams and P.E. Stott. *NUCLEAR FUSION. Half a Century of Magnetic Confinement Fusion Research*. Institute of Physics Publishing, 2002.

[27] Jeffrey P. Freidberg. *Ideal MHD*. Cambridge University press, Cambridge University Press, New York, 2014.

[28] J.A. Wesson, R.D. Gill, M. Hugon, F.C. Schüller, J.A. Snipes, D.J. Ward, D.V. Bartlett, D.J. Campbell, P.A. Duperrex, A.W. Edwards, R.S. Granetz, N.A.O. Gottardi, T.C. Hender, E. Lazzaro, P.J. Lomas, N. Lopes Cardozo, K.F. Mast, M.F.F. Nave, N.A. Salmon, P. Smeulders, P.R. Thomas, B.J.D. Tubbing, M.F. Turner, and A. Weller. Disruptions in JET. *Nuclear Fusion*, 29(4):641, 1989.

[29] Jet Design Team. *The JET project. Design Proposal EUR JET R5.* Commission of the European Communities, 1976.

[30] JET Team. Fusion energy production from a deuterium-tritium plasma in the jet tokamak. *Nuclear Fusion*, 32(2):187, 1992.

[31] R Aymar, P Barabaschi, and Y Shimomura. The ITER design. *Plasma Physics and Controlled Fusion*, 44(5):519, 2002.

[32] M. Shimada, D.J. Campbell, V. Mukhovatov, M. Fujiwara, N. Kirneva, K. Lackner, M. Nagami, V.D. Pustovitov, N. Uckan, J. Wesley, N. Asakura, A.E. Costley, A.J.H. Donné, E.J. Doyle, A. Fasoli, C. Gormezano, Y. Gribov, O. Gruber, T.C. Hender, W. Houlberg, S. Ide, Y. Kamada, A. Leonard, B. Lipschultz, A. Loarte, K. Miyamoto, V. Mukhovatov, T.H. Osborne, A. Polevoi, and A.C.C. Sips. Chapter 1: Overview and summary. *Nuclear Fusion*, 47(6):S1, 2007.

[33] Lyman Spitzer. The stellarator concept. *The Physics of Fluids*, 1(4):253–264, 1958.

[34] Carlos Alejaldre, Jose Javier Alonso Gozalo, Jose Botija Perez, Francisco Castejón Magaña, Jose Ramon Cepero Diaz, Jose Guasp Perez, A. Lopez-Fraguas, Luis García, Vladimir I. Krivenski, R. Martín, A. P. Navarro, Angel Perea, Antonio Rodriguez-Yunta, Mario Sorolla Ayza, and Antonio Varias. TJ-II project: A flexible heliac stellarator. *Fusion Technology*, 17(1):131–139, 1990.

[35] M. Bornatici, R. Cano, O. De Barbieri, and F. Engelmann. Electron cyclotron emission and absorption in fusion plasmas. *Nuclear Fusion*, 23(9):1153, 1983.

[36] E. de la Luna, J. Sánchez, V. Tribaldos, and T. Estrada. Multichannel electron cyclotron emission radiometry in TJ-II stellarator. *Review of Scientific Instruments*, 72(1):379–382, 2001.

[37] M. A. Pedrosa, A. López-Sánchez, C. Hidalgo, A. Montoro, A. Gabriel, J. Encabo, J. de la Gama, L. M. Martínez, E. Sénchez, R. Pérez, and C. Sierra. Fast movable remotely controlled Langmuir probe system. *Review of Scientific Instruments*, 70(1):415–418, 1999.

[38] M Wanner, J.-H Feist, H Renner, J Sapper, F Schauer, H Schneider, V Erckmann, and H Niedermeyer. Design and construction of WENDELSTEIN 7-X. *Fusion Engineering and Design*, 56-57:155 – 162, 2001.

[39] R.C. Wolf, A. Ali, A. Alonso, J. Baldzuhn, C. Beidler, M. Beurskens, C. Biedermann, H.-S. Bosch, S. Bozhenkov, R. Brakel, A. Dinklage, Y. Feng, G. Fuchert, J. Geiger, O. Grulke, P. Helander, M. Hirsch, U. Höfel, M. Jakubowski, J. Knauer, G. Kocsis, R. König, P. Kornejew, A. Krämer-Flecken, M. Krychowiak, M. Landreman, A. Langenberg, H.P. Laqua, S. Lazerson, H. Maaßberg, S. Marsen, M. Marushchenko, D. Moseev, H. Niemann, N. Pablant, E. Pasch, K. Rahbarnia, G. Schlisio, T. Stange, T. Sunn Pedersen, J. Svensson, T. Szepesi, H. Trimino Mora, Y. Turkin, T. Wauters, G. Weir, U. Wenzel, T. Windisch, G. Wurden, D. Zhang, and W7-X Team. Major results from the first plasma campaign of the Wendelstein 7-X stellarator. *Nuclear Fusion*, 57(10):102020, 2017.

[40] B. A. Carreras. Progress in anomalous transport research in toroidal magnetic confinement devices. *IEEE Transactions on Plasma Science*, 25(6):1281–1321, Dec 1997.

[41] B. A. Carreras, B. van Milligen, M. A. Pedrosa, R. Balbín, C. Hidalgo, D. E. Newman, E. Sánchez, M. Frances, I. García-Cortés, J. Bleuel, M. Endler, S. Davies, and G. F. Matthews. Long-range time correlations in plasma edge turbulence. *Phys. Rev. Lett.*, 80:4438–4441, May 1998.

[42] Per Bak, Chao Tang, and Kurt Wiesenfeld. Self-organized criticality: An explanation of the 1/f noise. *Phys. Rev. Lett.*, 59:381–384, Jul 1987.

[43] D. E. Newman, B. A. Carreras, P. H. Diamond, and T. S. Hahm. The dynamics of marginality and selforganized criticality as a paradigm for turbulent transport. *Physics of Plasmas*, 3(5):1858–1866, 1996.

[44] R Sanchez and D E Newman. Self-organized criticality and the dynamics of near-marginal turbulent transport in magnetically confined fusion plasmas. *Plasma Physics and Controlled Fusion*, 57(12):123002, 2015.

[45] E.J. Doyle, W.A. Houlberg, Y. Kamada, V. Mukhovatov, T.H. Osborne, A. Polevoi, G. Bateman, J.W. Connor, J.G. Cordey, T. Fujita, X. Garbet, T.S. Hahm, L.D. Horton, A.E. Hubbard, F. Imbeaux, F. Jenko, J.E. Kinsey, Y. Kishimoto, J. Li, T.C. Luce, Y. Martin, M. Ossipenko, V. Parail, A. Peeters, T.L. Rhodes, J.E. Rice, C.M. Roach, V. Rozhansky, F. Ryter, G. Saibene, R. Sartori, A.C.C. Sips, J.A. Snipes, M. Sugihara, E.J. Synakowski, H. Takenaga, T. Takizuka, K. Thomsen, M.R. Wade, H.R. Wilson, ITPA Transport Physics Topical Group, ITPA Confinement Database, Modelling Topical Group, ITPA Pedestal, and Edge Topical Group. Chapter 2: Plasma confinement and transport. *Nuclear Fusion*, 47(6):S18, 2007.

[46] F. Wagner, G. Becker, K. Behringer, D. Campbell, A. Eberhagen, W. Engelhardt, G. Fussmann, O. Gehre, J. Gernhardt, G. v. Gierke, G. Haas, M. Huang, F. Karger, M. Keilhacker, O. Klüber, M. Kornherr, K. Lackner, G. Lisitano, G. G. Lister, H. M. Mayer, D. Meisel, E. R. Müller, H. Murmann, H. Niedermeyer, W. Poschenrieder, H. Rapp, H. Röhr, F. Schneider, G. Siller, E. Speth, A. Stäbler, K. H. Steuer, G. Venus, O. Vollmer, and Z. Yü. Regime of improved confinement and high beta in neutral-beam-heated divertor discharges of the ASDEX Tokamak. *Phys. Rev. Lett.*, 49:1408–1412, Nov 1982.

[47] H. Biglari, P. H. Diamond, and P. W. Terry. Influence of sheared poloidal rotation on edge turbulence. *Physics of Fluids B: Plasma Physics*, 2(1):1–4, 1990.

[48] P. W. Terry. Suppression of turbulence and transport by sheared flow. *Rev. Mod. Phys.*, 72:109–165, Jan 2000.

[49] H Zohm. Edge localized modes (ELMs). *Plasma Physics and Controlled Fusion*, 38(2):105, 1996.

[50] X.L. Zou, G. Giruzzi, J.F. Artaud, F. Bouquey, A. Clémençon, C. Darbos, R.J. Dumont, C. Guivarch, M. Lennholm, R. Magne, and J.L. Ségui. Electron heat transport and ECRH modulation experiments in Tore Supra tokamak. *Nuclear Fusion*, 43(11):1411, 2003.

[51] K. W. Gentle, M. E. Austin, J. C. DeBoo, T. C. Luce, and C. C. Petty. Electron energy transport inferences from modulated electron cyclotron heating in DIII-D. *Physics of Plasmas*, 13(1):012311, 2006.

[52] F Imbeaux, F Ryter, and X Garbet. Modelling of ECH modulation experiments in ASDEX Upgrade with an empirical critical temperature gradient length transport model. *Plasma Physics and Controlled Fusion*, 43(11):1503, 2001.

[53] F. Ryter, C. Angioni, C. Giroud, A.G. Peeters, T. Biewer, R. Bilato, E. Joffrin, T. Johnson, H. Leggate, E. Lerche, G. Madison, P. Mantica, D. Van Eester, I. Voitsekhovitch, and JET Contributors. Simultaneous analysis of ion and electron heat transport by power modulation in JET. *Nuclear Fusion*, 51(11):113016, 2011.

[54] U. Gasparino, V. Erckmann, H.J. Hartfuß, H. Maaßberg, and M. Romé. Transport analysis through heat waves driven at different radial positions. *Plasma Physics and Controlled Fusion*, 40(2):233, 1998.

[55] M. Soler and J.D. Callen. On measuring the electron heat diffusion coefficient in a Tokamak from sawtooth oscillation observations. *Nuclear Fusion*, 19(6):703, 1979.

[56] N. J. Lopes Cardozo. Perturbative transport studies in fusion plasmas. *Plasma Physics and Controlled Fusion*, 37(8):799, 1995.

[57] P. Mantica and F. Ryter. Perturbative studies of turbulent transport in fusion plasmas. *Comptes Rendus Physique*, 7(6):634 – 649, 2006.

[58] Masaaki Yamada, Russell Kulsrud, and Hantao Ji. Magnetic reconnection. *Rev. Mod. Phys.*, 82:603–664, Mar 2010.

[59] John M. Greene and John L. Johnson. Determination of hydromagnetic equilibria. *The Physics of Fluids*, 4(7):875–890, 1961.

[60] M Wakatani. *Stellarator and Heliotron Devices*. Oxford University Press, 1998.

[61] B. A. Carreras, L. García, and P. H. Diamond. Theory of resistive pressure-gradient-driven turbulence. *The Physics of Fluids*, 30(5):1388–1400, 1987.

[62] B. A. Carreras, V. E. Lynch, and L. García. Electron diamagnetic effects on the resistive pressure-gradient-driven turbulence and poloidal flow generation. *Physics of Fluids B: Plasma Physics*, 3(6):1438–1444, 1991.

[63] L. García, B. A. Carreras, V. E. Lynch, M. A. Pedrosa, and C. Hidalgo. Sheared flow amplification by vacuum magnetic islands in stellarator plasmas. *Physics of Plasmas*, 8(9):4111–4119, 2001.

[64] R.D. Hazeltine and J.D. Meiss. *Plasma confinement*. Dover Publications, 2003.

[65] J. F. Drake and Thomas M. Antonsen. Nonlinear reduced fluid equations for toroidal plasmas. *The Physics of Fluids*, 27(4):898–908, 1984.

[66] L.A Charlton, J.A Holmes, H.R Hicks, V.E Lynch, and B.A Carreras. Numerical calculations using the full MHD equations in toroidal geometry. *Journal of Computational Physics*, 63(1):107 – 129, 1986.

[67] L. Garcia, H.R. Hicks, B.A. Carreras, L.A. Charlton, and J.A. Holmes. 3D nonlinear MHD calculations using implicit and explicit time integration schemes. *Journal of Computational Physics*, 65(2):253 – 272, 1986.

[68] I Teliban, D Block, A Piel, and F Greiner. Improved conditional averaging technique for plasma fluctuation diagnostics. *Plasma Physics and Controlled Fusion*, 49(4):485, 2007.

[69] Thomas Schreiber. Measuring information transfer. *Phys. Rev. Lett.*, 85:461–464, Jul 2000.

[70] C.W.J. Granger. Testing for causality: A personal viewpoint. *Journal of Economic Dynamics and Control*, 2:329 – 352, 1980.

[71] N. Wiener. *The theory of prediction. Modern Mathematics for the Engineer.* McGraw-Hill, New York, 1956.

[72] Raul Vicente, Michael Wibral, Michael Lindner, and Gordon Pipa. Transfer entropy—a model-free measure of effective connectivity for the neurosciences. *Journal of Computational Neuroscience*, 30(1):45–67, Feb 2011.

[73] Sosuke Ito and Takahiro Sagawa. Maxwells demon in biochemical signal transduction with feedback loop. *Nature Communications*, 6(7498), 2015.

[74] M. Bauer, J. W. Cox, M. H. Caveness, J. J. Downs, and N. F. Thornhill. Finding the direction of disturbance propagation in a chemical process using transfer entropy. *IEEE Transactions on Control Systems Technology*, 15(1):12–21, Jan 2007.

[75] T. Dimpfl and F. Peter. Using transfer entropy to measure information flows between financial markets. *Studies in Nonlinear Dynamics and Econometrics*, 17(1):85–102, 2013.

[76] B.Ph. van Milligen, G. Birkenmeier, M. Ramisch, T. Estrada, C. Hidalgo, and A. Alonso. Causality detection and turbulence in fusion plasmas. *Nuclear Fusion*, 54(2):023011, 2014.

[77] B. Ph. van Milligen, B. A. Carreras, L. García, A. Martín de Aguilera, C. Hidalgo, and J. H. Nicolau. The causal relation between turbulent particle flux and density gradient. *Physics of Plasmas*, 23(7):072307, 2016.

[78] A. Murari, E. Peluso, M. Gelfusa, L. Garzotti, D. Frigione, M. Lungaroni, F. Pisano, P. Gaudio, and JET Contributors. Application of transfer entropy to causality detection and synchronization experiments in tokamaks. *Nuclear Fusion*, 56(2):026006, 2016.

[79] C. E. Shannon. A mathematical theory of communication. *The Bell System Tehcnical Journal*, 27:623–656, 1948.

[80] C. E. Shannon. A mathematical theory of communication. *SIGMOBILE Mob. Comput. Commun. Rev.*, 5(1):3–55, January 2001.

[81] Terry Bossomaier, Michael Harré, Lionel Barnett, and Joseph T. Lizier. *An introduction to Transfer Entropy (Information flow in Complex Systems).* Springer, 2016.

[82] Stefan M. Moser and Po-Ning Chen. *A student's guide to coding and informationi theory.* Cambridge University Press, 2012.

[83] M. Tribus. *An engineer looks at Bayes. Seventh Annual Workshop: Maximum Entropy and Bayesian Methods.* Springer, 1987.

[84] Henry D. I. Abarbanel, Reggie Brown, John J. Sidorowich, and Lev Sh. Tsimring. The analysis of observed chaotic data in physical systems. *Rev. Mod. Phys.*, 65:1331–1392, Oct 1993.

[85] Alfred J. Lotka. Contribution to the theory of periodic reactions. *The Journal of Physical Chemistry*, 14(3):271–274, 1909.

[86] Vito Volterra. Variations and fluctuations of the number of individuals in animal species living together. *ICES Journal of Marine Science*, 3(1):3–51, 1928.

[87] S. Eguilior, F. Castejón, E. de la Luna, A. Cappa, K-Likin, A-Fernández, and TJ-II Team. Heat wave experiments on TJ-II flexible heliac. *Plasma Physics and Controlled Fusion*, 45(2):105, 2003.

[88] T. Happel, A. Bañón Navarro, G. D. Conway, C. Angioni, M. Bernert, M. Dunne, E. Fable, B. Geiger, T. Görler, F. Jenko, R. M. McDermott, F. Ryter, and U. Stroth. Core turbulence

behavior moving from ion-temperature-gradient regime towards trapped-electron-mode regime in the ASDEX Upgrade tokamak and comparison with gyrokinetic simulation. *Physics of Plasmas*, 22(3):032503, 2015.

[89] S. Sattler and H. J. Hartfuss. Experimental evidence for electron temperature fluctuations in the core plasma of the W7-AS stellarator. *Phys. Rev. Lett.*, 72:653–656, Jan 1994.

[90] P. A. Politzer. Observation of avalanchelike phenomena in a magnetically confined plasma. *Phys. Rev. Lett.*, 84:1192–1195, Feb 2000.

[91] N. B. Marushchenko, A. Dinklage, H. J. Hartfuss, M. Hirsch, H. Maassberg, and Yu. Turkin. Optimization of ECE diagnostics for the W7-X stellarator. *Fusion Science and Technology*, 50(3):395–402, 2006.

[92] Ralf König and W7-X Team. The set of diagnostics for the first operation campaign of the Wendelstein 7-X stellarator. *Journal of Instrumentation*, 10(10):P10002, 2015.

[93] Radu Balescu. *Aspects of anomalous transport in plasmas*. Institute of Physics Publishing (GB), 2005.

[94] G.M.D. Hogeweij, N.J. Lopes Cardozo, M.R. De Baar, and A.M.R. Schilham. A model for electron transport barriers in tokamaks, tested against experimental data from rtp. *Nuclear Fusion*, 38(12):1881, 1998.

[95] A M R Schilham, G M D Hogeweij, and N J Lopes Cardozo. Electron thermal transport barriers in RTP: experiment and modelling. *Plasma Physics and Controlled Fusion*, 43(12):1699, 2001.

[96] C. Caso, G. Conforto, A. Gurtu, M. Aguilar-Benitez, C. Amsler, R.M. Barnett, P.R. Burchat, C.D. Carone, O. Dahl, M. Doser, S. Eidelman, J.L. Feng, M. Goodman, C. Grab, D.E. Groom, K. Hagiwara, K.G. Hayes, J.J. Hernández, K. Hikasa, K. Honscheid, F. James, M.L. Mangano, A.V. Manohar, K. Mönig, H. Murayama, K. Nakamura, K.A. Olive, A. Piepke, M. Roos, R.H. Schindler, R.E. Shrock, M. Tanabashi, N.A. Törnqvist,

T.G. Trippe, P. Vogel, C.G. Wohl, R.L. Workman, and W.-M. Yao. Particle Data Group. Review of particle physics. *The European Physical Journal C*, 3:1–794, 1998.

[97] B. A. Carreras, V. E. Lynch, L. García, and P. H. Diamond. Resistive pressure-gradient-driven turbulence with self-consistent flow profile evolution. *Physics of Fluids B: Plasma Physics*, 5(5):1491–1505, 1993.

[98] K. C. Shaing and E. C. Crume. Bifurcation theory of poloidal rotation in tokamaks: A model for L-H transition. *Phys. Rev. Lett.*, 63:2369–2372, Nov 1989.

[99] P. H. Diamond, Y.-M. Liang, B. A. Carreras, and P. W. Terry. Self-regulating shear flow turbulence: A paradigm for the L to H transition. *Phys. Rev. Lett.*, 72:2565–2568, Apr 1994.

[100] F. Medina, M. A. Pedrosa, M. A. Ochando, L. Rodríguez, C. Hidalgo, A. L. Fraguas, B. A. Carreras, and the TJ-II Team. Filamentary current detection in stellarator plasmas. *Review of Scientific Instruments*, 72(1):471–474, 2001.

[101] D. Carralero, E. de la Cal, J.L. de Pablos, A. de Coninck, J.A. Alonso, C. Hidalgo, B.Ph. van Milligen, and M.A. Pedrosa. Turbulence studies by fast camera imaging experiments in the TJ-II stellarator. *Journal of Nuclear Materials*, 390-391:457 – 460, 2009. Proceedings of the 18th International Conference on Plasma-Surface Interactions in Controlled Fusion Device.

[102] E de la Cal, P Semwal, A Martín Aguilera, B van Milligen, J L de Pablos, Z Khan, and C Hidalgo. Double imaging with an intensified visible fast camera to visualize the fine structure of turbulent coherent plasma structures (blobs) in TJ-II. *Plasma Physics and Controlled Fusion*, 56(10):105003, 2014.

[103] B.Ph. van Milligen, A. Lopez Fraguas, M.A. Pedrosa, C. Hidalgo, A. Martín de Aguilera, and E. Ascasíbar. Parallel and perpendicular turbulence correlation length in the TJ-II stellarator. *Nuclear Fusion*, 53(9):093025, 2013.

[104] Benjamín A Carreras, Irene Llerena Rodríguez, and Luis García. A topological analysis of plasma flow structures. *Journal of Physics A: Mathematical and Theoretical*, 46(37):375501, 2013.

[105] D. A. D'Ippolito, J. R. Myra, and S. J. Zweben. Convective transport by intermittent blob-filaments: Comparison of theory and experiment. *Physics of Plasmas*, 18(6):060501, 2011.

[106] G. Kocsis, A. Alonso, C. Biedermann, G. Cseh, A. Dinklage, M. Jakubowski, R. König, M. Krychowiak, M. Otte, T. Sunn Pedersen, T. Szepesi, and S. Zoletnik. Investigation of edge filament dynamics in W7-X limiter plasmas. In *43rd EPS Conference on Plasma Physics*, page P4.003, Leuven, Belgium, 2017. European Physical Society.